PRODUCTION OF POSITRONS WITH LOW TRANSVERSE MOMENTUM AND LOW-MASS ELECTRON-POSITRON PAIRS IN PROTON-PROTON COLLISIONS AT A CENTER-OF-MASS ENERGY OF 63 GEV.

VINCENT HEDBERG

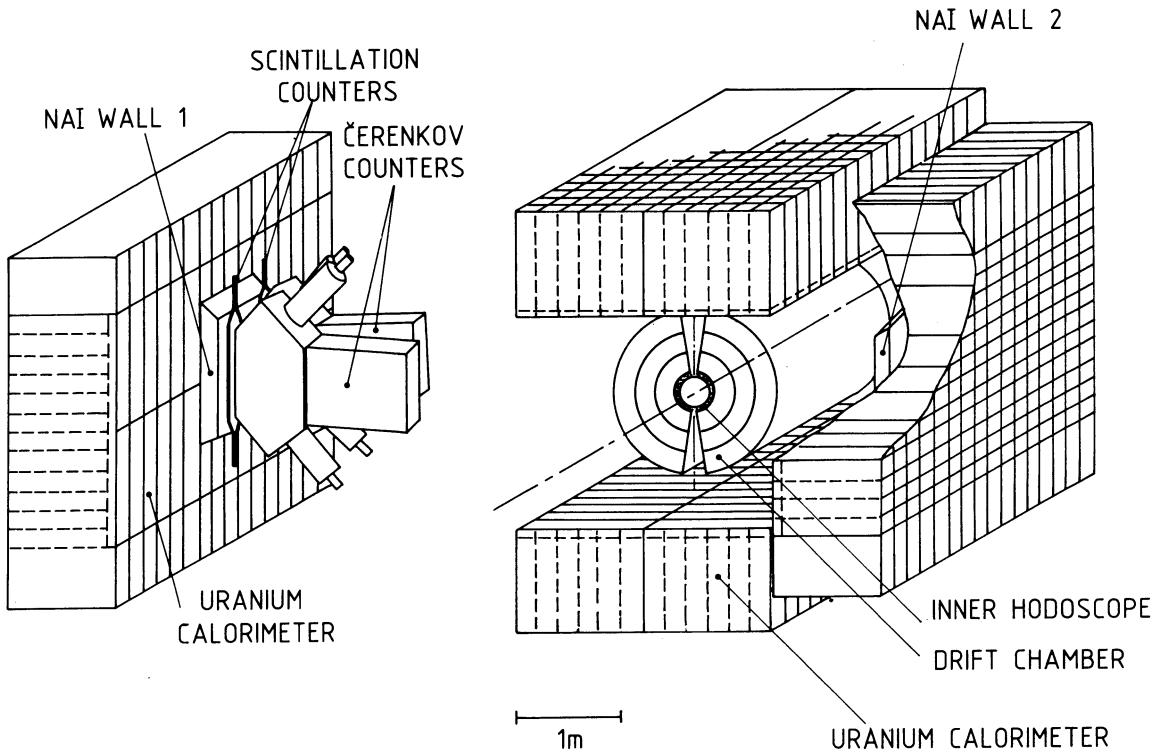

University of Lund

Department of physics

LUNFD6/(NFFL – 7037)/1987

31 March 1987

PRODUCTION OF POSITRONS WITH LOW TRANSVERSE MOMENTUM AND LOW – MASS ELECTRON – POSITRON PAIRS IN PROTON – PROTON COLLISIONS AT A CENTER – OF – MASS ENERGY OF 63 GEV.

VINCENT HEDBERG

The department of elementary particle physics
University of Lund
Sweden*

ABSTRACT

The production of inclusive prompt positrons in pp collisions at $\sqrt{s} = 63$ GeV and $y = 0$ has been measured over the P_T interval $0.08 < P_T < 1.0$ GeV/c. The e^+/π ratio rises with decreasing P_T to $\sim 1.6 \cdot 10^{-3}$ at $P_T = 0.1$ GeV/c. A measurement of low – mass e^+e^- pairs ($0.05 < m_{ee} < 0.60$ GeV/c^2) has also been performed. It is found that the observed rise of the e^+/π ratio can be explained by the low – mass pair continuum.

The origin of this pair continuum, which has been observed by several previous experiments, has so far been unclear. In order to obtain some new insight into the possible production mechanism a measurement of the production of single positrons and electron – positron pairs as a function of the associated charge multiplicity has been carried out. The results indicate that the production of low – P_T positrons (< 0.4 GeV/c) and low – mass pairs is proportional to the square of the mean multiplicity in the central region ($|y| < 1$). Such a quadratic dependence is not expected from final – state sources such as hadronic bremsstrahlung or hadronic decays, but is predicted by models where low – mass electron pairs are produced by interactions of constituents created during the collision.

* Present address: EP – div. CERN, CH – 1211 Geneve 23, Switzerland

CONTENTS

TABLES

FIGURES

1. INTRODUCTION

Inclusive lepton production in hadron–hadron collisions has been investigated extensively over the past decade. Following the initial observations of lepton–to–pion ratios at the level of $\sim 10^{-4}$ for large P_T at Serpukhov, Fermilab and the CERN Intersecting Storage Rings (ISR) [1]– [3] (see fig. 1), subsequent studies [4]– [16] have been only partially successful in elucidating all contributions to the measured yields. For transverse momenta $P_T > 2$ GeV/c, the strongest contributions are due to lepton pairs from the decay of the J/ψ and from the Drell–Yan continuum. In the intermediate regime $0.5 < P_T < 2$ GeV/c the semileptonic decay of charmed particles (mostly D) presents a dominant source of single leptons, although large uncertainties still exist in the absolute charm cross sections [13]–[16]. For P_T below 1 GeV/c down to 0.25 GeV/c, a rise in the e/π ratio with decreasing P_T has been reported in measurements from $\sqrt{s} = 4.5$ to 63 GeV [17]–[20].

Experimentally, the rise at low P_T has remained somewhat controversial [21]–[23] and in addition the interpretation of an increasing e/π ratio up to $4 \cdot 10^{-4}$ in this region needs further clarification. The two main known sources contributing to the e/π ratio at low P_T (< 0.5 GeV/c) are, as already mentioned, the semileptonic decay of charmed particles and, to some extent, internal conversion of bremsstrahlung radiated by charged hadrons [40]– [45].

A number of experiments have reported observations of a dilepton continuum with masses $m < 0.6$ GeV/c^2, i.e. below the ρ^0 and ω. This low–mass dilepton continuum has been seen both in $\mu^+\mu^-$ [25]– [33] and e^+e^- channels [34]–[39]. The production rate of these pairs is up to two orders of magnitude larger than what would be expected from the Drell–Yan process [117]. It is conceivable that the increase of the e/π ratio at low P_T is solely due to the low–mass electron pair continuum but this has not been confirmed in a conclusive way, since few experiments have been able to measure both the e/π ratio at very low P_T and the production of low–mass e^+e^- pairs. However, the low mass dilepton continuum is in itself not very well understood and even if the rise of the e/π ratio at low P_T could be connected to the low–mass pairs, the question about the origin of these leptons still remains.

It has recently been pointed out by Cerny, Lichard and Pisut [48] that information about the production mechanism of the low–mass e^+e^- continuum can be obtained by studying the associated charge multiplicity in a rapidity region close to that of the lepton pairs. If the dileptons are created after the final hadrons have been produced (e.g. by hadronic decays or hadronic bremsstrahlung), the mean number of dileptons per event will be proportional to the number of final hadrons, thus giving a constant value of the e/π ratio. In another class of models, the lepton pairs are produced over an extended volume at an early time during the collision when new quarks and anti–quarks have been created and the lepton production is enhanced by including interactions between the many quarks and anti–quarks pro-

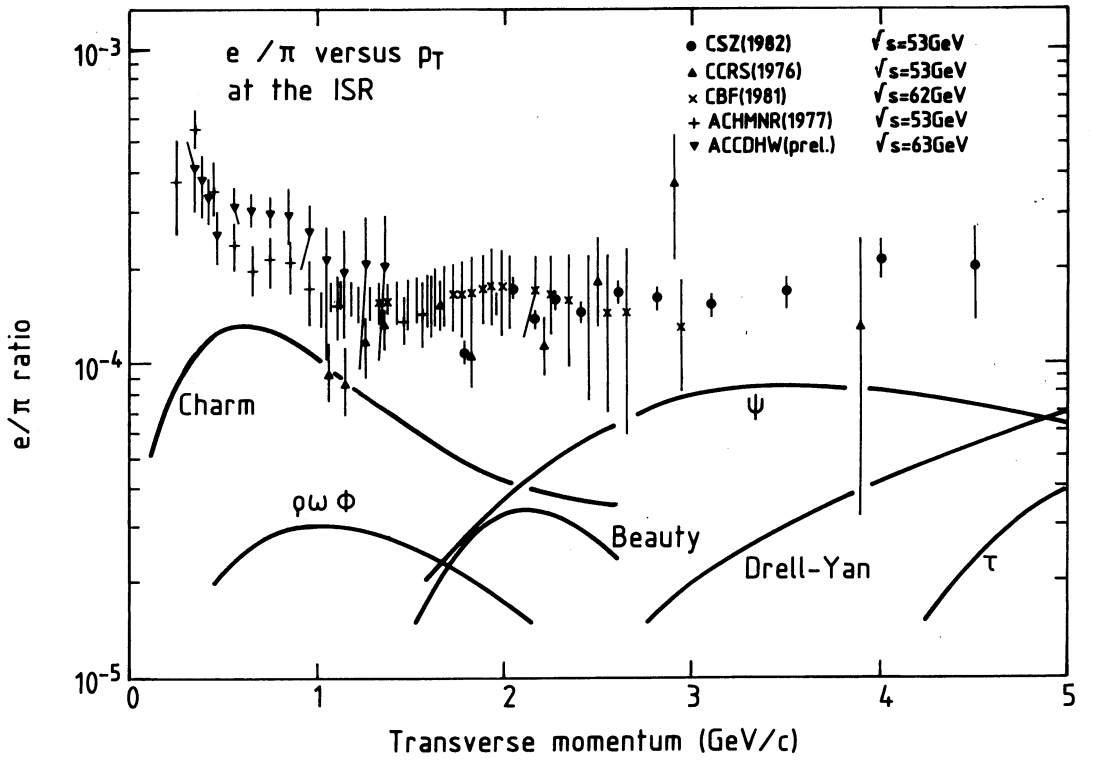

Figure 1: The e/π ratio versus transverse momentum. This compilation of ISR data was made previous to this experiment in 1982 [47].

duced in the hadron – hadron collision. The production rate of dileptons in these models should be proportional to the density of quarks times the density of antiquarks, i.e. proportional to the square of the charged particle multiplicity. This characteristic dependence is predicted by the the thermodynamic models [49] – [50] and the so – called soft annihilation model [51] which was originally proposed by Bjorken and Weisberg [52].

In view of this situation, the e/π ratio has been remeasured in pp collisions at $\sqrt{s}$ = 63 GeV and followed down to values of P_T lower than previously achieved. Since the ratio depends crucially on the proper background elimination, a combination of good experimental rejection and an extensive Monte Carlo simulation of the known sources was needed to make it possible to extract the prompt electron signal. The rise of the e/π ratio with decreasing P_T could not only be confirmed, but it was

found that it continues to a level of $1.6 \cdot 10^{-3}$ at $P_T = 0.1$ GeV/c. At $P_T > 0.4$ GeV/c the results agree with previous experiments. The strong rise observed definitely rules out explanations in terms of semileptonic charm decays, other known hadronic decays and hadronic bremsstrahlung.

The same event sample that was used in the inclusive single e/π measurement was later used in a study of the production of e^+e^- pairs in the mass range of 50 to 600 MeV/c^2. In this mass interval an excess of pairs above known sources was observed and this is the first time that the low–mass pair continuum has been studied at ISR energies and at masses less than 200 MeV/c^2. Although the pair measurement suffers from systematic uncertainties due to a large background subtraction, the magnitude of the observed pair signal is such that it can explain most of the low–P_T excess seen in the e/π measurement.

Finally, a measurement of the production of prompt positrons and e^+e^- pairs as a function of charged particle multiplicity has been performed. A significant difference was observed between the multiplicity dependence of the low–P_T positrons, which probably originate from the low–mass pair continuum, and the high–P_T positrons, which are attributed mainly to the decay of charmed particles. The direct measurement of the production rate of the low–mass pair continuum also indicated a quadratic rather than linear dependence of the pair cross section on the associated charged particle multiplicity. The conclusion, from the measured multiplicity dependence of the e/π and e^+e^- signal, is that a production mechanism of the low–mass dilepton continuum as described by the soft annihilation model and the thermodynamic models is favored over an explanation in terms of hadronic decays or hadronic bremsstrahlung.

Another aspect of these results is the suggestion that the phase transition between hadronic matter and quark matter in very high energy nucleus–nucleus collisions could be detectable by measuring the production rate of lepton pairs [53]–[58]. Amongst other features, a square dependence of this rate on particle multiplicity is predicted as one of the signatures for the quark–gluon plasma [54]. For this reason, it is of obvious importance to first understand the production mechanism of lepton pairs in ordinary hadron–hadron collisions.

The results presented below have been partly published in the following publications:

- PRODUCTION OF INCLUSIVE POSITRONS AT LOW PT IN 63 GEV PP COLLISIONS AT THE CERN ISR [59]
  V. Hedberg

- PRODUCTION OF PROMPT POSITRONS AT LOW TRANSVERSE MOMENTUM IN 63 GeV pp COLLISIONS AT THE CERN INTERSECTING STORAGE RINGS [60]
  The Axial Field Spectrometer Collaboration

- INCLUSIVE η PRODUCTION AT LOW TRANSVERSE MOMENTUM IN 63 GeV pp COLLISIONS AT THE CERN INTERSECTING STORAGE RINGS [61]
  The Axial Field Spectrometer Collaboration

- CORRELATIONS BETWEEN THE PRODUCTION OF PROMPT POSITRONS AT LOW TRANSVERSE MOMENTUM AND THE ASSOCIATED CHARGED MULTIPLICITY [62]
  The Axial Field Spectrometer Collaboration

2. THE APPARATUS

During the last year of the ISR (in 1983) when this experiment was performed, the Axial Field Spectrometer (AFS) [63] consisted mainly of a 2π Uranium – copper calorimeter (UCAL) and a large cylindrical drift chamber (DC) as shown in fig. 2 . These detectors were primarily designed to study jet phenomena. Two highly segmented NaI walls were positioned at opposite sides of the interaction making it possible to study direct photons and electrons. A barrel shaped hodoscope and two scintillator walls were used to define the event time which, among other things, was used in the time – of – flight (TOF) system. In addition, the AFS had a set of small drift chambers surrounding the beam pipes, used in a glueball search, and a muon arm consisting of two proportional chambers with an iron wall in between. However, the glueball drift chambers and the muon detectors were not used in this analysis. The data in this particular experiment was recorded during three dedicated ISR runs in which one calorimeter wall was retracted and a spectrometer arm consisting of two scintillation counters and two Cherenkov counters was installed. These additional counters were used to trigger on electrons.

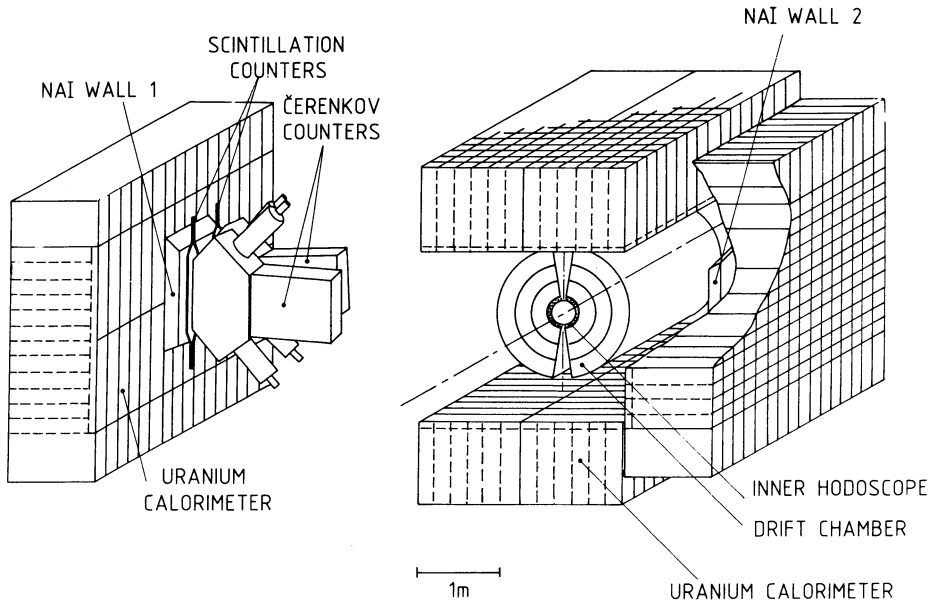

Figure 2: Description of the Axial Field Spectrometer. One calorimeter wall was retracted in this experiment so that a Cherenkov arm could be installed.

The AFS had a complex trigger system with which it was possible to run with up to 50 parallel triggers although typically the number of triggers was between 15 to 20. The data acquisition system consisted of 57 CAMAC crates containing various electronic modules (mostly ADCs,TDCs and DTRs) connected to two computers of type PDP – 11.

The AFS coordinate system is indicated in figure 3 . It was a right – handed system with the X coordinate pointing towards the center of the ISR while the Y coordinate pointed upwards. The Z axis was in the same plane as the two proton beams and the smallest angle between this axis and each beam was 7.4^{0}. In the polar coordinate system the azimuthal angle (ϕ) and the polar angle (θ) were defined in respect to the X,Y and Z axis in the usual way.

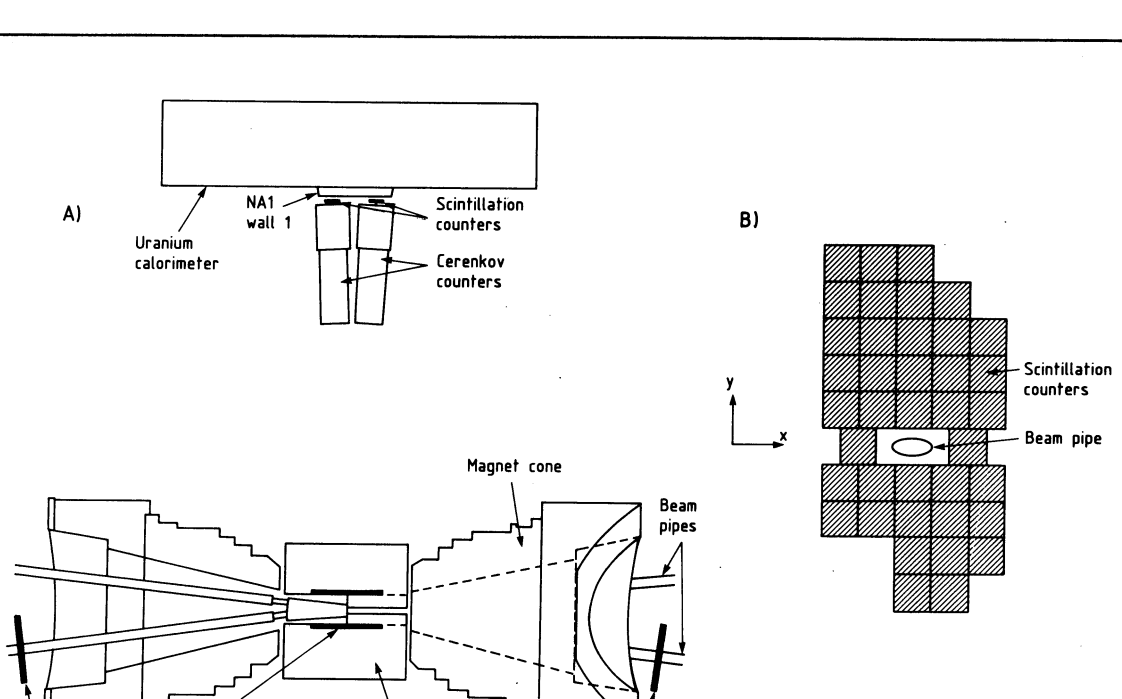

Figure 3: The position of the counters used in the TOF system.
A) Top view of the experiment.
B) Front view of one of the BB counter walls.

2.1 THE TIME – OF – FLIGHT SYSTEM

Two scintillation counters, with the dimensions 62x20x1 cm, were used in the TOF and trigger systems. They were positioned behind the Cherenkov counters ($y \approx 0$) at a distance of 4.9 m from the interaction point (see fig. 2 and 3 a). The acceptance for triggering positrons was limited by these detectors to $\Delta y = 0.036$ and $\Delta\phi = 6.4^0$. Each scintillator was viewed with two photomultipliers (PM) mounted at the top and bottom of the counter. The signals from the PMs were split and sent to ADCs, TDCs and the trigger system.

The beam – beam (BB) detectors consisted of two walls of box like scintillation counters surrounding the beam pipes downstream from the collision point and covering $2^0 < \theta < 20^0$ (as depicted in fig. 3 a and b). The inner hodoscope (IH) counter was a barrel shaped hodoscope consisting of 44 scintillators each with $\Delta\phi = 8^0$ surrounding the intersection region and covering $40^0 < \theta < 140^0$.

The hardware event time (T0) was derived from the signals of the inner hodoscope counters and the beam – beam counters, as described in section 2.6 below. The T0 signal was used, among other things, to start the TDCs that were later stopped by signals from the triggering scintillation counters. From these TDC measurements it was possible to calculate the time – of – flight of a triggering particle.

The BB counters had a better time resolution than the IH counters and it was required in the off – line analysis (see section 4.4) that the BB counters had fired in order to be able to calculate the time – of – flight with as good a resolution as possible. The rms of the measured TOF was 0.64 ns after corrections.

2.2 THE DRIFT CHAMBER AND THE MAGNET

The drift chamber [64] was placed in a magnet (fig. 3 a and 4 a) which provided an axial field with the nominal value of 0.5 Tesla. In this particular experiment the magnet was operated with a field of only 0.1 Tesla in order to make it possible to study low momentum electrons which at a higher field would have curled – up (and then been undetected).

The 1.4 m long cylindrical drift chamber extended from a radius of 0.2 m to 0.8 m and it was filled with 50% argon and 50% ethane at atmospheric pressure. The sense wires which ran parallel to the Z axis were arranged into four degree sectors in the azimuthal plane and into three crowns (fig. 4 b) in the radial direction. Fig. 4 c shows the positioning of the sense wires in two of the sectors. The three crowns had 14, 18 and 10 sense wires in each sector.

By drift time measurements the track position could be measured in the azimuthal plane while charge division was used to measure the Z position. The sense wires

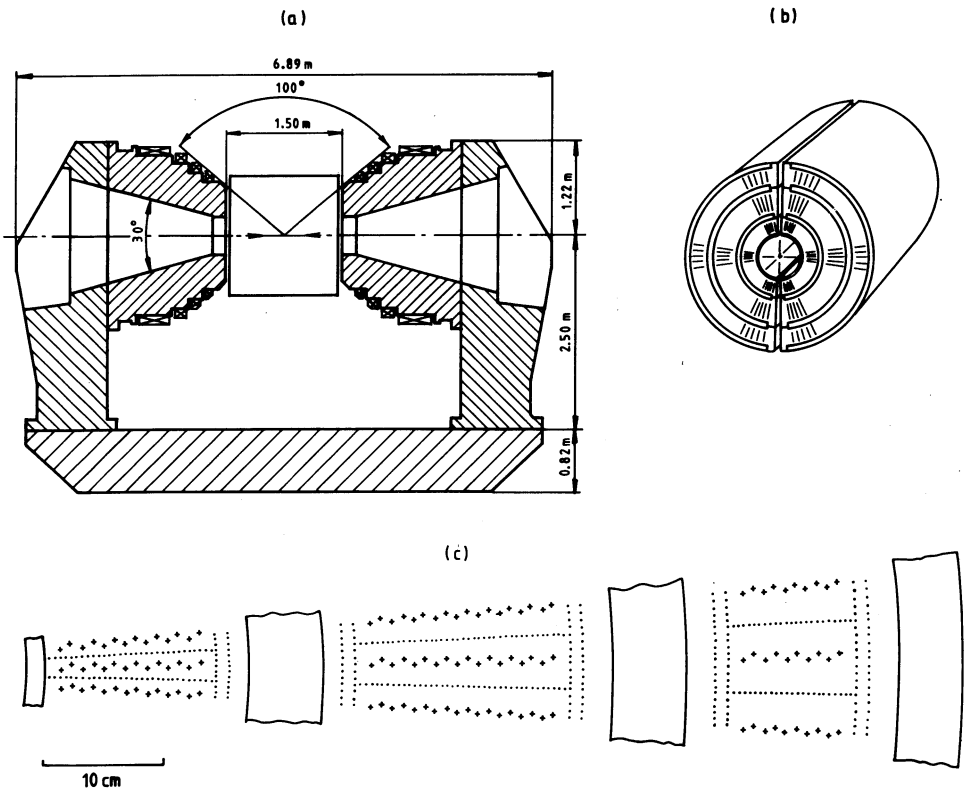

Figure 4: Description of the drift chamber and the magnet.
A) The position of the DC in the magnet.
B) Side view of the DC.
C) The wire positions in two DC sectors.

were staggered by ± 0.4 mm to resolve the left–right ambiguity. The energy loss (dE/dx) was measured with each sense wire through pulse height measurements. Offline, the lowest 70% of the pulse height measurements were used for each track in the dE/dx calculation (i.e. a truncated mean value was used).

The spatial resolution of the chamber was 230 μm (rms) in the azimuthal direction and 1.5 cm in the Z direction (charge division direction). The momentum resolution was, with the low magnetic field, $\Delta P/P \approx \sqrt{((0.1P)^2 + (0.01)^2)}$ where P is in GeV/c, i.e. the resolution changed from ~1% at 0.1 GeV/c to ~10% at 1 GeV/c.

2.3 THE CHERENKOV DETECTORS

During this experiment the Axial Field Spectrometer was equiped with two Cherenkov counters filled with CO_2 at atmospheric pressure as shown in fig. 2 and 3 a. The two detectors were mounted with a 60 mrad angle (with respect to the horizontal plane) in a way so that one Cherenkov had full geometrical acceptance for electrons down to a P_T of 70 MeV/c and the other Cherenkov had the same acceptance for positrons.

The length of the radiator was 140 cm and it had a momentum threshold of 18 MeV/c for electrons and 4.9 GeV/c for pions. The Cherenkov light was collected by spherical mirrors, each viewed by one photomultiplier, as shown in fig. 5 . By using LEDs mounted inside the Cherenkovs, it was possible to study the pulse height spectrum of the PMs without any beam. The high voltage was adjusted so that the pulse height corresponding to the one – photoelectron peak was the same for all PMs. The four output signals went to ADCs, TDCs and the trigger logic.

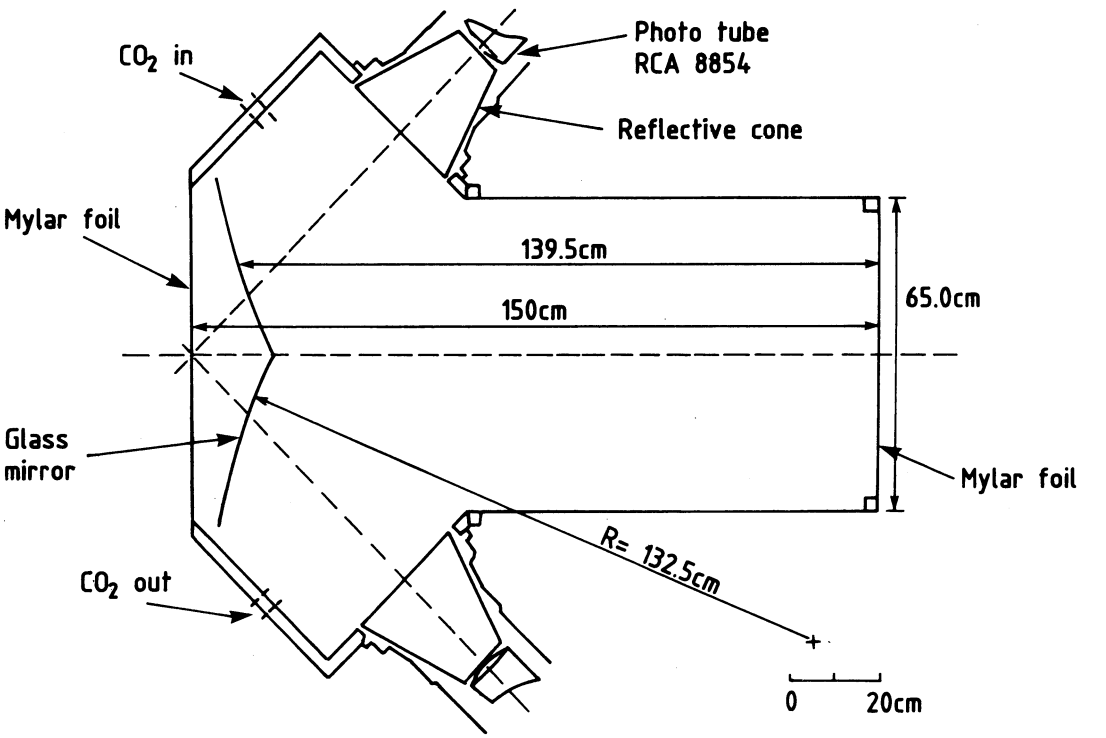

Figure 5: The Cherenkov detector.

2.4 THE NAI DETECTORS

Each NaI detector [65] consisted of 20x30 NaI crystals. The crystals were cut so that they would point towards the interaction region and they were optically isolated from each other. The geometrical structure of the detectors is shown in fig. 2 with wall 1 in its retracted position. The lateral front dimension of each crystal was 3.5x3.5 cm^2 and the average depth was 13.8 cm, corresponding to 5.3 radiation lengths (X_0). On the front face of each crystal a vacuum photodiode and a preamplifier were mounted. Photodiodes were used since they are not affected by a high magnetic field to the same extent as photomultipliers.

The spatial resolution of the detector was estimated with Monte Carlo calculations to be 0.6 cm but after NaI wall 1 had been retracted 4 m, its crystals did not point any longer towards the interaction region and this probably worsened the spatial shower resolution somewhat. The energy resolution for electrons at 1 GeV was measured in a test beam to be 9%.

2.5 THE URANIUM CALORIMETER

The Uranium calorimeter [66] was built up by towers with a surface area of 20.0x20.8 cm^2 and an absorber depth of 80 cm. Each calorimeter wall consisted of 12x16 towers. The towers were divided longitudinally into an electromagnetic part (6 X_0 deep) consisting of Uranium and scintillator plates and a hadronic part (3.8 λ deep) with Uranium, Copper and scintillator plates (as shown in fig. 6). In the four corners of the uranium calorimeter, copper–scintillator calorimeters were installed to minimize leakage.

The scintillators were read out with wavelength shifters, two for the electromagnetic part and two for the hadronic part of the tower. Each of the four wavelength shifters were connected to PM tubes with the dynode signals going to the trigger system (the VFB) and the anode signals to ADCs. In this experiment the normal 2π azimuthal coverage was reduced because of the retracted wall. The rapidity coverage of the remaining three calorimeter walls in the centre–of–mass varied with azimuth from $|y| < 0.7$ to $|y| < 1.2$ because of the detectors box like shape.

The advantage of a uranium–scintillator calorimeter is the nearly identical response to hadrons and electrons due to compensation through induced fission and the high energy resolution. The calorimeter in this experiment had an energy resolution of $\sigma(E)/E = 0.36/\sqrt{E}$ for hadrons and $\sigma(E)/E = 0.16/\sqrt{E}$ for electrons and a spatial resolution at normal incidence that was ~1 cm for electromagnetic showers and ~3 cm for hadronic showers. The ratio of electron to hadron response was 1.11 .

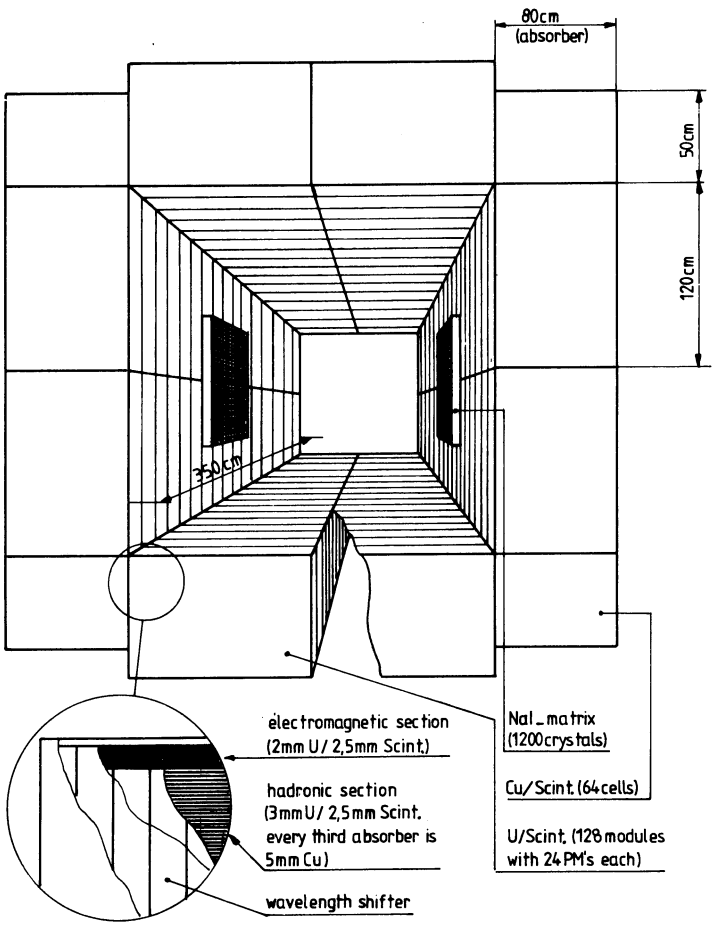

Figure 6: Description of the Uranium calorimeter.

2.6 THE TRIGGER SYSTEM

The AFS experiment had a complex trigger system with which data could be recorded using a large number of different triggers at the same time. The main part of the trigger system, the very fast bus (VFB) [67], was a special purpose electronic system with which the signals from the UCAL could be used to trigger on either total energy or localized energy in the calorimeter. Also signals from other parts of the experiment other than the UCAL went to the VFB where the final trigger configuration was defined. Only the part of the trigger system that was used in this experiment will be described below.

The data was taken with five different triggers, two selecting pions and three selecting electrons. The pion triggers (PI) required a coincidence between a signal in one of the scintillation counters, positioned behind the Cherenkov counters, and the event time. The latter was defined by the beam – beam counters positioned around the beam pipes downstream from the spectrometer and by the inner hodoscope counters which surrounded the intersection region at large angle. The first electron trigger, the minimum bias trigger (MB), required a coincidence between the event time, a hit in one of the scintillators and a signal from the corresponding Cherenkov counter. Since the signals from the scintillation counters would be accepted even if the pulse height was very low, it was assumed that the trigger efficiency of these counters was the same for electrons and pions. It was also assumed that the trigger efficiency of the Cherenkovs was a 100% for electrons (a test beam measurement using pion beams showed a 100% efficiency above the Cherenkov threshold). However, this assumption could lead to a slightly underestimated value of the e/π ratio. In section 2.3 it was mentioned that the two Cherenkov counters were mounted with different angles with respect to the horizontal plane. This resulted in a full geometrical acceptance for electrons in one of the Cherenkovs while the same was true for positrons in the other detector. The inefficiency for particles with the "wrong" charge could be calculated by dividing the P_T spectrums of triggering electrons and triggering positrons (from γ conversions) which had traversed the same Cherenkov counter (see fig 7 a).

In order to be able to trigger on electrons with higher momentum, the NaI detector was used in the so – called PT trigger. This trigger had the same requirements as the MB trigger and in addition a requirement of a minimum energy deposition in the NaI detector. The efficiency for this trigger was calculated with an event sample in which the NaI detector was not in the trigger but where the signals from the PT trigger were recorded so that the P_T spectrum of trigger electrons with and without the PT trigger requirement could be compared. With the PT trigger it was possible to select electrons with $P_T > 0.2$ GeV/c with more than 50% efficiency (see fig. 7 b).

The third electron trigger (the ETOT trigger) used the total energy deposited in the Uranium calorimeter together with the requirement of the MB trigger. With this trigger, events with a total energy above a threshold of $\sim$ 8 GeV were selected. A pion trigger with the same requirement on the energy in the UCAL was used together with this electron trigger.

Figure 8 describes, in a schematic way, the different parts of the trigger system that were used in this experiment. The T0 signal was derived from the IH counters or from the BB counters if no signals were generated in the IH. The 44 scintillators that made up the barrel shaped inner hodoscope were read out in both ends with PM tubes and the signals were discriminated. The signals then went to meantime units and subsequently to a logic unit which generated a signal if at least two scintillation counters were hit. The signals from the two BB counter walls were discriminated and then put into two logical OR units (one for each wall). The output from

each OR was put in coincidence so that at least one hit in each BB wall was required in order for a BB signal to be generated. A pretrigger was generated if a T0 signal was present at the input of the PRE AND gate at the same time as a signal from either the scintillation counters or the Uranium calorimeter.

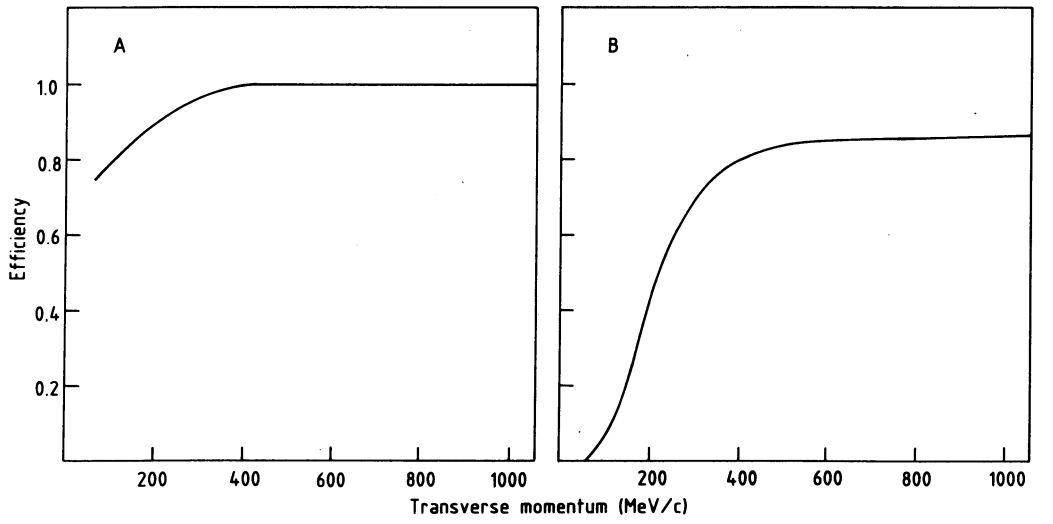

Figure 7: The trigger efficiency.
A) Efficiency due to geometrical acceptance.
B) The efficiency of the PT trigger.

The pretrigger started the gate generator which provided gates, a busy signal to the data acquisition system and a clock pulse for the VFB. After the event had been read by the computer a reset signal was sent from the PDP to the gate generator which sent clear signals to the data acquisition system. If the trigger was aborted in the VFB, the reset signal would instead be generated by this unit.

If the UCAL information was used, the pretrigger was generated from the analogue bi–polar ETOT signal (coming from the UCAL summing logic) by a so–called zero–crossing unit which in effect was a discriminator that was fired when the input pulse was at its maximum negative value, if the maximum value was above the discriminator level. The output from the discriminator was put in coincidence with an IH signal and the resulting signal was used in the pretrigger.

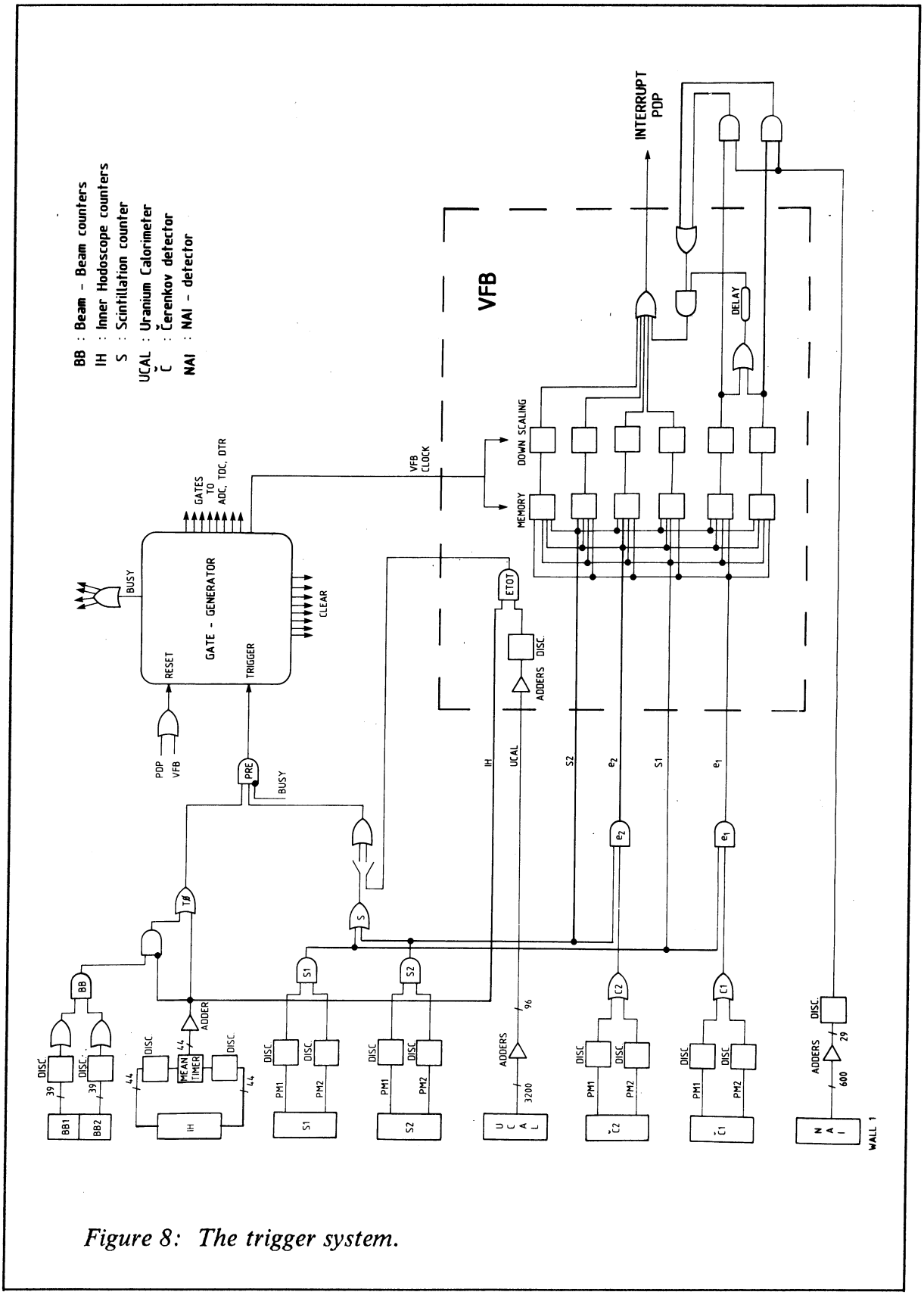

Figure 8: The trigger system.

If the UCAL was not used in the trigger, the pretrigger was generated from the scintillation counters by taking the coincidence of the signal from both PM tubes in each counter (thus creating the S1 and S2 signals) and subsequently using the logical OR of these signals in the pretrigger. The S1 and S2 signals were also used in the VFB to define the pion triggers. The electron triggers (e1 and e2) had a requirement of a signal from at least one of the PM tubes in a Cherenkov counter in coincidence with the corresponding S signal. Both the pion and electron signals addressed a set of memories in the VFB. If one of the addressed memories had been loaded with the binary value one, an output signal was generated. These signals could then be downscaled, i.e. only one out of a certain number of signals would be allowed to continue and create a trigger.

Table 1: The composition of the different triggers.

name	**pretrigger**	**first level**	**second level**
MB – 1	T0·(S1 + S2)	S1·C1	–
MB – 2	T0·(S1 + S2)	S2·C2	–
PT – 1	T0·(S1 + S2)	S1·C1	NaI
PT – 2	T0·(S1 + S2)	S2·C2	NaI
ETOT – 1	T0·ETOT	S1·C1	–
ETOT – 2	T0·ETOT	S2·C2	–
PI – 1	T0·(S1 + S2)	S1	–
PI – 2	T0·(S1 + S2)	S2	–
PI(ETOT) – 1	T0·ETOT	S1	–
PI(ETOT) – 2	T0·ETOT	S2	–

The pion and electron triggers which did not contain any NaI information would send an interrupt from the VFB to the PDP providing the triggers survived the downscaling requirement. The PT trigger, which was a second level trigger, required a signal from the NaI detector. The signals from the 600 photodiodes in NaI wall 1 were summed up into row sums. If the total signal from two neighboring rows was larger than a computer controlled discriminator value, a NaI trigger signal would be generated. This signal took a long time to create and the coincidence between the first level electron trigger and the NaI signal was therefore done outside of the VFB. When this second level trigger had been created it went back into the VFB where it produced an interrupt for the PDP. If no first or second level trigger

was made in the VFB an abort was send to the gate generator. Table 1 shows the requirement for the different triggers.

3. DATA TAKING, RECONSTRUCTION AND DATA REDUCTION

The total event sample consisted of about three million events (see table 2). Most of the events originated from Dalitz decays and photons converting in the beam pipe, the inner hodoscope, or the drift chamber wall. All of the events were processed through the AFS track–finding and track–and–vertex fitting programs. The computer processing time needed for this operation was so large that it could not be done on the CERN mainframe computers and thus two 168/E emulators were kept busy with this task for more than 22 weeks. After this stage the event sample was reduced by a series of cuts. To begin with, all tracks in the drift chamber were extrapolated through the magnetic field to a distance of 5 m from the intersection. The event was kept for further analysis if one and only one track in the event could be extrapolated to a fiducial area around the triggering scintillation counter ($X = -500$ cm, $-52 < Y < 52$ cm, $-20 < Z < 60$ cm or $-60 < Z < 20$ cm). The track that reached the fiducial area was defined as the trigger track. In the event sample where at least one trigger track could be found, about 2–3% of the events had more than one track that could be extrapolated to the scintillation counters. However, most of these events had been triggered by a zero–mass e^+e^- pair from a γ conversion.

Table 2: The number of events recorded with the different triggers.

Trigger	Number of events
MB	810,000
PT	1,160,000
ETOT	812,000
PI	115,000
PI(ETOT)	90,000

A set of requirements was made on the trigger track: the χ^2 of the track–fit divided with the number of degrees of freedom had to be less than 4.5, the length of the trigger track measured in the drift chamber was required to be larger than 33 cm and the starting point of the trigger track had to be less than 20 cm from the intersection. Only events where the trigger track had a P_T larger than 50 MeV/c were kept since the Cherenkov detector was not fully efficient for tracks with a P_T less

than 70 MeV/c. The invariant pair mass was calculated between the trigger track and all other tracks in the drift chamber with opposite charge (assuming both of the tracks to be electrons). The event was disregarded if there was a second track in the event which could be combined with the trigger track to form an invariant mass that was less than 40 MeV/c^2. This requirement removed a large fraction of events triggered by converted photons or electrons from Dalitz decay. The total reduction of data from these cuts was a factor of $\sim$ 8. When this data reduction had been done, the events were processed through the shower reconstruction programs of the NaI and UCAL detectors.

4. ELECTRON IDENTIFICATION

Since the e/π signal, which is measured in this experiment, is in the order of $2 \cdot 10^{-4}$ it is essential to have a very good capability of identifying electrons. For this purpose four different detector systems were available with which independent measurements could be performed in order to be able to identify the triggering particle. In chapter 2 each detector system was described and in the following one the calculations of pion rejection and efficiency corrections will be presented.

4.1 THE dE/dx MEASUREMENT

The truncated mean value (70 %) of the pulse height measurements along the trigger track was used as a measurement of the energy loss (dE/dx) in the drift chamber. The dE/dx, measured in the beginning of the analysis, is depicted in fig. 9 as a function of momentum, for PT and PI triggers separately. The same thing is plotted in fig. 10 after applying all cuts in the analysis except the dE/dx cut. The curves in fig. 9 are from a calculation of the truncated mean obtained by a Monte Carlo simulation based on a model by Allison and Cobb [68]. The cut on dE/dx, that was imposed on the trigger track, was momentum dependent in such a way that it resulted in a constant cut efficiency for electrons. The cut removed events where the trigger track had either a too low or a too high dE/dx, i.e. it was made on both sides of the electron band.

In fig. 9 a and 10 a there are many trigger tracks with a dE/dx much larger than what would be expected from a single electron. These measurements are mainly due to $e+e-$ pairs which have not opened up sufficiently so that the ionization produced by the two electrons is picked up by the same sense wires. A trigger track was called "doubly ionizing" if there had been a second electron passing through the same DC sector as the trigger track. The dE/dx measured for the trigger track was then twice the dE/dx expected for a single electron. However, a trigger track was also called doubly ionizing even if a second track only partly shared a DC sector with it. In this case the dE/dx measured for the trigger track was larger than that of a single electron but lower than that of two electrons.

The rejection and the efficiency of the identification by dE/dx was calculated with the MC mentioned above. This MC, which was based on the Allison – Cobb model, had two parameters that had to be determined by data. The first parameter was the scale of the truncated mean value, i.e. a normalization of the calculated mean value (given in KeV) to the measured mean value (in ADC counts) had to be performed. The second parameter was the mean number of measurements that was used to calculate the truncated mean, i.e. the mean number of signals from sense wires that had been used to calculate the dE/dx. This parameter determined the width of the dE/dx distribution.

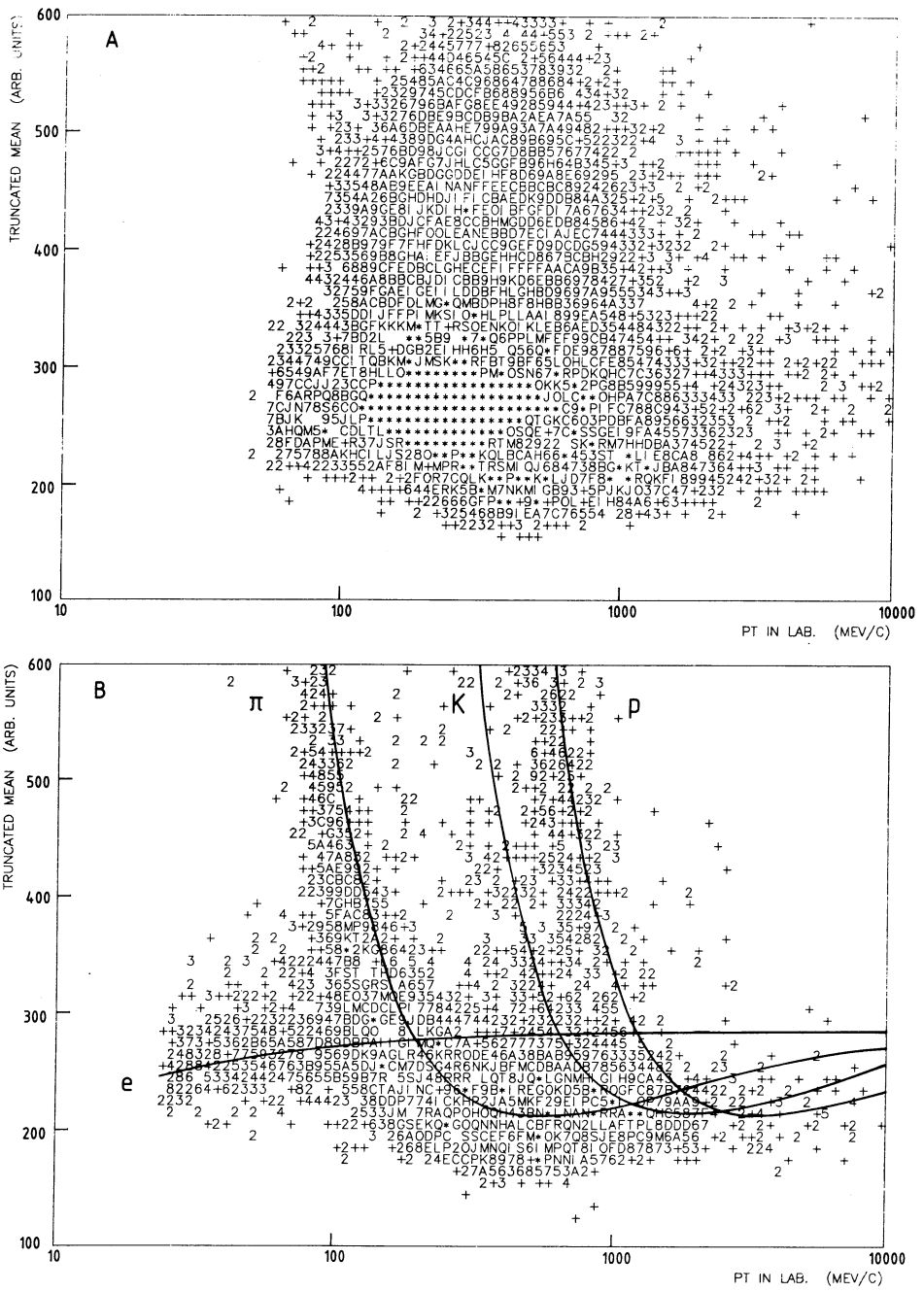

Figure 9: The dE/dx of trigger tracks plotted versus P_T. This measurement was performed at an an early stage of the analysis.
A) PT triggered data.
B) PI triggered data. The curves show the results of a MC calculation.

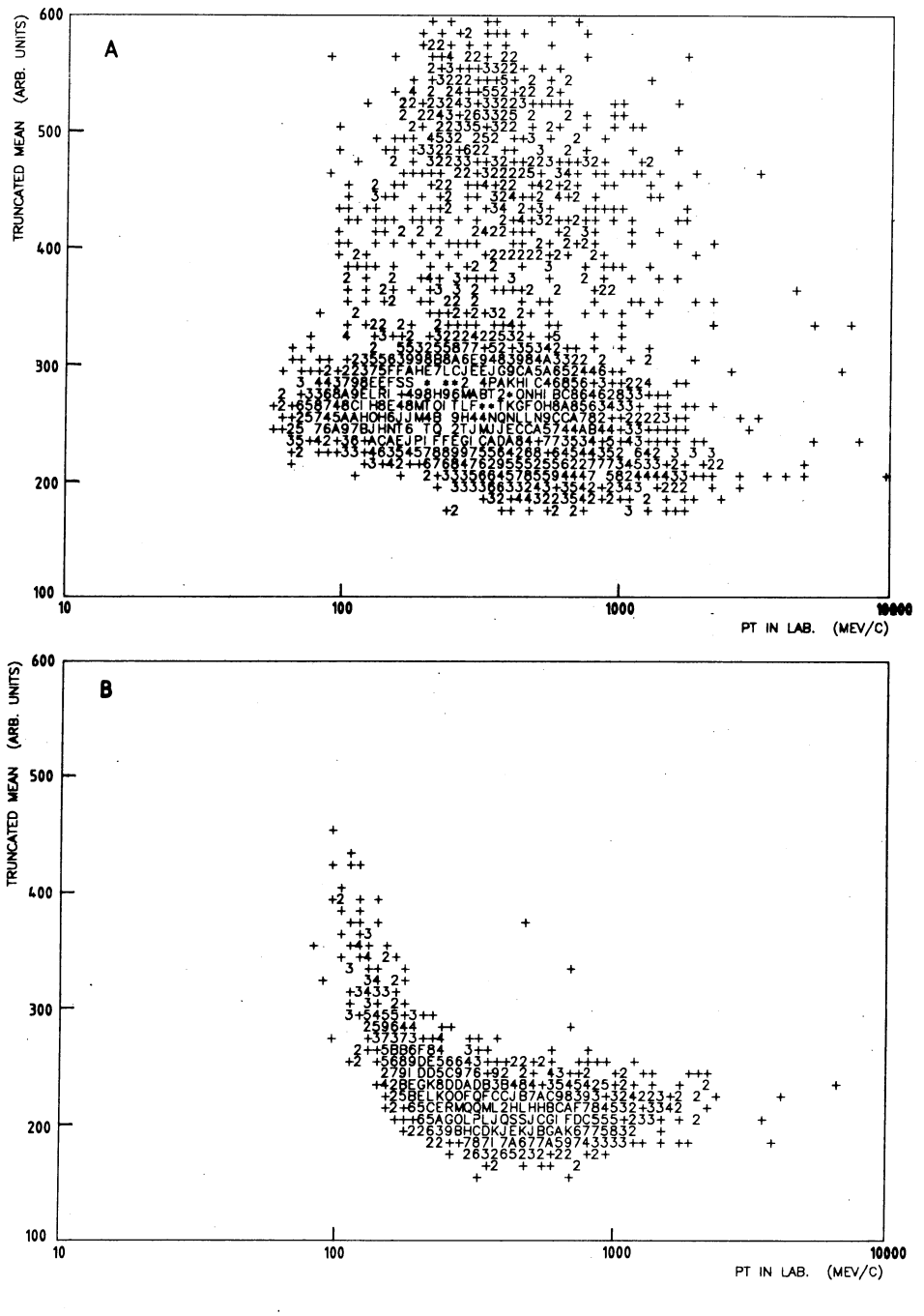

Figure 10: The dE/dx of the trigger track measured after all cuts in the analysis (except the dE/dx cut).
A) PT triggered data.
B) PI triggered data.

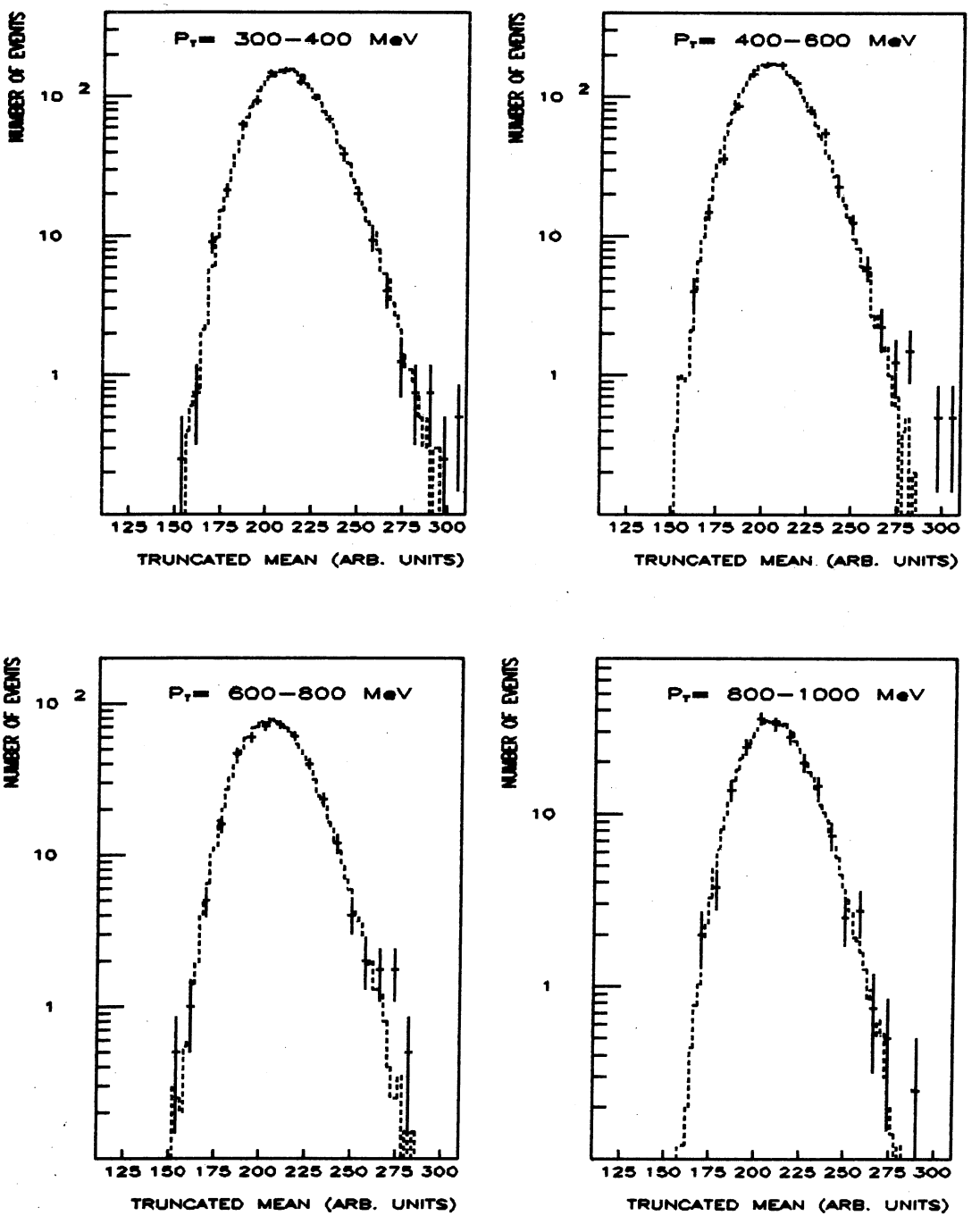

Figure 11: The dE/dx of pions in data and MC (for 4 P_T bins). The dashed line refers to the MC calculation and the crosses to the data.

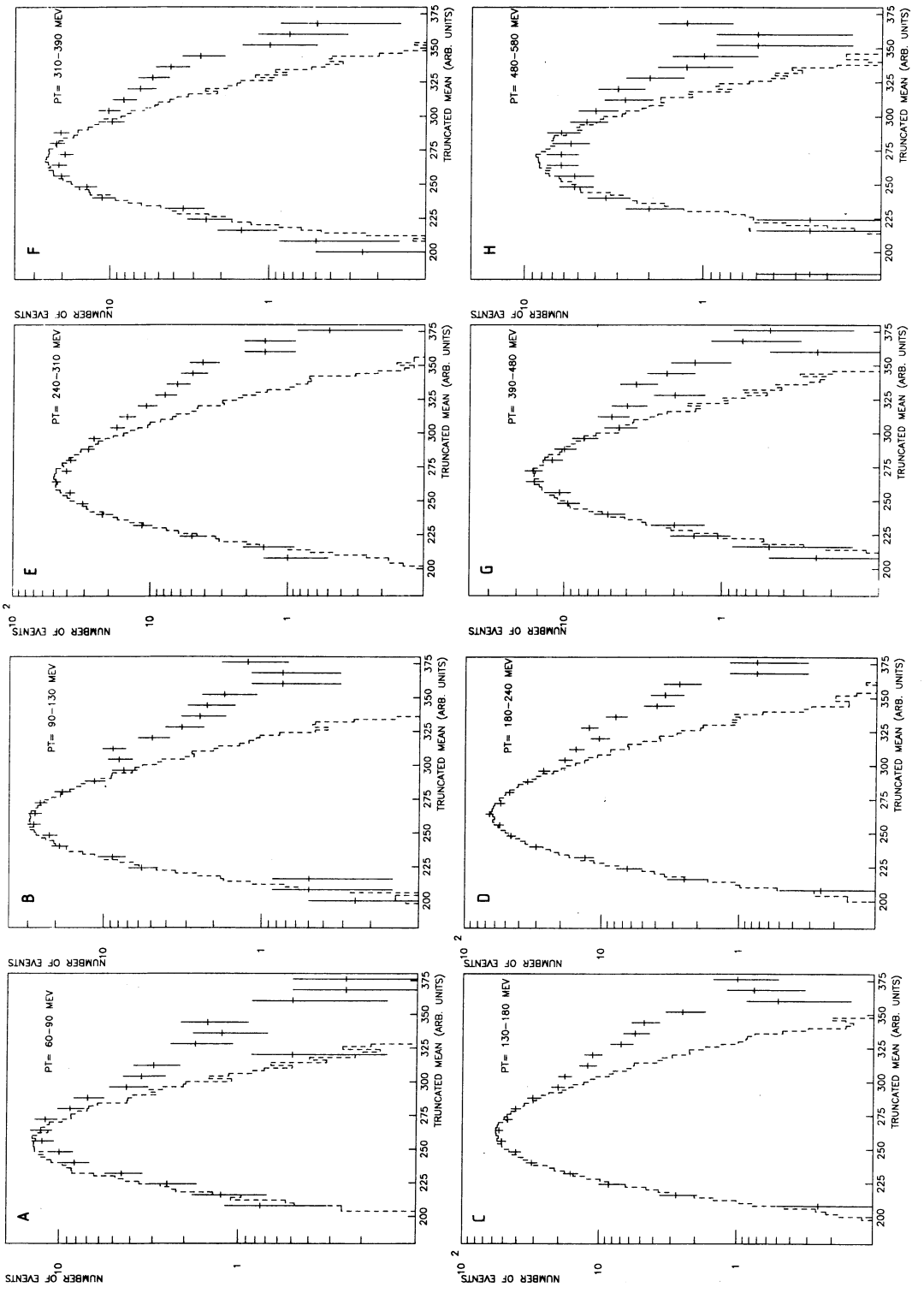

Figure 12: The dE/dx of electrons in data and MC (for 8 P_T bins).

A pion sample was used to fix the two parameters. After the sample had been cleaned up by a hard time–of–flight cut it was divided into four momentum bins in the region where the pions are minimum ionizing. The data in the lowest momentum bin was used to obtain the truncated mean value and the mean number of dE/dx measurements along a trigger track. The values of these two parameters were then incorporated into the MC. In fig. 11 the dE/dx distribution from the MC calculation and the pion data are compared. There is an excellent agreement between the tails of the distributions in the data and the MC. This is important since the calculation of the rejection is sensitive to these tails. It is also clear from fig. 11 that the high tails of the truncated mean distribution, although much smaller than in the original Landau distribution, are not well fitted with a Gaussian distribution.

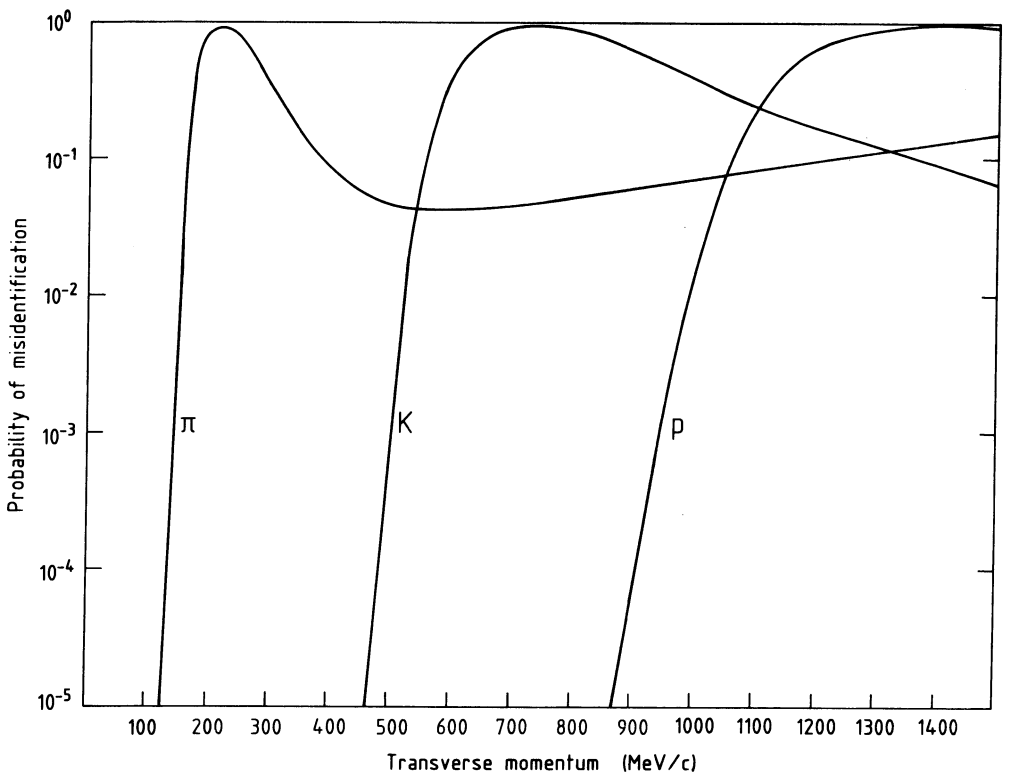

Figure 13: The hadron rejection achieved by the dE/dx requirement.

In principle both the MC and the pion sample could be used to calculate the rejection. In practice, however, the MC was used because of the possibility of a small kaon and proton contamination of the pion sample and in addition the MC made it possible to obtain results with negligible statistical errors. Another advantage with the MC was that the rejection of pions, kaons and protons could be estimated separately while in the data only a pion sample was available (i.e. the kaon and proton rejection could not have been estimated without the MC). The results of the MC calculation of the hadron rejection due to the dE/dx cut is illustrated in fig. 13 .

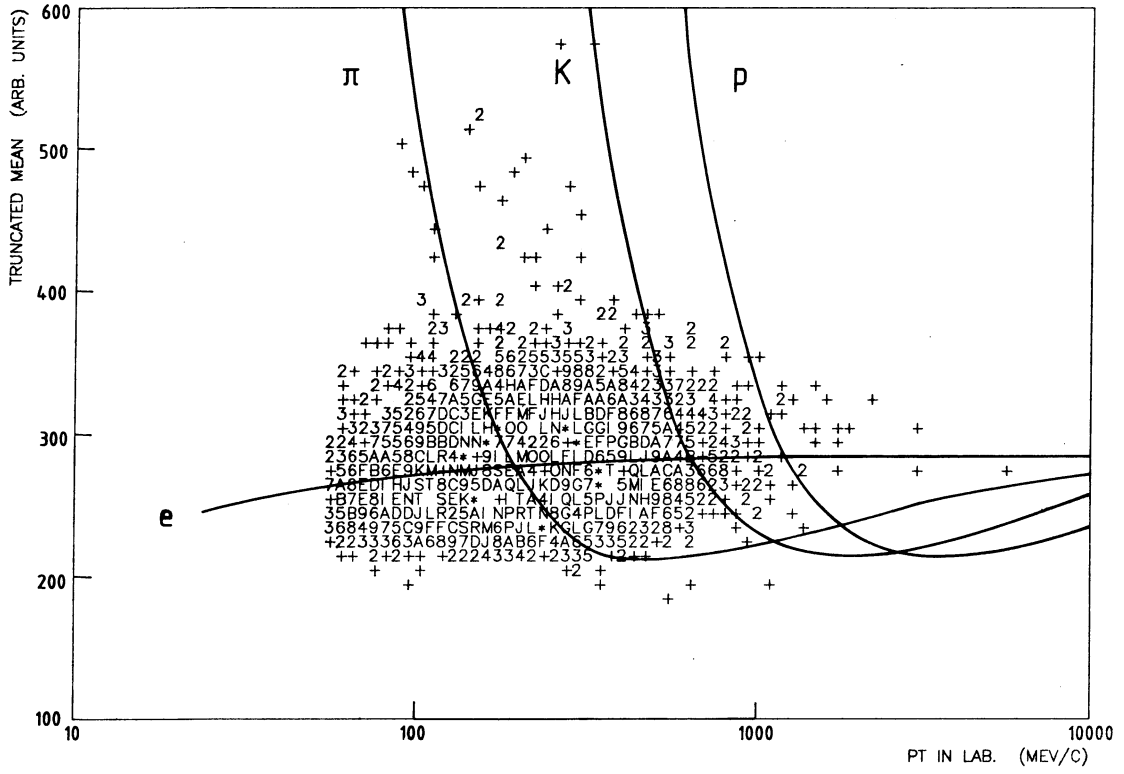

Figure 14: The dE/dx measured for tracks from low – mass pairs.

After the two parameters in the MC had been fixed by using the pion sample, it was possible to calculate the cut efficiency for electrons. However, it was desirable to first check the dE/dx distribution predicted by the MC with the distribution from a sample of electrons. For this study a sample of trigger electrons was selected, where the trigger track formed a low – mass pair ($m < 40$ MeV/c^2) with another track in the drift chamber. This sample consisted mostly of electrons from γ conversions and

was therefore free from any hadron contamination. In order to remove doubly ionizing trigger tracks, it was required that the two tracks in the pair were well separated when they left the drift chamber. This requirement removed a large fraction of the doubly ionizing tracks but not all. The dE/dx for this sample is plotted in fig. 14 .

This sample was divided into P_T bins like the pion sample and compared with the MC. From this comparison it was concluded that the MC overestimated the separation between the minimum ionizing pions and the electron band by 6%. For this reason the pions and the electrons had to be normalized separately to the data. The reason for the disagreement between data and MC is not well understood. It could either be due to an imperfect model or to an experimental problem like impurities in the chamber gases.

The dE/dx of electrons in data and MC is plotted in fig. 12 after normalization. The agreement between data and MC is very good for the lower tails of the distributions but at high dE/dx the agreement is not perfect because of the doubly ionizing problem. Even if the widths differ, the agreement between the mean value in the data and the MC show that the relativistic rise is calculated correctly in the MC. The dE/dx cut that was finally used in the analysis had, according to the MC calculation, a 94% efficiency independent of P_T.

4.2 THE ENERGY MEASUREMENT BY THE NaI DETECTOR

To be able to measure the energy of the trigger electron in the NaI detector it was necessary to first find the shower that corresponded to the trigger track which had been detected by the drift chamber. In the Z direction only the information from the NaI was used and it was required that the shower candidates were in the half of the NaI wall that corresponded to the triggering scintillation detector. The trigger track measured with the DC was extrapolated to the NaI wall, this extrapolation, however, had a bad resolution in Z. In particular if there were two tracks in the same sector, the Z fit would have a large error. In the Y direction a measurement by the scintillator (Y_S) was used in addition to the measurement of the shower position (Y_{NaI}) and the extrapolated track position (Y_{DC}). The position of the track in the scintillator was calculated with the following formula:

$$Y_S = c\cdot(T_1 - T_2)/(2\cdot n) \qquad \text{where}$$

T_1 the time measured with the upper scintillator PM;
T_2 the time measured with the lower scintillator PM;
c the velocity of light;
n the refractive index of the scintillator.

The difference between the shower position in the NaI and the Y position measured with the scintillator was required to be less than ± 16 cm which corresponded to a cut of ± 2.5 standard deviations in the $Y_S - Y_{NaI}$ distribution.

The next step was to compare the extrapolated Y position with the Y position of the shower (i.e. make a cut on the $Y_{DC} - Y_{NaI}$ distribution). In this case the width of the ΔY distribution would depend on particle type and momentum because of multiple scattering. For this reason a momentum dependent cut was introduced (assuming a Gaussian approximation for multiple scattering, as described in section 6.5) so that the cut inefficiency was the same for pions and electrons and independent of momentum.

If two or more showers satisfied the above criteria then the shower with the highest energy was chosen as the one belonging to the drift chamber track. The shower matching described above was done on both electron and pion triggers. One reason for this was that the scintillation counters were sitting close to the edge of the active area of the NaI wall and it was possible for a small fraction of trigger particles to pass through the scintillators but not the NaI crystals. Since it was required that a NaI shower could be found for both electron and pion triggers, this and other systematic uncertainties cancelled to a large extent when the e/π ratio was calculated.

In order to be able to reject pions, a cut on the energy deposited in the NaI detector was done. This cut was, of course, only made on electron triggers. For tracks with a P_T larger than 335 MeV/c it was required that the NaI energy was larger than 120 MeV (the minimum ionizing peak was at 80 MeV). Tracks with a P_T less than 335 MeV/c were submitted to a P_T dependent cut so that the cut efficiency was constant as a function of P_T. An attempt was made to use the information derived from the electromagnetic part of the calorimeter situated behind the NaI wall. It was found that the pion rejection (at $P_T < 1$ GeV/c) could not be improved significantly, without lowering the efficiency, by adding the information from the UCAL.

Table 3: The efficiency of the NaI energy requirement.

Trigger	**Efficiency**
MB – 1	88%
MB – 2	91%
PT – 1	98%
PT – 2	97%
ETOT – 1	88%
ETOT – 2	87%

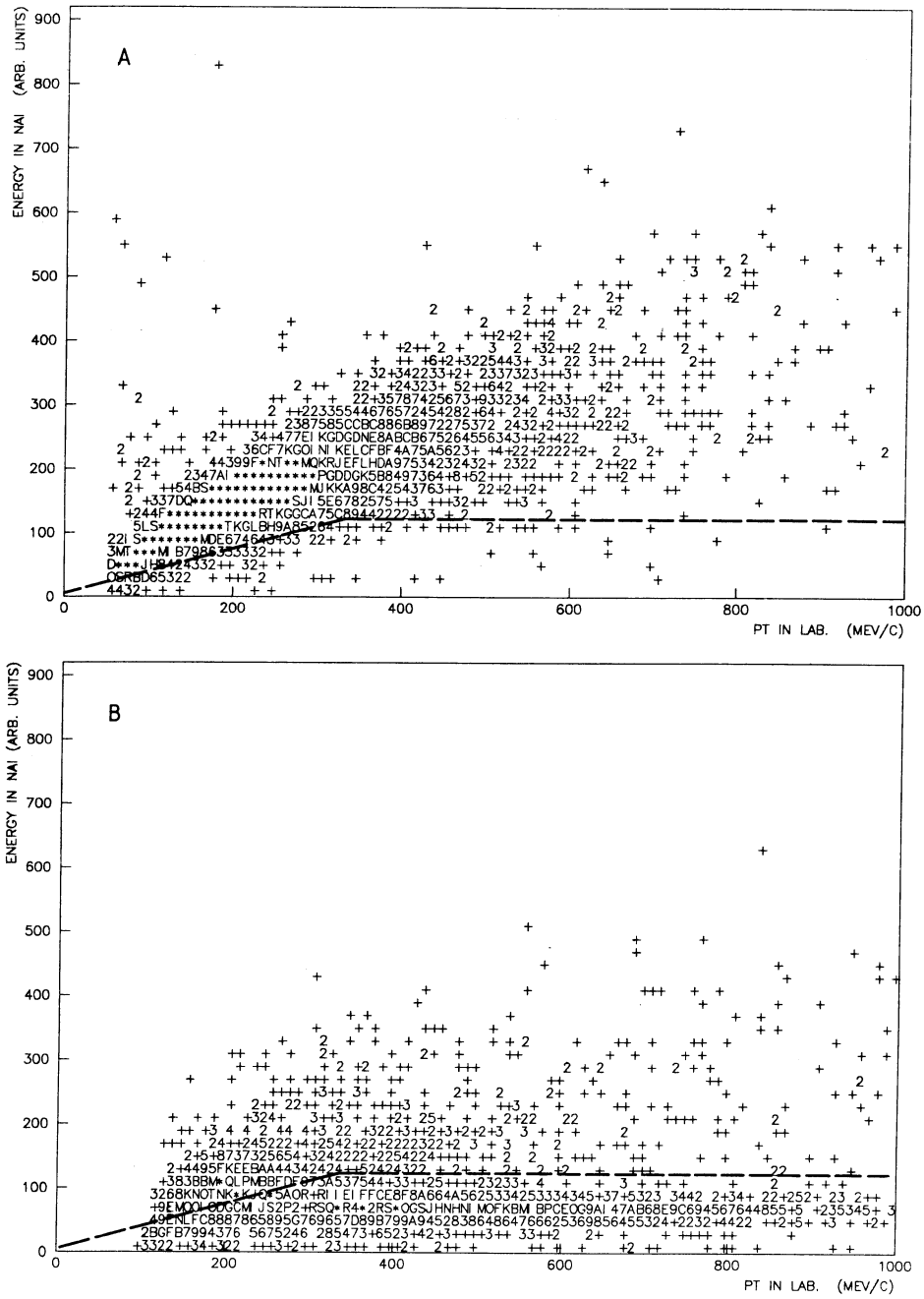

Figure 15: The energy deposited in the NaI plotted versus the P_T measured in the DC. The dashed line shows how the cut was applied.
A) PT triggered data.
B) PI triggered data.

Figure 15 shows the energy deposited in the NaI versus the momentum measured with the drift chamber. The cut (applied only on electron triggers) is indicated as a dashed line in this figure. In the electron case there is a linear dependence of the energy on the momentum since most of the electromagnetic shower is contained in the NaI wall at these low energies. The low momentum pions ($P_T < 200$ MeV/c) are also, to a large extend, contained in the wall and show the same linear relationship as the electrons. At higher momentum the pions become minimum ionizing and start to deposit a constant amount of energy (80 MeV) in the wall.

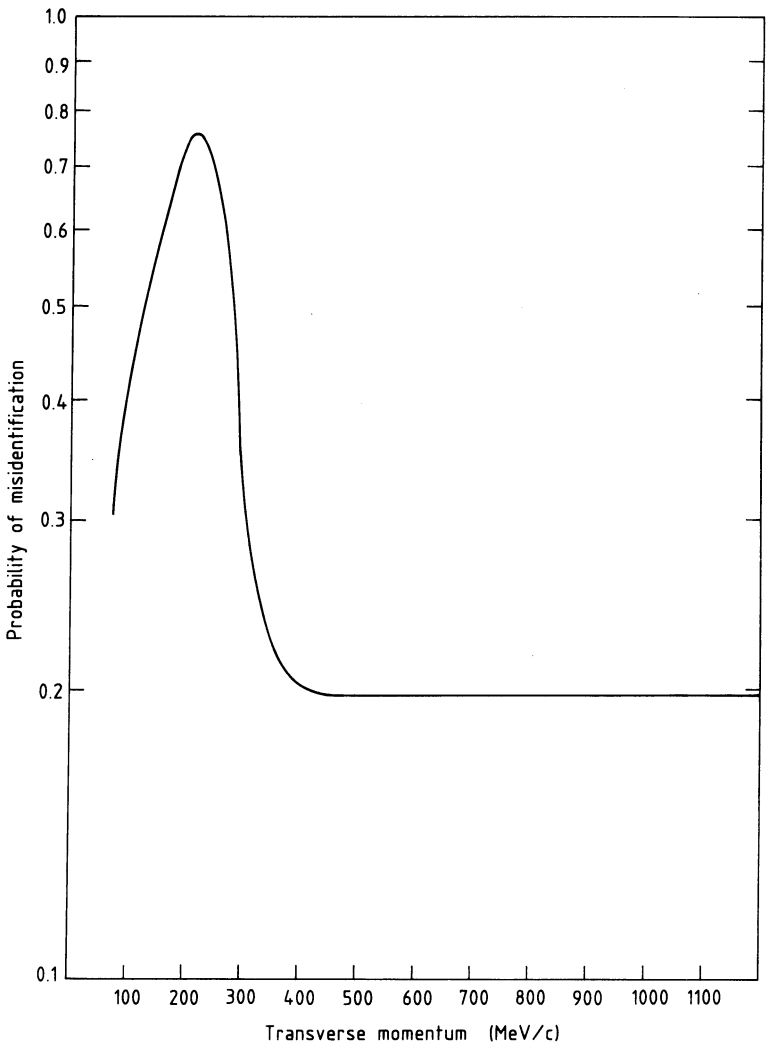

Figure 16: Hadron rejection obtained with the NaI energy requirement.

The cut efficiency was calculated with a sample of low – mass electron – positron pairs submitted to various hard pion rejection cuts (excluding the NaI cut). The result of these measurements is shown in table 3 .

The rejection of pions was calculated by using the PI triggered sample after cleaning it up by TOF and dE/dx. In fig. 16 the probability of misidentifying a pion as an electron versus P_T is depicted. Below a P_T of 300 MeV/c the NaI detector gives hardly any rejection (except at very low P_T where the pions have lost so much energy before they reach the NaI crystals that they do not survive the cut). Above 300 MeV/c in P_T, where the pions are minimum ionizing, the pion rejection factor is constant and roughly 5. This rejection was worse than what was expected from a test beam experiment [65]. This disagreement is not well understood but it could partly be due to the fact that the crystals in this experiment did not point towards the interaction region. Another problem at the ISR was the background of photons, which could produce showers, which were mistakingly attributed to trigger tracks. Whatever the reason, the fact remains that the rejection of hadrons at low P_T by using the NaI detector was not very high.

4.3 PARTICLE IDENTIFICATION USING THE CHERENKOV DETECTOR

On – line the trigger requirement on the four Cherenkov signals was a minimum pulse height corresponding to 3 ADC counts for the MB trigger and 26 ADC counts for the PT and the ETOT trigger. Two requirements were made off – line on the Cherenkov signals. The first requirement was that the sum of the pulse heights, from the two PMs in the same Cherenkov, should be larger than 40 ADC counts, which corresponded to about two photoelectrons. The reason the pulse heights from the two PMs were added was that a particle passing through one of the detectors could produce Cherenkov light that was seen by both PMs (see fig. 5). The second requirement was that the signals should arrive within a 5 ns time window with respect to the event time. This time cut was made to prevent particles, originating from another event than that of interest, to trigger the Cherenkov.

In the calculation of the efficiency for these cuts, an event sample was used which had been submitted to very stringent electron identification cuts on TOF, dE/dx and the energy deposited in the NaI detector. In addition, it was required that the triggering particle made a low – mass combination with a second track of an opposite sign. In this way a sample of clean electrons recorded with the MB trigger (which had the lowest trigger threshold) was selected, without using the Cherenkov information. The pulse height distribution for this sample is plotted in fig. 17 , both for the individual PM tubes and for the sum of both tubes. From these distributions the efficiency of both the on – line and off – line pulse height cut was estimated and the results of these calculations are given in table 4 . A significant difference in efficiency for electrons and positrons was measured as a result of the different incident angles for positive and negative particles. It is important to note that the magnetic field was in the opposite direction when the PT data was recorded compared to when the MB and ETOT data were taken, and this can be seen in the results.

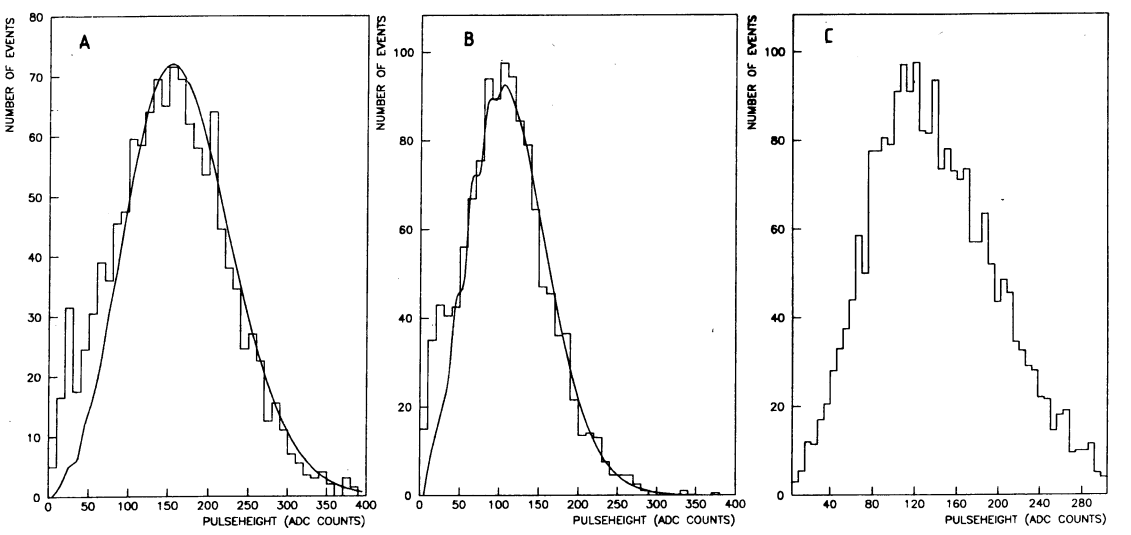

Figure 17: Pulse height spectrum for the Cherenkov detector. The curves in A) and B) are from a fit to a function described in the text.
A) Cherenkov 1, PM A.
B) Cherenkov 1, PM B.
C) Cherenkov 1, sum of PM A & B.

The Cherenkov pulse height spectrum can be described as a sum of Poisson distributions multiplied by Gaussian distributions:

$$dN(x) = N_t \cdot \sum_{n=1}^{\infty} \frac{U^n \cdot e^{-U}}{n!} \cdot \frac{e^{-\left(\frac{n \cdot m - x}{\sigma \cdot \sqrt{n}}\right)^2 / 2}}{\sqrt{2} \cdot \sqrt{\pi} \cdot \sigma \cdot \sqrt{n}} \, dx \quad \text{where}$$

x	the pulse height;
dN(x)	the number of events with pulse height between x and x + dx;
N_t	the total number of events;
U	the mean number of photoelectrons;
m	the pulse height of the first photoelectron peak;
σ	the width of the first photoelectron peak.

This formula was fitted to the measured pulse height distributions for each PM tube (see fig. 17). The fit made it possible to estimate the mean number of photoelectrons that were produced in the four PMs. The results of these fits are given in table 5 .

Table 4: The efficiency of the Cherenkov pulse height requirement.

Detector	Particle	MB	ETOT	PT
Cherenkov 1	e^+	97%	96%	88%
Cherenkov 1	e^-	90%	88%	96%
Cherenkov 2	e^+	87%	86%	91%
Cherenkov 2	e^-	92%	91%	86%

Table 5: The mean number of photoelectrons.

PM	σ	m	U
Cherenkov 1 A	6	22	8
Cherenkov 1 B	5	21	6
Cherenkov 2 A	5	21	6
Cherenkov 2 B	5	21	5

σ The width of the first photoelectron peak (rms) in ADC counts.
m The mean of the first photoelectron peak in ADC counts.
U The mean number of photoelectrons.

The efficiency of the timing requirement was calculated in a similar way as for the pulse height cut. The same clean electron sample was used and the time distribution (Cherenkov time – T0) was plotted (fig. 18). It was required that the Cherenkov signal had a measured time between 16 and 21 ns. The efficiency of this cut could be calculated directly from the time distribution (see table 6).

Since the Cherenkov detector was used in the trigger it was a bit more complicated to calculate its rejection than for the NaI detector or the TOF. The momentum threshold, however, was easy to calculate with the following expression [69]:

$$P_t = m/\sqrt{(2\cdot\delta + \delta^2)} \qquad \text{where}$$

P_t the momentum threshold for Cherenkov light;
δ $n-1$ ($410 \cdot 10^{-6}$ for CO_2);
n the refractive index;
m the mass of the particle which produces Cherenkov light.

A calculation of the P_t for different particles is given in table 7 . A pion with a momentum below P_t could fire the Cherenkov mainly by knock–on electrons or chance overlap and to a lower extent by scintillations in the gas or through electronic noise (see fig. 19).

Table 6: The efficiency of the Cherenkov time requirement.

Detector	**particle**	**MB**	**ETOT**	**PT**
Cherenkov 1	e^+	93%	97%	92%
Cherenkov 1	e^-	92%	95%	93%
Cherenkov 2	e^+	94%	96%	93%
Cherenkov 2	e^-	92%	96%	91%

Table 7: The momentum threshold (P_t) for producing Cherenkov light in CO_2 at atmospheric pressure.

Particle	**P_t (GeV/c)**
e	0.018
μ	3.7
π	4.9
K	17.2
p	32.8

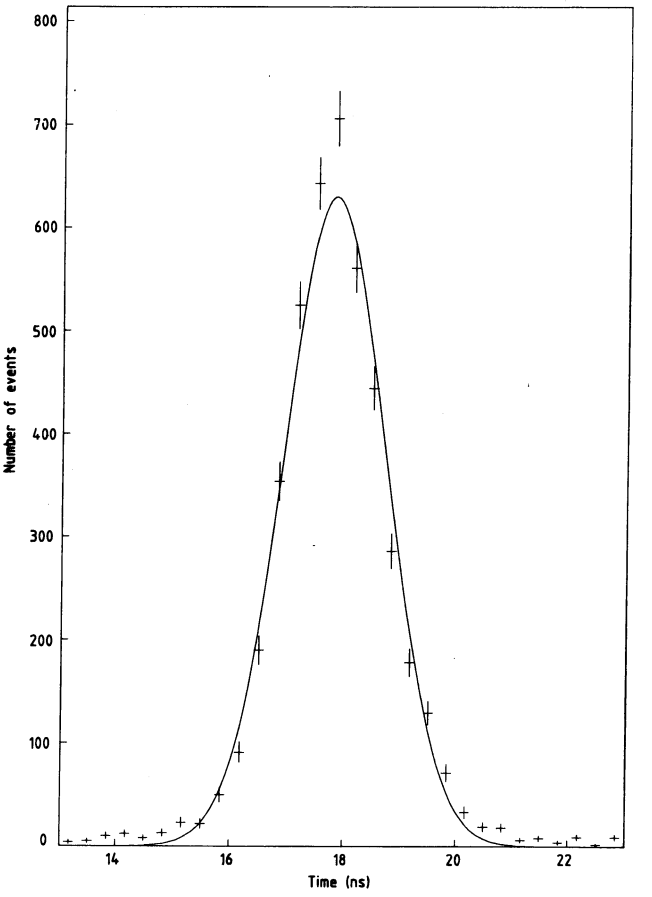

Figure 18: Time distribution for signals from the Cherenkov. A Gaussian distribution has been fitted to the measured distribution as a comparison.

The principle of the method, that was used to calculate the rejection, was that the amount of pions which survived the two Cherenkov cuts (on pulse height and time) was measured using dE/dx, and compared to the total amount of pions produced, which was measured with the pion trigger. The following formula (which is derived in appendix A) was used in the calculation of the rejection:

$$R = \left(B - \frac{A - \frac{B}{X}}{\frac{1}{Y} - \frac{1}{X}} \right) / P \qquad \text{where}$$

R the probability that a pion survive the Cherenkov cuts;

A the number of Cherenkov triggered events before the dE/dx cut;
B the number of Cherenkov triggered events after the dE/dx cut;
X the probability that a pion survives the dE/dx cut;
Y the probability that an electron survives the dE/dx cut;
P the number of PI triggered events after the dE/dx cut.

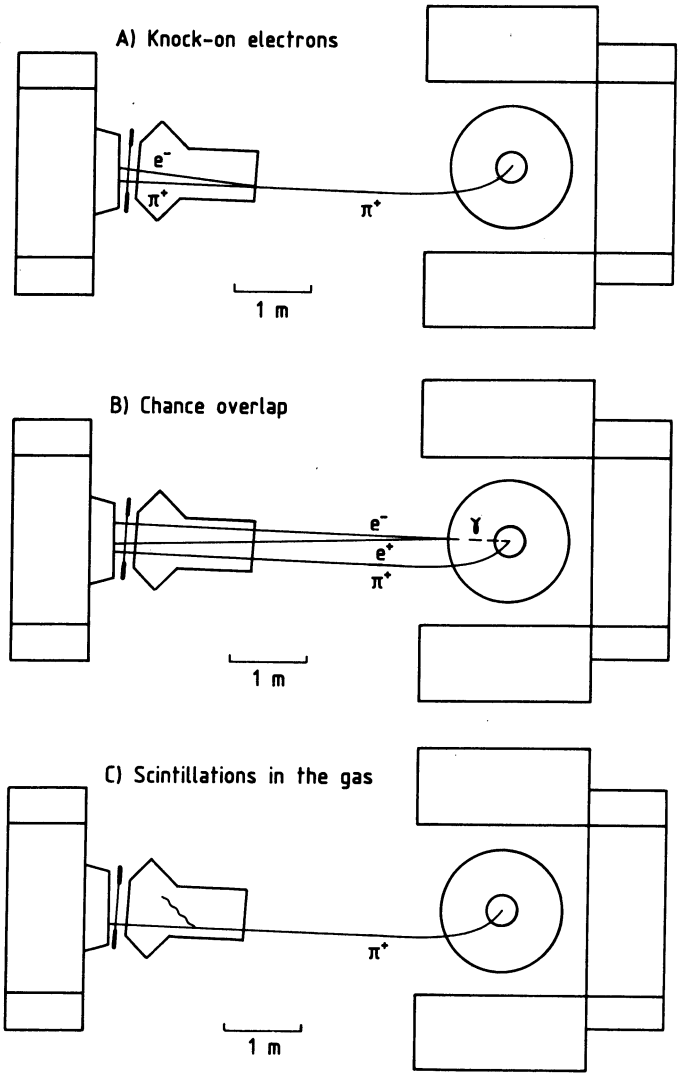

Figure 19: Different ways that background could fire the Cherenkov.

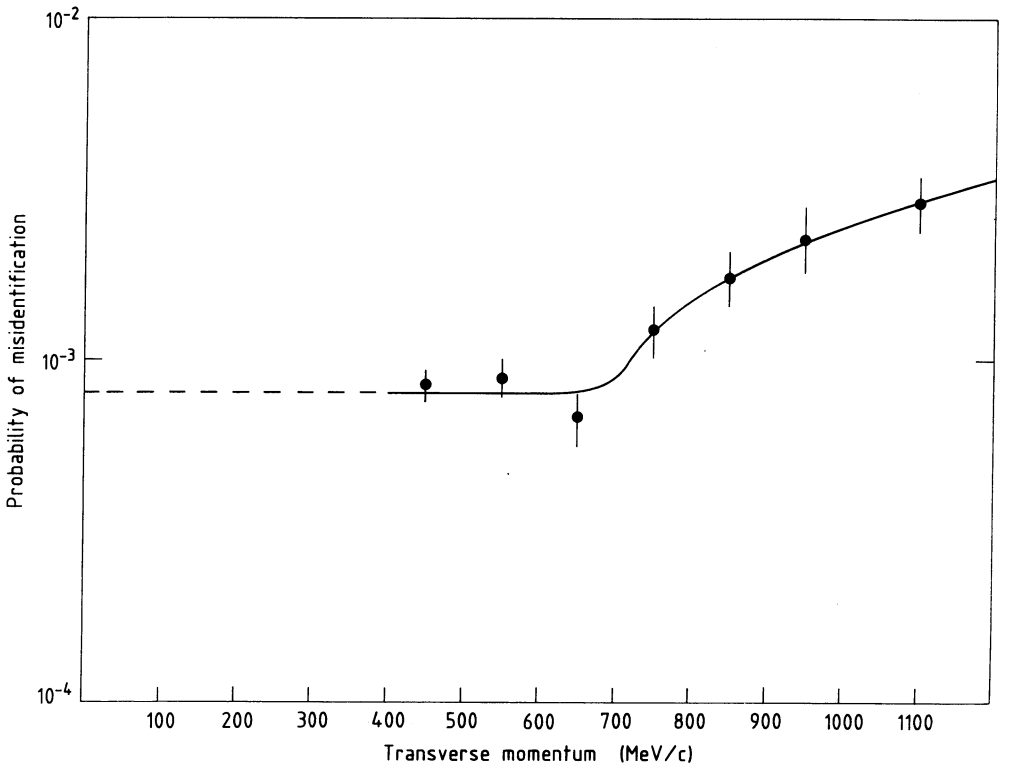

Figure 20: The pion rejection obtained with the Cherenkov detector.

In the calculation of the rejection a P_T cut of $P_T > 400$ MeV/c was made so that the Cherenkov time cut would not work as a TOF measurement and so that the identification of pions through dE/dx would be possible. A dE/dx cut was then constructed, which made it possible to identify pions with 85% efficiency (Y). The probability that an electron would be misidentified as a pion (X), by using this cut, was 0.011. At $P_T < 400$ MeV/c the Cherenkov counters have probably a better pion rejection than at high P_T since knock–on electrons (with $P > 18$ MeV/c) cannot be produced by pions with $P_T < 650$ MeV/c and the probability for chance overlap (fig. 19 b) is independent of the momentum of the triggering particles. However, it has been assumed in this analysis that the pion rejection of the Cherenkov detectors is the same for 80–400 MeV/c as in the measured region of $P_T > 400$ MeV/c which ought to be a safe assumption.

Using the MB data a rejection, integrated over P_T, of $R = (1.13 \pm 0.05) \cdot 10^{-3}$ was obtained. For the PT triggered data, where the NaI was also in the trigger, a

combined rejection of the Cherenkov and the NaI was measured to be $2.31 \cdot 10^{-4}$. By using the earlier calculated rejection for the NaI detector, the rejection factor obtained by the Cherenkov itself was estimated to be $(1.10 \pm 0.06) \cdot 10^{-3}$. Since the values of R for the two trigger samples are in perfect agreement, this is an independent test of the calculations of the NaI rejection at high P_T. Fig. 20 shows the result of a measurement of the rejection factor versus P_T. At a P_T larger than 700 MeV/c it seems as if the Cherenkov detectors ability to reject pions is decreasing (i.e. the rejection factor is increasing).

A crude calculation of the knock–on probability per pion was done to see if it could explain the rise at high P_T (see fig. 21). The following formulas [69] were used to calculate the production of knock–on electrons per unit path length:

$$\frac{dN}{dx} = D \cdot \frac{Z \cdot \rho}{A} \cdot \left(\left(\frac{1}{T_t} - \frac{1}{T_m} \right) / \beta^2 + (\ln(T_t) - \ln(T_m)) / T_m \right)$$

where

$$T_m = \frac{2 \cdot m \cdot \beta^2 \cdot \gamma^2}{1 + 2 \cdot \gamma \cdot \frac{m}{M} + \left(\frac{m}{M}\right)^2}$$

D	constant (0.1535 MeVcm^2/g);
Z	the atomic number of the medium;
A	the mass number of the medium;
ρ	the mass density of the medium;
T_t	the threshold kinetic energy of the Cherenkov (17 MeV);
T_m	the maximum kinetic energy of the knock–on electron;
β	the v/c ratio of the projectile particle;
γ	$(1-\beta^2)^{-1/2}$;
m	the electron mass;
M	the mass of the projectile particle.

In this calculation, only a crude estimate of the amount of material was made and no tracking of the particles was performed. This means that the systematic error on the absolute value could be as large as a factor of 2. On the other hand, the shape of the curve should be correct which means that a sharp cut–off can be expected at a pion momentum of 650 MeV/c. This cut–off is due to the minimum momentum (18 MeV/c) required by the electron in order for it to be able to trigger the Cherenkov detector. From this it can be concluded that the rise in the probability of misidentification at high P_T is most likely due to knock–on electrons produced by pions. Particles heavier than pions, such as kaons and protons, have an even higher cut–off and can therefore not trigger the Cherenkov when they are within the P_T range of this experiment.

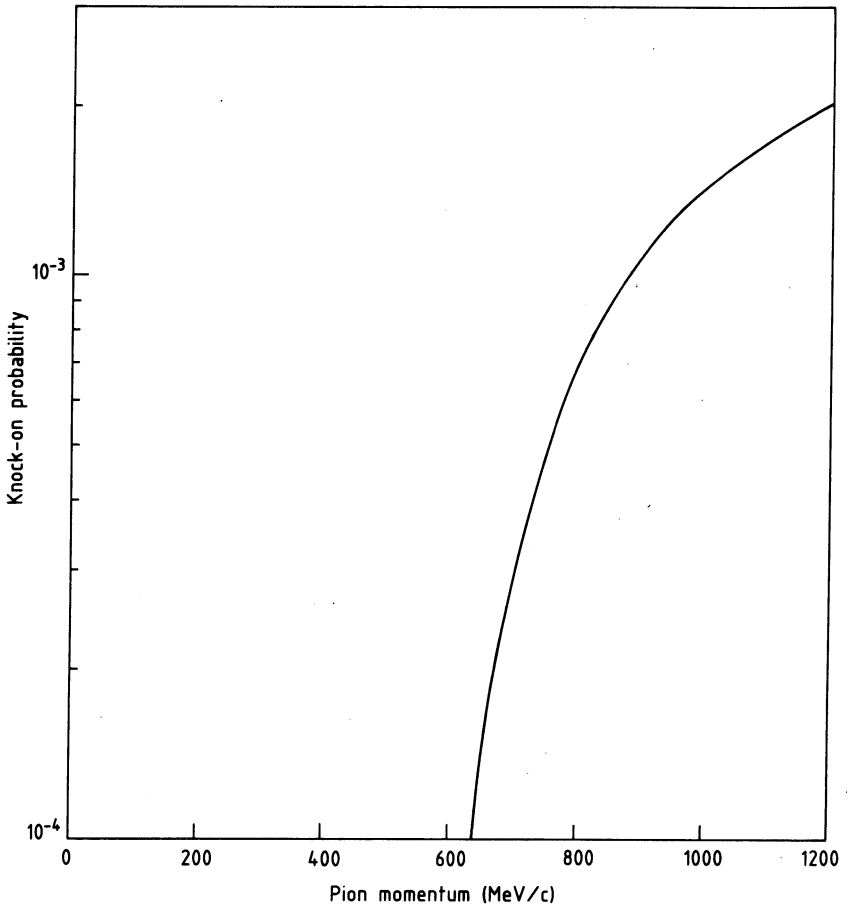

Figure 21: The knock – on probability per pion.

4.4 THE TIME – OF – FLIGHT MEASUREMENT

The event time (T0) was calculated off – line by using only the information from the BB counters since they had a better time resolution than the IH counters. For most events (81%) the event time was defined as

$$T0 = (<TBB_1> + <TBB_2>)/2$$

where $<TBB_1>$ and $<TBB_2>$ were the mean time of the signals from BB wall 1 and 2. Before calculating the mean value the signals were corrected for time shifts due to differences in pulse height (so – called slewing correction). If only one wall had registered hits (but there were at least two hits in the wall) the T0 was calculated in the following way:

$$T0 = <TBB_i> + \delta$$

where δ was the time required by a particle to travel between the vertex and the beam – beam counters. The requirement that the BB walls had been hit by particles reduced the two samples of MB and PI triggered events by 10%.

Both the signals from the BB counters and the IH counters were used in an algorithm which removed so – called double events, that is events where two pp collisions occurred so close in time that the signals from both collisions were recorded as if they belonged to one event.

The Time – Of – Flight (TOF) was defined as

$$TOF = (T_1 + T_2)/2 - T0$$

where T_1 and T_2 were the two times measured at both ends of the scintillation counters and T0 was the event time. A slewing correction of the form

$$T_i = t_i - A/PH_i$$

was performed, where PH_i was the pulse height of photomultiplier number i, and t_i the time measured for the corresponding photomultiplier. The constant A (=110) was obtained by minimizing the width of the $T_i - T0$ distribution. The time distributions, with and without slewing correction, are plotted in fig. 22 for a sample of electrons.

The flight paths of the particles were calculated by extrapolation assuming a magnetic field of 0.1 Tesla with a 100 cm radius. From the TOF and the flight path it was possible to calculate β (=v/c) of the triggering particle. A cut of $\beta > 0.92$ was imposed on the electron triggers. This cut had an efficiency which is described in table 8 . The efficiency was calculated using the clean sample of low – mass electron pairs shown in fig. 23 .

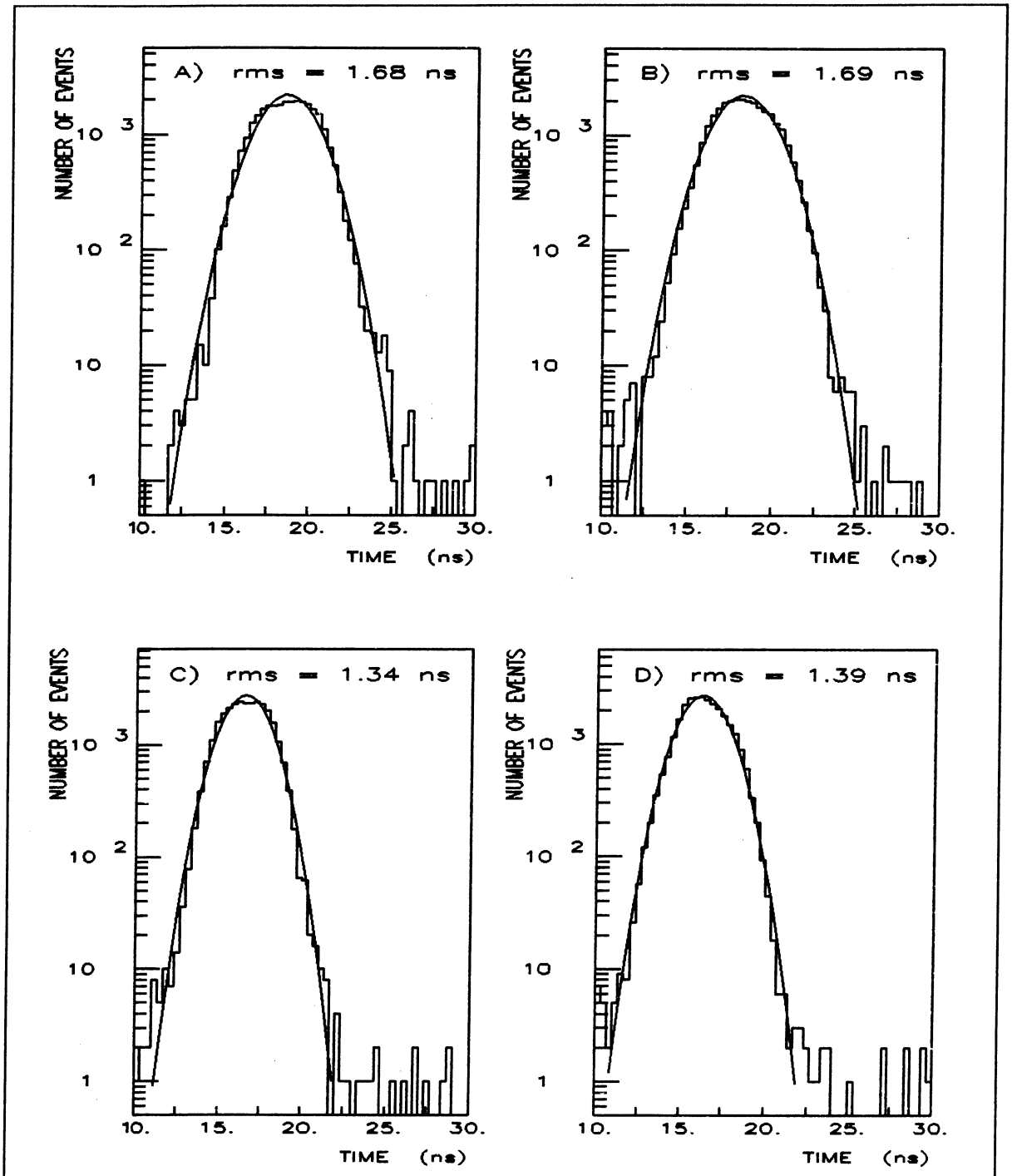

Figure 22: Time distributions for signals from the scintillators.
A) $t_1 - T0$ B) $t_2 - T0$ C) $T_1 - T0$ D) $T_2 - T0$
where t_i is the time measured by PM tube number i before slewing correction and T_i is the same time after slewing correction. The curves show Gaussian distributions.

Table 8: The efficiency of the TOF requirement.

Trigger	Efficiency
MB – 1	99%
MB – 2	98%
PT – 1	99%
PT – 2	99%
ETOT – 1	99%
ETOT – 2	99%

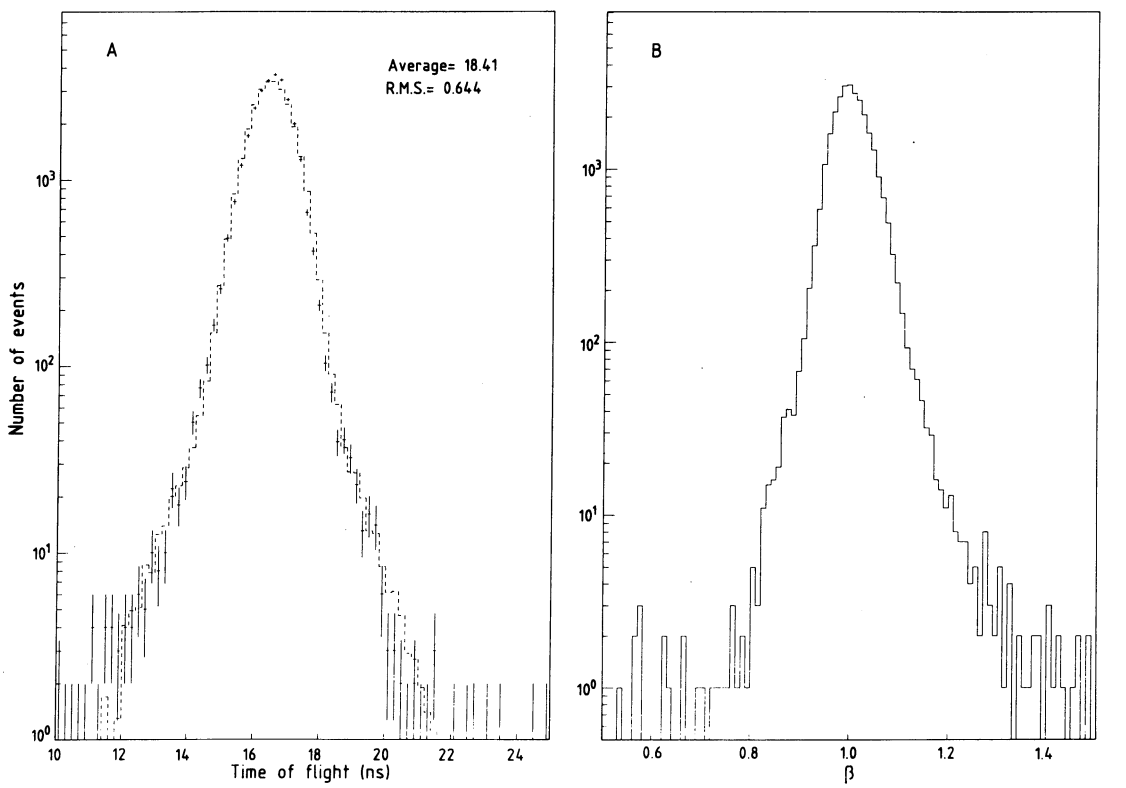

Figure 23: The distributions of A) TOF and B) β for electrons. The dashed line in A) indicates the result of the MC calculation.

The rejection of hadrons obtained by the TOF cut could be directly calculated for pions by using the PI triggered data. However, since it was impossible to extract a clean sample of kaons and protons, the rejection for these particle types could not be calculated using the data. For this reason a MC was written which tracked the particles through the magnetic field and decayed the correct fraction of pions into e,μ,ν and of kaons into π,e,ν. Only the shape of the TOF distribution for electrons (see fig. 23 a) was used as an input to this MC. The momentum dependence of the hadron bands in the MC was in good agreement with data as can be seen in fig. 24 .

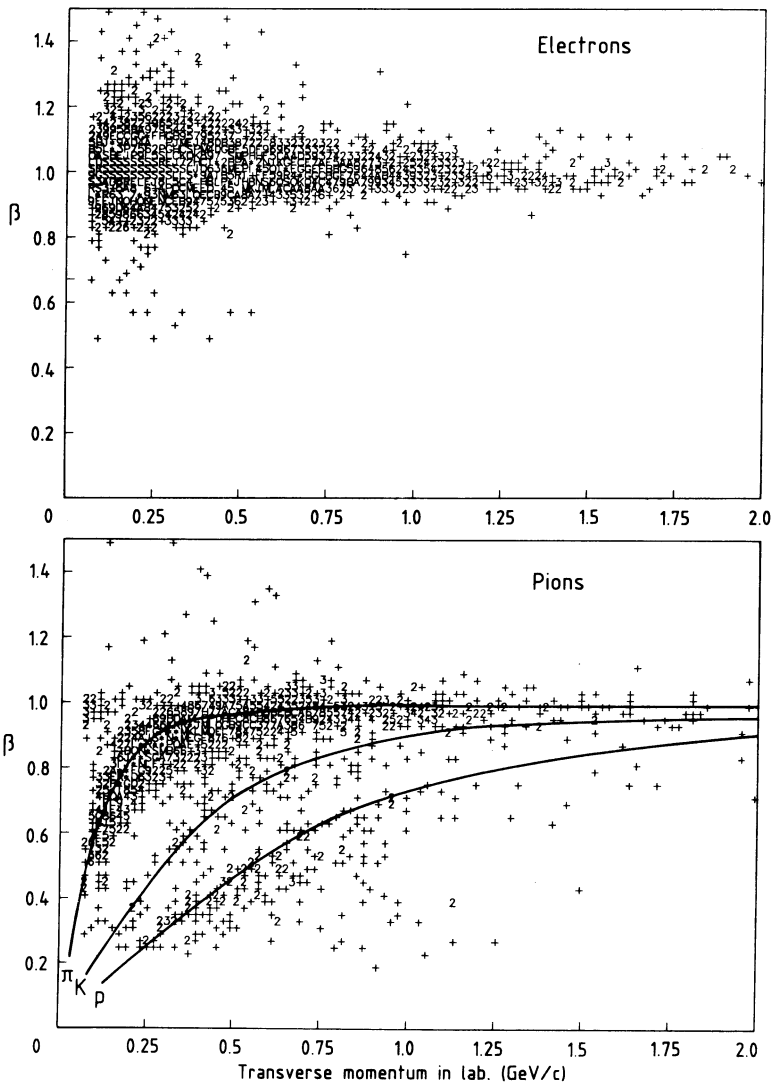

Figure 24: β plotted versus transverse momentum for electron and pion triggers. The curves show the mean value of β versus P_T according to MC calculations.

The hadron rejection which was calculated with the MC is presented in fig. 25 . If the PI triggered data was used instead of the MC, a similar rejection of pions was estimated.

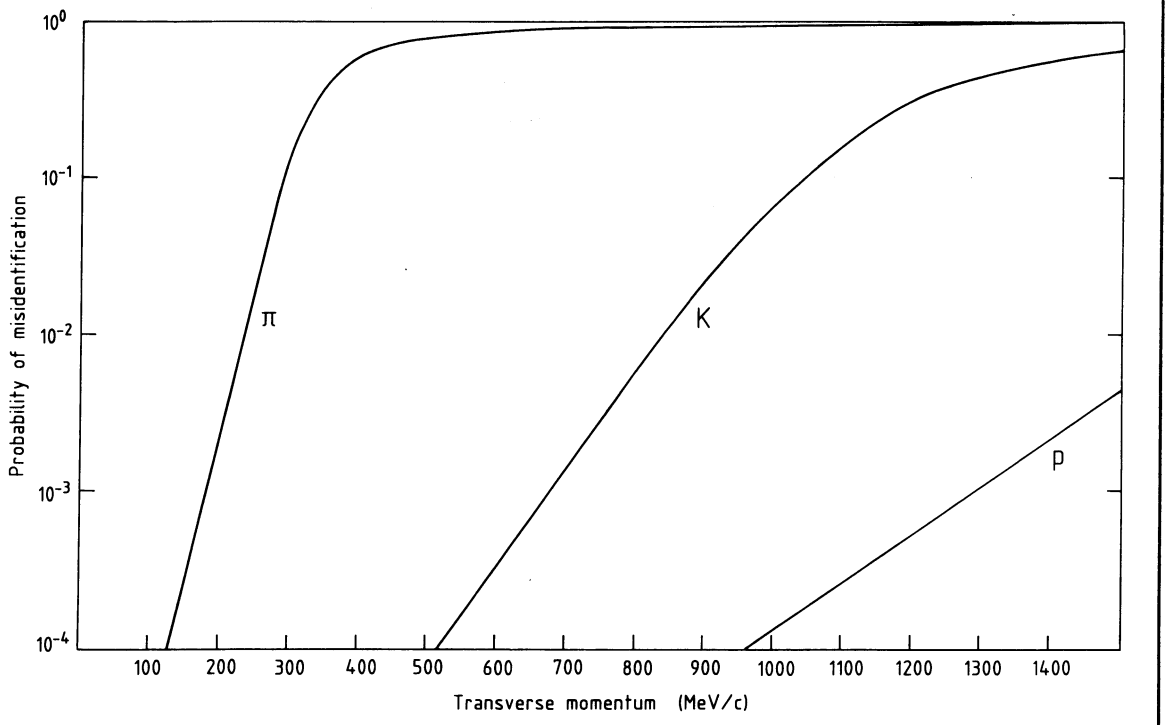

Figure 25: The hadron rejection obtained with the TOF cut.

4.5 SUMMARY OF HADRON REJECTION AND CUT EFFICIENCIES

Fig. 26 shows the probability of misidentifying a hadron as an electron combining all four methods of electron identification. Below a P_T of 200 MeV/c the TOF and the dE/dx gave a very good rejection of pions. In the P_T range of 200 – 800 MeV/c the pion contamination was in the order of $\sim 10^{-5}$ and the kaon contamination was negligible. Above 800 MeV/c the contamination of pions was rising rapidly due to knock – on electrons which fired the Cherenkov and in addition because of the decreasing rejection from dE/dx. Also the kaon contamination increased rapidly at high P_T since the rejection from TOF and dE/dx decreased at high P_T. The shaded band shows the uncertainties in the rejection of kaons with the Cherenkov.

The upper limit was calculated by assuming the same Cherenkov rejections for pions and kaons and the lower limit by assuming a constant Cherenkov rejection at the level of $\sim 8 \cdot 10^{-4}$ for kaons. The proton contamination was negligible in the P_T interval of this experiment due to the effective rejection of protons by dE/dx and TOF. Since the hadron contamination was rising rapidly at high P_T the e/π ratio was not measured above a P_T of 1 GeV/c.

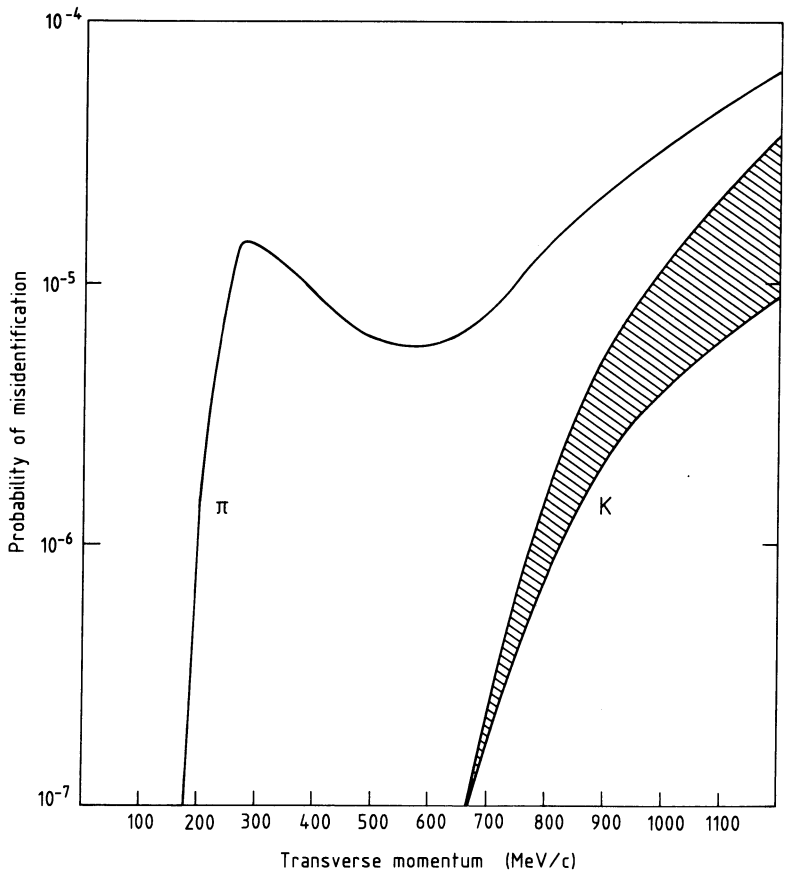

Figure 26: The hadron rejection combining all methods.

The cuts that were applied in order to reject hadrons off–line were constructed so that they would have a constant cut efficiency for electrons. The overall cut efficiency was ~75% but it was slightly different for electrons and positrons (mainly due to the Cherenkov efficiency) and for triggers in Cherenkov 1 and Cherenkov 2,

as can be seen in table 9 . There were also differences between the different triggers since they were recorded during different ISR runs and the conditions were not exactly the same e.g. the polarity of the magnetic field.

Table 9: Combined efficiency of the various pion rejection cuts.

Detector	**particle**	**MB**	**ETOT**	**PT**
Cherenkov 1	e^+	75%	76%	74%
Cherenkov 1	e^-	68%	69%	81%
Cherenkov 2	e^+	68%	67%	75%
Cherenkov 2	e^-	71%	70%	70%

5. REJECTION OF TRIVIAL ELECTRON SOURCES

The background sources can be divided into two main categories: single electron sources and pair sources. Among the single sources are weak decay of kaons and D mesons and electrons from Compton scattering. The pairs are either coming from converting real photons or from virtual photons. Since the real photons create pairs with a zero mass, contrary to the virtual photons, the second electron in the conversion pairs was likely to be found close to the trigger track. This made it relatively easy to reject conversions provided the second electron in the pair reached the drift chamber.

In addition to the division into single and pair sources, the background was divided up into "trivial" and "interesting" background sources. A background source was called trivial if it was possible to calculate, with high accuracy, the contribution from the source to the measured e/π ratio. The contribution from interesting sources was more difficult to calculate with Monte Carlo simulations (e.g. because of uncertainties in cross sections or branching ratios). The division into trivial and interesting sources was to some extend arbitrary but in order to be able to compare the results with previous experiments the two groups of background sources had to be the same as in other experiments. The reason for this was that trivial sources were eliminated from the data as much as possible and the fraction of events from these sources that survived the cuts were calculated by MC and later subtracted from the measured e/π. This was not the case for the interesting sources. In this way positrons from e.g. weak decay of K mesons are not included in the final e/π ratio while positrons from the weak decay of D mesons are.

Electrons originating from Compton scattering of photons are a special case. Although this was a trivial background source it was difficult to reject these electrons in the analysis and since the production of low $-P_T$ Compton electrons was copious in this experiment it was decided not to use the e^- triggers when the e/π ratio was calculated. However, the e^- triggers were used in the pair measurement where the Compton background was less of a problem and also in a test of the Monte Carlo simulation.

5.1 REJECTION OF LOW – MASS ELECTRON – POSITRON PAIRS

The "trivial" background of electron – positron pairs, originated either from the conversion of photons or from Dalitz decays of various mesons. If one of the members of the pair did not reach the drift chamber because its momentum was so low it curled – up (due to the magnetic field) before entering it, the pair could obviously not be rejected. The fraction of events from different background sources where this occurred could be calculated easily and reliably since it was only a geometrical problem which did not depend on any detector response.

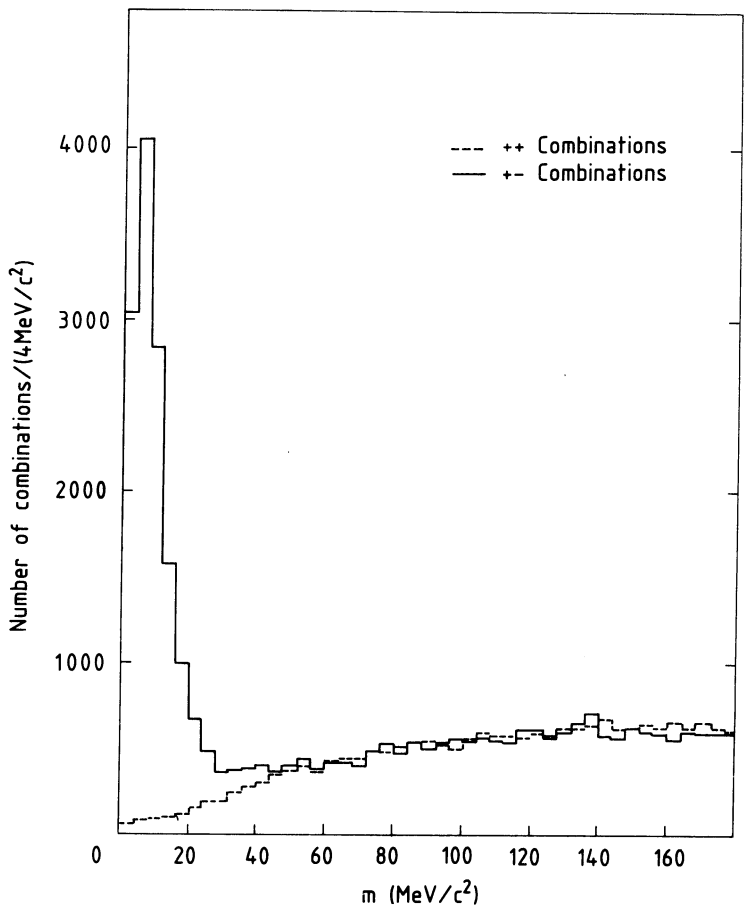

Figure 27: Mass distributions of e^+x^- and e^+x^+ pairs (where e is the trigger track and x is any other track in the DC).

When the low momentum electron reached the drift chamber, the situation was more complicated. Three situations could occur as follows:

- A) The second track was found and reconstructed by the track–finding and track–fitting programs.
- B) The second track was not reconstructed because it had too low momentum (< 10 MeV/c) and hence a radius and length that was too small.
- C) The second track was not found because it had a fairly high P_T and it was so close to another track (in most cases the trigger track) that the track finding programs made one track out of the two.

Different methods of rejecting all three types of background events were used and in order to be able to calculate the remaining background, a large Monte Carlo drift chamber simulation was made.

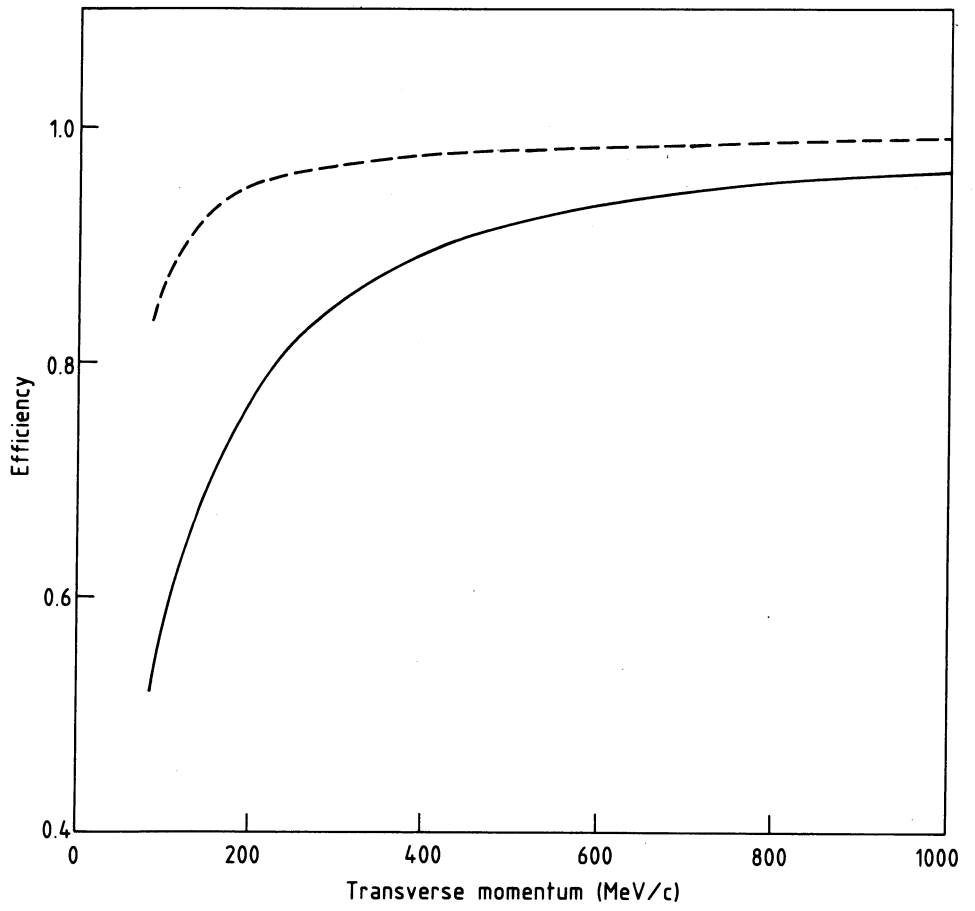

Figure 28: Efficiency corrections for the mass cut.
The dashed line shows the efficiency for a cut at 50 MeV/c^2 and the full line the efficiency for a cut at 100 MeV/c^2.

5.1.1 RECONSTRUCTED PAIRS

The main way of rejecting positrons coming from converted photons or Dalitz decays was by a cut on the invariant mass calculated by combining the trigger track with all other tracks of negative charge. In this calculation it was assumed that the

second track was an electron. There was no quality requirement made on the second track in order to obtain the highest possible track finding efficiency (and thus the highest possible pair finding efficiency). In fig. 27 the invariant mass for like–sign and unlike–sign combinations is depicted and a clear peak at zero mass is seen due to pairs from γ conversions and Dalitz decays.

The cut was done at a 100 MeV/c^2 so that a major part of all pairs from Dalitz decays of π^0's would be cut away. Another reason for doing the cut at a 100 MeV/c^2 and not at e.g. 50 MeV/c^2 was that previous experiments had made cuts on either mass or angle which corresponded to this value. In order to be able to compare the AFS results with those of previous experiments it was therefore preferable to do the same mass cut. Since the source of interest might very well be a pair source, it is important to note that in this experiment, as well as in others, the measured e/π ratio does not include contributions from pairs with a mass less than 100 MeV/c^2.

Since there was no quality requirement or identification made on the second electron (i.e. the electron that did not trigger) in the pair, the probability of finding this electron was high if it reached the drift chamber. The negative aspect of this loose requirement on the second electron was that a larger efficiency correction (see fig. 28) had to be made because of the possibility of two uncorrelated tracks giving a mass combination less than 100 MeV/c^2.

This cut efficiency was calculated by using the pion sample. Since there were no pion triggers with a P_T less than 120 MeV/c the cut efficiency, at these low P_T values, was calculated by changing the momentum vector of pion triggers with a higher P_T and then combine these "new" trigger tracks with the other tracks in the event. When the momentum vector of the trigger track was changed the direction of the vector was kept intact but the absolute value was decreased. The efficiency calculated with pions with original momentum vectors and modified vectors was in good agreement at $P_T > 120$ MeV/c but the systematic uncertainty of this method below a P_T of 120 MeV/c was still assumed to be large.

5.1.2 UNRECONSTRUCTED ASYMMETRIC PAIRS

Events of type B could effectively be rejected by a cut on the digitizings in the drift chamber which had not been assigned to any track by the track fitting programs. Fig. 29 displays a typical event where a second low–P_T electron has not been found by the track fitting program. The track can still be detected, by counting the number of unassigned digitizings in a volume around the trigger track.

Eventually three different cuts on the number of unassigned digitizings were used. Two of the cuts were aimed at the type B events and one cut at the type C events. In the main requirement, the number of unassigned digitizings was counted within a sector of $\pm$12cm in ΔZ and $-8^0 < \Delta\phi < 80^0$ (with respect to the trigger

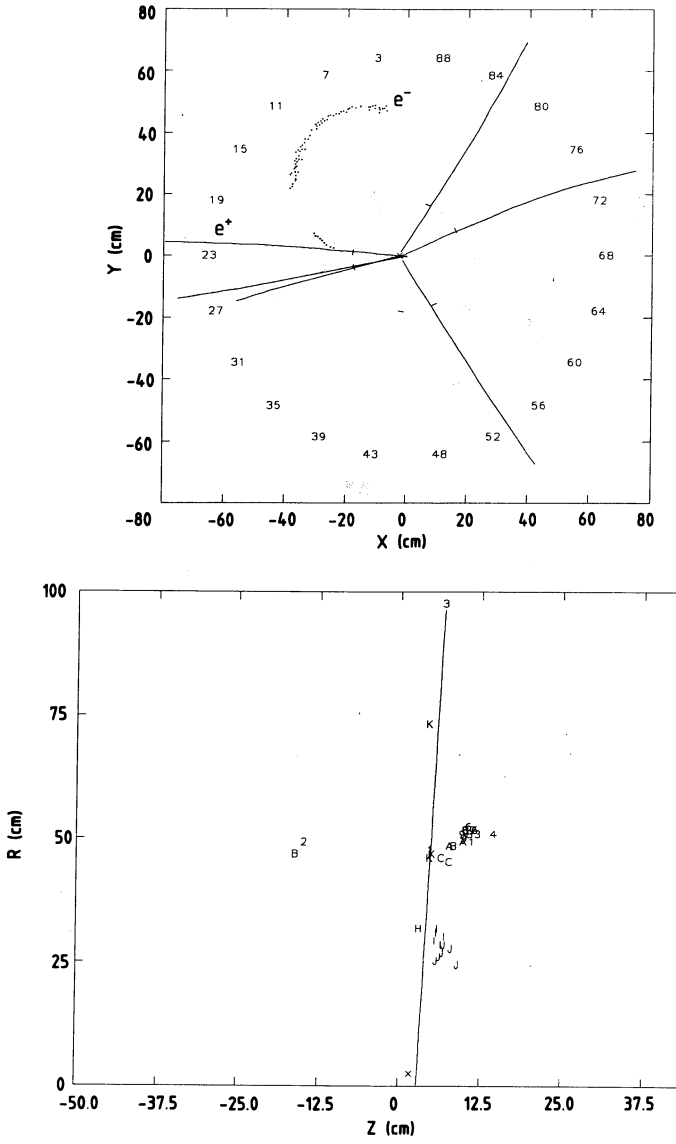

Figure 29: Event with an unreconstructed pair in the DC.
A) View of the event in the transverse plane. The reconstructed tracks are shown as lines and the unassigned digitizings as dots.
B) View of the event in the ZR plane. Only the trigger track and the unassigned digitizings are shown.

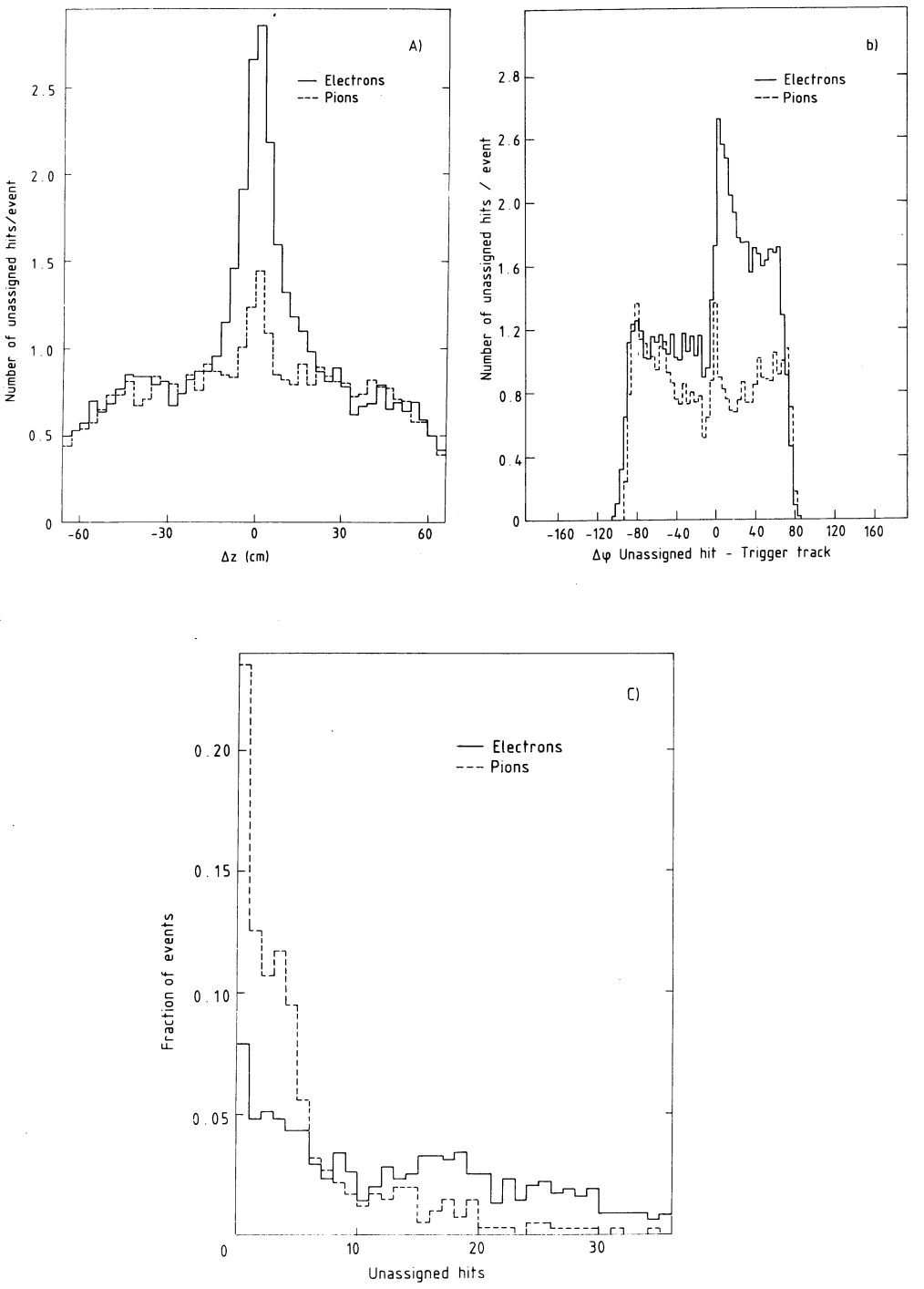

Figure 30: Distributions of unassigned digitizings.
A) The number of un. dig. as a function of ΔZ.
B) The number of un. dig. as a function of $\Delta\phi$. Only half of the DC has been used in this plot.
C) The total number of un. dig. within ± 12cm in ΔZ and $-8^0 < \Delta\phi < 80^0$

track). The distributions of these quantities are shown in fig. 30 a and b. In fig. 30 c the distribution of the total number of unassigned digitizings in the region of space described above is shown. The higher mean number of unassigned digitizings for the electron trigger compared with the pion trigger is due to the unreconstructed low–mass pairs.

In the ΔZ distribution, a clear enhancement of the number of digitizings, due to pairs, is seen around the trigger track ($\Delta Z = 0$). However, the pion trigger also has a peak around $\Delta Z = 0$, although it is considerably smaller. This is due to digitizings belonging to the trigger track, which were not used by the track–fitting program. In the $\Delta\phi$ distribution it is clear, by comparing the pion and electron triggered sample, that there is an additional amount of digitizings from an unresolved second track since the difference between the distributions is only on one side of the trigger track ($\Delta\phi > 0$).

The second cut on the unassigned digitizings was aimed at removing events with a second electron, with a momentum of only a few MeV/c, which had curled–up in the very beginning of the drift chamber. The region in space used for this cut was $R < 35$ cm and either $-5 < \Delta Z < 30$ cm or $-30 < \Delta Z < 5$ cm depending on which Z region had the most unassigned digitizings.

The final sample of events was scanned visually and less than 2% of the events had any digitizings which could belong to a second track. This scan confirmed that the final event sample hardly contained any asymmetric pairs where the second electron had reached the drift chamber.

5.1.3 UNRECONSTRUCTED SYMMETRIC PAIRS

Pairs of type C, where the second electron had a high momentum and was so close to the trigger that it was not reconstructed, could be rejected by three methods:

- the unassigned digitizings;
- the dE/dx of the trigger track;
- the number of measurements of the Z position along the trigger track.

The algorithm for unassigned digitizings, which was used to remove the type C events, counted the number of unassigned digitizings in the same drift chamber sector as the trigger track. No requirement was made on the Z position of the unassigned digitizings, since if two tracks had passed through the same DC sector, the Z measurements (obtained by charge division) would be unreliable.

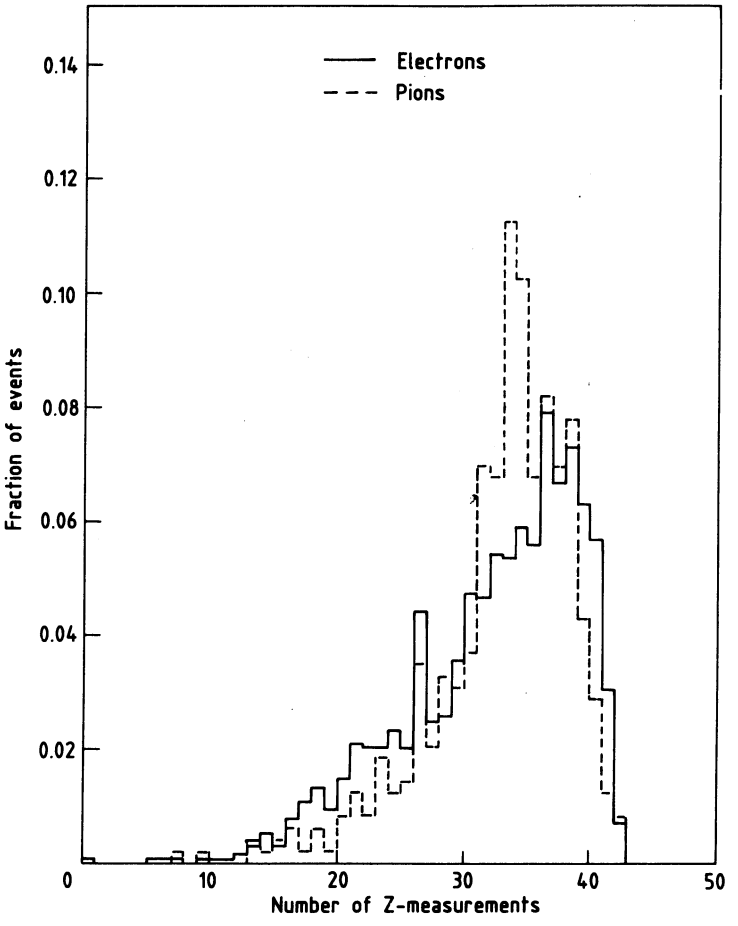

Figure 31: Distributions of the number of Z measurements.

The second method which was used to remove the close pairs, was a measurement of the number of Z measurements that had been used in the track–fitting procedure. As already mentioned, the Z position was measured by charge division and if two tracks passed through the same sector, the charge from both tracks would be collected on the same sense wires. When this happened the measurement would be disregarded by the track–fitting program. The total number of Z measurements would therefore be larger for a single track than for close unresolved pairs. The distributions of the number of Z measurements are depicted in fig. 31 for pion and electron trigger tracks. A requirement was made of at least 25 Z measurements and it can be seen from figure 31 that this cut removed more electron than pion triggers (because of the unreconstructed close pairs in the electron sample).

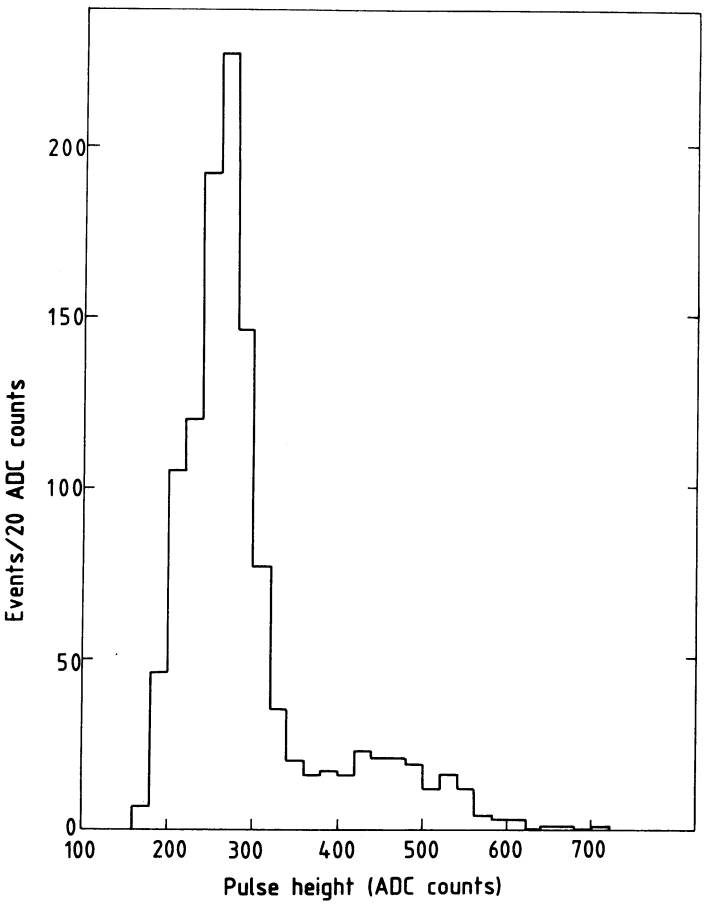

Figure 32: A dE/dx distribution for electron triggers. The doubly ionizing pairs are clearly seen as a second peak.

It has already been discussed in section 4.1, that if there was more than one track in the same sector, the charge from both tracks would be collected on the same sense wires, thus giving a pulse with larger pulse height than that of a single track. This effect made it possible to remove not only hadrons but also close unresolved pairs with the dE/dx cut. The distribution of dE/dx for a sample with a large fraction of close pairs is given in fig. 32 , a clear second peak from so called doubly ionizing pairs can be seen.

5.2 REJECTION OF BACKGROUND FROM SINGLE ELECTRON SOURCES

In this experiment the main way of rejecting trivial single electrons sources was by extrapolating the track back to the vertex. If the trigger track was further away from the primary vertex than 1.5 cm in the transverse plane and ± 12 cm in the Z direction the event was disregarded. Events with electrons from single sources where the electron pointed back towards the vertex were much more difficult to reject.

5.2.1 SINGLE ELECTRONS FROM WEAK DECAYS

The main background of positrons originating from weak decay of mesons comes from the following decay channels [69]:

- A) $K^+ \rightarrow e^+ + \pi^0 + \nu$ $c\tau$: 370.9 cm
- B) $K^0_L \rightarrow e^+ + \pi^- + \nu$ $c\tau$: 1554 cm
- C) $D^+ \rightarrow e^+ + X$ $c\tau$: 0.028 cm
- D) $D^0 \rightarrow e^+ + X$ $c\tau$: 0.013 cm

It has already been mentioned that decays of type A and B were called "trivial" while C and D were regarded as "interesting". For this reason attempts were made in the analysis to reject Ke_3 decays but not D meson decays. The rejection of positrons originating from kaons depended strongly on the decay point. If the decay occurred before the drift chamber, the positrons would be rejected mainly by the vertex requirement. The vertex distribution for electrons from Ke_3 decays will be discussed in more detail in section 6.4.1 (fig. 36). In addition to the vertex requirement, it was possible to reject type B events, to some extent, by the mass cut because of low – mass $\pi^- e^+$ combinations.

If the decay occurred inside the drift chamber the vertex requirement would remove an even larger fraction of the background and in addition the χ^2/NDF cut would remove events with a kink in the K – e trajectory. The type B decays would be rejected by the requirement that the trigger track had to start in the beginning of the drift chamber. All this combined meant that, of the Ke_3 events that survived the cuts, only a negligible fraction had decays that occurred in the drift chamber.

Finally, the kaon could decay between the drift chamber and the Cherenkov detector. All the type B events would be rejected by the requirement of a trigger track in the drift chamber which could be extrapolated to the scintillation counters. The same requirement rejected a large fraction of the type A events.

Positrons originating from charm decay (type C and D) could not be rejected by the vertex requirement since the decay length was too short. The mass cut would remove a small fraction of events triggered by the decay of D mesons because of $e^+ K^-$ combinations with a low mass. The double semileptonic decay of $D\bar{D}$ pairs can produce electron – positron pairs but the probability that these pairs have a low mass is small [14].

5.2.2 SINGLE ELECTRONS FROM COMPTON SCATTERING

The vertex requirement did not remove a substantial fraction of the electrons produced through Compton scattered photons since most of the produced electrons pointed in the same direction as the γ. The only other way to reduce the large Compton background in this experiment was to extrapolate the trigger track back to the inner hodoscope scintillator that the track had passed through. If there was no signal from the corresponding scintillator the γ must have scattered after the inner hodoscope, i.e. in the drift chamber wall. Figure 33 shows the pulse height distribution for the inner hodoscope scintillator that the trigger track was extrapolated back to. If the trigger track was a charged pion the fraction of events with no signal from the scintillator was 4%, i.e. the efficiency of a requirement of a signal from the inner hodoscope was 96%. If the trigger track was a positron, which had survived all pion and pair rejection cuts, the fraction of events with no signal was somewhat higher (6%) due to a small fraction of events in this sample that were triggered by γ conversions in the drift chamber wall.

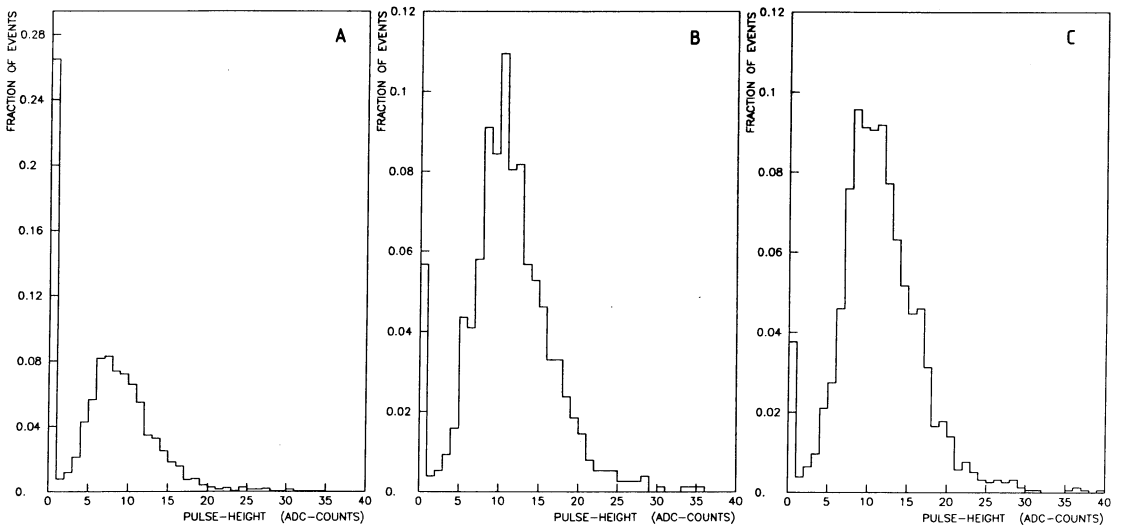

Figure 33: Pulse height distributions of signals from the IH counters for different particle types.
A) e^- B) e^+ C) π

A large difference can be seen if the pulse height distribution for electrons and positrons are compared. In the electron case, 27% of the events have no signal from the inner hodoscope scintillator that was traversed by the trigger track. This is due to Compton scattering in the drift chamber wall which corresponded to 25% of all material between the vertex and the drift chamber. Consequently, the pulse height requirement made it possible to remove some, but not all, of the large Compton background. Since the remaining background from this process was larger than all other background processes added together, it was decided not to use the electron sample in the single e/π measurement. In the pair measurement, however, the background from single electrons was not so troublesome and here the electron triggered sample was used after a requirement of a minimum pulse height in the inner hodoscope.

6. MONTE CARLO SIMULATIONS

The final event sample contained electrons from a large number of known sources. These sources could be grouped in the following way:

- **A. e^+e^- pairs from real photons:**

  a1. γ conversion of photons originating from the decay of mesons;
  a2. γ conversion of photons originating from hadronic bremsstrahlung.

- **B. e^+e^- pairs from virtual photons:**

  b1. Dalitz decays of π^0, η and η';
  b2. Hadronic bremsstrahlung;
  b3. The decay of ρ, ω, ϕ and J/ψ.

- **C. Single electrons and positrons:**

  c1. weak decay of kaons;
  c2. weak decay of D mesons;
  c3. Compton scattering.

The contribution from all these sources to the measured yield of single electrons was calculated by Monte Carlo simulation and a complete list of all decays considered is given in table 10[1] together with their branching ratio (B) [69], the number of parents per π^0 at y=0 integrated over P_T (X_π), the multiplicity of the decay product (M) and the rejection factor (R). The major contribution to the raw e/π (before any rejection cuts) comes from group a1, b1 and c1. It was described, in chapter 5, how the fraction of electrons coming from these sources was reduced by the different cuts in the analysis. The remaining positrons that originated from these sources were calculated by MC simulation and subtracted from the measured e/π. Other sources like b2, b3 and c2 were defined as "interesting" (see chapter 5) and the contribution from these sources was not subtracted from the e/π ratio. The background originating from Compton scattering of photons (group c3) was large but could easily be removed by using only the positron sample and simply disregarding the electron sample. However, the background from Compton scattering was calculated as a test of the MC.

[1] The decay processes shown in table 10 are somewhat incomplete, e.g. decays of type a and c3 also involve atoms.

Table 10: The processes generated in the Monte Carlo.

Decay	**type**	**B**	X_π	**M**	**R**
$\pi^0 \to \gamma + \gamma \to e^+e^- + \gamma$	a1.1	0.98802	1	2	54
$\eta \to \gamma + \gamma \to e^+e^- + \gamma$	a1.2	0.390	0.145	2	61
$\eta \to 3\pi^0 \to \gamma\gamma + 2\pi^0 \to e^+e^- + \gamma + 2\pi^0$	a1.3	0.314	0.145	6	31
$\omega \to \gamma + \pi^0 \to e^+e^- + \pi^0$	a1.4	0.087	0.110	1	88
$\omega \to \pi^0 + \gamma \to \gamma\gamma + \gamma \to e^+e^- + \gamma + \gamma$	a1.5	0.086	0.110	2	60
$\eta' \to \gamma + \gamma \to e^+e^- + \gamma$	a1.6	0.019	0.063	2	87
$\eta' \to \gamma + \rho \to e^+e^- + \rho$	a1.7	0.300	0.063	1	47
$\pi^+ \to \pi^+ + \gamma \to \pi^+ + e^+e^-$	a2.1	–	1	1	–
$\pi^0 \to \gamma^* + \gamma \to e^+e^- + \gamma$	b1.1	0.01198	1	1	12
$\eta \to \gamma^* + \gamma \to e^+e^- + \gamma$	b1.2	0.0050	0.145	1	4.6
$\eta \to 3\pi^0 \to \gamma^*\gamma + 2\pi^0 \to e^+e^- + \gamma + 2\pi^0$	b1.3	0.00381	0.145	3	7
$\omega \to \pi^0 + \gamma \to \gamma^*\gamma + \gamma \to e^+e^- + \gamma + \gamma$	b1.4	0.00104	0.110	1	16
$\omega \to \gamma^* + \pi^0 \to e^+e^- + \pi^0$	b1.5	$6.4 \cdot 10^{-4}$#	0.110	1	4.8
$\pi^+ \to \pi^+ + \gamma^* \to \pi^+ + e^+e^-$	b2.1	–	1	1	–
$\rho \to \gamma^* \to e^+e^-$	b3.1	$4.6 \cdot 10^{-5}$	0.109	1	–
$\omega \to \gamma^* \to e^+e^-$	b3.2	$6.7 \cdot 10^{-5}$	0.110	1	–
$\phi \to \gamma^* \to e^+e^-$	b3.3	$3.1 \cdot 10^{-4}$	0.060	1	–
$J/\psi \to \gamma^* \to e^+e^-$	b3.4	0.074	$7 \cdot 10^{-6}$	1	–
$K^+ \to e^+ + \pi^0 + \nu$	c1.1	0.0482	0.087	1	6.2
$K^0_L \to e^+ + \pi^- + \nu$	c1.2	0.387	0.080	0.5	7.0
$D \to e + K + \nu$	c2.1	0.04	0.0013	1	–
$D \to e + K^* + \nu$	c2.2	0.04	0.0013	1	–
$\pi^0 \to \gamma + \gamma \to e^- + \gamma' + \gamma$	c3.1	0.98802	1	2	1
$\eta^0 \to \gamma + \gamma \to e^- + \gamma' + \gamma$	c3.2	0.390	0.145	2	1
$\eta \to 3\pi^0 \to \gamma\gamma + 2\pi^0 \to e^- + \gamma' + \gamma + 2\pi^0$	c3.3	0.314	0.145	6	1
$\omega \to \gamma + \pi^0 \to e^- + \gamma' + \pi^0$	c3.4	0.087	0.110	1	1
$\omega \to \pi^0 + \gamma \to \gamma\gamma + \gamma \to e^- + \gamma' + \gamma + \gamma$	c3.5	0.086	0.110	2	1
$\eta' \to \gamma + \gamma \to e^- + \gamma' + \gamma$	c3.6	0.019	0.063	2	1
$\eta' \to \gamma + \rho \to e^- + \gamma' + \rho$	c3.7	0.300	0.063	1	1

no measurement exists ($B = 0.087 \cdot \alpha$ has been assumed).
γ^* denotes a virtual and γ' a scattered photon.

The first step in the MC calculations was the generation of the parent particles according to parameterizations described below. A certain CM phase space volume ($150^0 < \phi < 210^0, |y| = \pm 0.1$), which was somewhat larger than the triggering scintillation counters, was used to define a trigger in the MC. The fact that the "trigger" phase space volume was larger in the MC than in the data did not change the results but did increase the efficiency of the MC. The number of parent particles (N_X) going into the trigger phase space volume was counted for normalization purposes. All the parent particles were then decayed into the channel of interest.

After the parents had been decayed into positrons and electrons the generated MC event was read out to magnetic tape and used as input to the AFS full drift chamber MC. This MC simulated the ADC and DTR signals caused by the electrons. The output from this MC had the same format as a raw data tape and could be processed through the standard track–finding and track– and vertex–fitting programs. The final result of the MC chain was events that could be studied with the normal analysis programs. This MC did not simulate any other parts of the experiment than the drift chamber, but since all rejection of pairs was accomplished by this detector, this was not a limitation. However, the MC events did only contain the electron tracks and the additional particles that are present in a real event were not generated. The residual e/π ratio versus P_T was calculated, from the P_T spectrum of the electrons that had not been rejected, by the following formula:

$$\sigma(e)/\sigma(\pi) = (e/\pi) \cdot (X_\pi/N_X) \cdot B \cdot M \qquad \text{where}$$

$\sigma(e)/\sigma(\pi)$	the cross section of electrons divided with the cross section of pions;
e	P_T spectrum of electrons that were not rejected;
π	P_T spectrum of π^0's normalized to the integral of one;
X_π	the number of parents per π^0 at $y = 0$, integrated over P_T;
N_X	the number of parents going into the trigger phase space volume;
B	the branching ratio;
M	multiplicity of the final decay product.

The e/π ratio obtained after this normalization could be subtracted from the measured efficiency corrected e/π ratio. In the case of bremsstrahlung the normalization was somewhat different. For this process an absolute normalization was done, i.e. formulas were used with which it was possible to directly calculate the probability that a charged pion would radiate a bremsstrahlung photon.

In order to save computer time, a simple "geometric" MC was made for the less significant background processes. In this MC, the pair rejection calculated with the full drift chamber MC was used. This pair rejection was parameterized versus the momentum of the non–triggering electron.

6.1 PARENT PRODUCTION

Two things were needed for the MC as far as the parent production was concerned:

- a parameterization of the cross section in P_T and rapidity (y);
- the number of parent particles per pion integrated over P_T (X_π).

The first requirement was fulfilled by fits to measurements done by other experiments in the case of π's and K's and by using a form of m_T scaling (described below) for the rest of the particles. A specific measurement of η/π at low P_T was performed in order to check the validity of m_T scaling for η mesons.

6.1.1 π PRODUCTION

A parameterization of the measured P_T spectrum for pions was used, as given in [70]:

$$E\cdot\frac{d^3\sigma}{dP} = A\cdot e^{-B\cdot P_T}\cdot e^{-C\cdot Y^2} + D\cdot\frac{(1-P_T/P_B)^m}{(P_T^2+M^2)^4} \qquad \text{where}$$

$E\cdot d\sigma^3/d\bar{p}$	the invariant differential cross sections;
P_T	the transverse momentum;
Y	the rapidity;
P_B	the beam momentum.

with A = 210, B = 7.58, C = 0.06, D = 10.7, M = 1.03 and m = 10.9 for π^+;
with A = 205, B = 7.44, C = 0.06, D = 12.8, M = 1.08 and m = 13.1 for π^-.

There exists another measurement of pion production at the ISR [71] which has smaller systematic errors at very low P_T. This parameterization, however, is not valid at high P_T and was therefore only used to estimate the systematic error in the pion parameterization at $P_T < 200$ MeV/c, where pions could not be measured in the AFS experiment (see chapter 7). Isospin invariance was assumed with $\pi^0 = (\pi^+ + \pi^-)/2$ and therefore isospin breaking processes like $\eta \to \pi^0\pi^0\pi^0$ had to be added separately. The constant C in the formula above which determines the rapidity dependence was made smaller so that the parameterization would agree more with the measured data (see fig. 24 in [70]). Since the rapidity coverage of the triggering scintillation counters was very small, the rapidity range of parents contributing to the e/π ratio at y = 0 was limited to ± 1 unit in rapidity and the result was not strongly affected by the rapidity dependence.

6.1.2 K PRODUCTION

The parameterization used for the kaon production was the same as for the pion production described above, but with the following values of the constants:
$A = 14.3$, $B = 6.78$, $C = 0.075$, $D = 8.0$, $M = 1.29$ and $m = 12.1$ for K^+ and
$A = 13.4$, $B = 6.51$, $C = 0.075$, $D = 9.8$, $M = 1.39$ and $m = 17.4$ for K^-.
It was assumed that $K^0 = (K^+ + K^-)/2$.

For the calculation of the integrated K/π ratio, one parameterization [71] was used for $P_T < 300$ MeV/c and another parameterization [70] was used for $P_T > 300$ MeV/c. Both parameterizations were based on measurements at $\sqrt{s} = 53$ GeV since the measurement at $\sqrt{s} = 63$ GeV had large statistical errors. The result of the integration was $K^+/\pi^0 = 0.087$ and $K^0/\pi^0 = 0.080$.

6.1.3 η PRODUCTION

The decay products from the η meson were the second largest source of background electrons at low P_T. The η/π ratio has been measured by several experiments at $P_T > 1$ GeV/c and found to be constant (0.55) [8] [72] – [78]. Below 1 GeV/c the situation was more uncertain. Some bubble chamber experiments [79] – [87], dominated by low $-P_T$ production, have reported lower η/π ratios than 0.55 which suggests a decrease for $P_T < 1$ GeV/c. Previous experiments which have studied electron production at low P_T have used a parameterization of the inclusive production in terms of the transverse mass ($m_T = \sqrt{(m^2 + P_T^2)}$), the so–called m_T scaling [88] – [89]. The following formula derived by [88] was used in this experiment:

$$\frac{X}{\pi}(P_T) = \frac{X}{\pi}(\infty) \cdot \left(\frac{\sqrt{P_T^2 + M_X^2} + 2}{\sqrt{P_T^2 + M_\pi^2} + 2} \right)^{12.3} \quad \text{where}$$

$x/\pi(P_T)$	the particle to pion ratio as a function of P_T;
$x/\pi(\infty)$	the particle to pion ratio at $P_T >> M_X$;
P_T	the transverse momentum;
M_X	the particle mass;
M_π	the pion mass.

The validity of this parameterization had been checked with other mesons such as K, ρ, ω, ϕ and J/ψ mesons but due to the lack of experimental data at low P_T in the case of η mesons the assumption about m_T scaling could introduced a large systematic error in the final result of the MC calculation. For this reason a measurement was performed of the η/π ratio at low P_T as described in chapter 8. Although the statistical errors in this measurement are quite large the results are in agreement with a drop at low P_T as expected from m_T scaling and this new measurement significantly reduced the systematic error in the calculation of the remaining single electron background.

6.1.4 η', ρ, ω AND ϕ PRODUCTION

For η',ρ,ω and ϕ the same type of m_T scaling was used as for η. The m_T scaling function was normalized at high P_T (>5GeV/c) to 0.9 for ρ/π, ω/π and η'/π and to 1.0 for ϕ/π. This gave an integrated parent-to-pion ratio of $\rho/\pi=0.109$, $\omega/\pi=0.110$, $\eta'/\pi=0.0629$ and $\phi/\pi=0.0599$.

6.1.5 PRODUCTION OF CHARMED PARTICLES

For hidden charm (i.e. J/ψ) a value of the branching ratio times $d\sigma/dy$ of $14.8\cdot10^{-33}$ cm^2 [90] was used to calculate $B\cdot X_\pi$ ($=5\cdot10^{-7}$). This process, however, contributes negligible to the e/π ratio at low P_T.

The absolute cross section and Feynman-x dependence of open charm production (i.e. D mesons) at the ISR energies are not well known [13]– [16] [91] [92]. However, most experiments agree on the shape of the P_T spectrum as something like $d\sigma/dP_T \sim P_T\cdot e^{-\alpha P_T}$ where $\alpha\simeq2.5$ [15] [91] [92]. This means that the contribution from electrons originating from D mesons will have a maximum at $P_T=600-800$ MeV/c, i.e. the contribution will be decreasing at lower P_T. The measured e/π ratio at 600–800 MeV/c thus gives an upper limit for the possible contribution from open charm. In the MC calculations a branching ratio of 8% for $D\rightarrow eK^{(*)}\nu$ [14] [16] and an integrated D/π ratio of 0.0013 was used which gives a contribution in e/π of $\sim2\cdot10^{-4}$ at $P_T=700$ MeV/c. This means that the measured e/π ratio at this P_T can be fully explained by charm, hadronic bremsstrahlung and vector meson decay. The true contribution from open charm, however, might very well be lower (but not higher). The large uncertainty in the MC calculations of the charm contribution was one of the reasons why this process could not be subtracted from the measured e/π ratio.

6.2 e^+e^- PAIRS FROM REAL PHOTONS

6.2.1 γ CONVERSIONS

The main source of background, in this experiment, came from conversions of real photons. The amount of material between the vertex point and the drift chamber is given in table 11 . The total amount of material corresponded to 4.89% of a radiation length. The energy distribution was simulated according to Bethe–Heithlers formula in a form given by Rossi [93]:

$$\phi(\omega,\varepsilon) \sim (\varepsilon^2+(1-\varepsilon)^2)\cdot(f_1(\delta)/4 - \ln(Z)/3)+2\cdot\varepsilon\cdot(1-\varepsilon)\cdot(f_2(\delta)/4 - \ln(Z)/3)/3$$

where

ε	The helicity (or fractional energy of the positron = E/ω).
E	The energy of the positron.
ω	The energy of the photon.

δ	The screening variable $=100 \cdot Z^{-1/3} \cdot (m/\omega)/(\varepsilon(1-\varepsilon))$.
m	The electron mass.
Z	The atomic number of the medium in which the conversion occurs.

The screening functions (f_1 and f_2) can be approximated with the following expressions [94]:

$$f_1(\delta) = 21.12 - 4.184 \cdot \ln(\delta + 0.952) \quad \text{if } \delta > 1$$
$$f_2(\delta) = f_1(\delta) \quad \text{if } \delta > 1$$

$$f_1(\delta) = 20.867 - 3.242 \cdot \delta + 0.625 \cdot \delta^2 \quad \text{if } \delta < 1$$
$$f_2(\delta) = 20.209 - 1.930 \cdot \delta + 0.086 \cdot \delta^2 \quad \text{if } \delta < 1$$

All generated photons were forced to convert but the conversion point was chosen according to the relative weight of the different materials and smeared randomly across the material in order to simulate the proper distribution of energy loss. Most of the events (the exceptions being events with ω and η' parents) were passed through the full drift chamber MC. The MC events were then passed through the standard analysis programs and the events that survived the pair rejection cuts were weighted with $1 - e^{-P}$ where P was the absolute probability for a photon to undergo γ conversion. The following energy and material dependent parameterization of the total probability for a γ conversion was used:

$$P(Z,e) = x/(4 \cdot \ln(183 \cdot Z^{-1/3}) \cdot (F(e) - 28 \cdot (\ln(Z) + 3 \cdot C(Z))/27) \cdot G(e) \text{ where}$$

$$C(Z) = a \cdot (1/(1+a) + 0.202 - 0.0369 \cdot a + 0.0083 \cdot a^2 - 0.002 \cdot a^3) \text{ and}$$

$$F(e) = -0.653 + 1.530 \cdot \ln(e) + 0.381 \cdot (\ln(e))^2 \quad \text{if } e < 12 \text{ MeV}$$
$$F(e) = 16.37 + 91.63/e - 89.37 \cdot \ln(e)/e \quad \text{if } e > 12 \text{ MeV}$$

$$G(e) = -0.435 - 0.0570 \cdot \ln(e) - 0.0457 \cdot (\ln(e))^2 \quad \text{if } e < 12 \text{ MeV}$$
$$G(e) = 1.071 + 19.75/e - 14.34 \cdot \ln(e)/e \quad \text{if } e > 12 \text{ MeV}$$

P	the absolute probability for a γ to undergo conversion;
x	the thickness of the material in fraction of a radiation length ($=X'/X_0$);
X'	the thickness of the material in g/cm^2;
X_0	the radiation length in g/cm^2 ($=(4\alpha r^2 NZ(Z+1)\ln(183Z^{-1/2})/A)^{-1}$);
N	Avogadro's number;
A	the mass number of the material;
Z	the atomic number of the material;
α	the fine structure constant ($\simeq 1/137$);
r	the classical electron radius ($\simeq 2.818$ fm);
e	$=\omega/Z^{1/3}$;
ω	the energy of the photon;
a	$=(\alpha \cdot Z)^2$;
C(Z)	the Coulomb correction function.

Table 11: The amount of material between the vertex and the DC.

Type of material	**X′**	**X_0**	**x**	**Z/A**	**K·10³**
Beam pipe:					
Stainless Steel (99%Fe+1%C)	0.247	13.84	1.79%	0.466	17.3
Inner Hodoscope:					
Plastic Scint. ($C_{19}H_{21}$)	0.648	43.8	1.48%	0.541	52.6
PVC plastic (C_2H_3Cl)	0.0874	43.8[1]	0.20%	0.512	6.7
Aluminium foil	0.0189	24.01	0.08%	0.482	1.4
Drift chamber wall:					
G10 (*)	0.321	33.0	0.97%	0.513	24.7
Copper coating	0.030	12.86	0.24%	0.456	2.1
Glue ($C_{14}H_{20}O_3$)	0.028	40.55[2]	0.07%	0.542	2.3
Rohacell (expanded $C_5H_8O_2$)	0.024	40.55	0.06%	0.539	1.9
Sum of all material			**4.89%**		**109.0**

* 40% $C_{14}H_{20}O_3$ + 41% Al_2O_3 + 3% CaO + 12% SiO_2 + 4% MgO
[1] assumed to be the same as for plastic scintillators
[2] assumed to be the same as for plexiglass

X′	the thickness of the material in g/cm²;
X_0	the radiation length in g/cm²;
x	the ratio X'/X_0;
Z	the atomic number of the material;
A	the mass number of the material;
K	a material depending quantity used in the Compton scattering calculation (=C·X′·Z/A) see section 6.4.3 .

This formula was obtained by modifying an expression for the total pair cross section given in [95]. The definition of radiation length ($X_0^{-1} = 4\alpha r^2 NZ(Z+1) \ln(183Z^{-1/2})/A$) that was used, when this cross section formula was transformed into a formula for probability per X_0, was similar to that in [96].

This was important since the X_0 in table 11 that was used to calculate the final conversion probability originated from [96]. The accuracy of the formula was tested with tabulated values [97] and was found to be within the errors of the tabulated data.

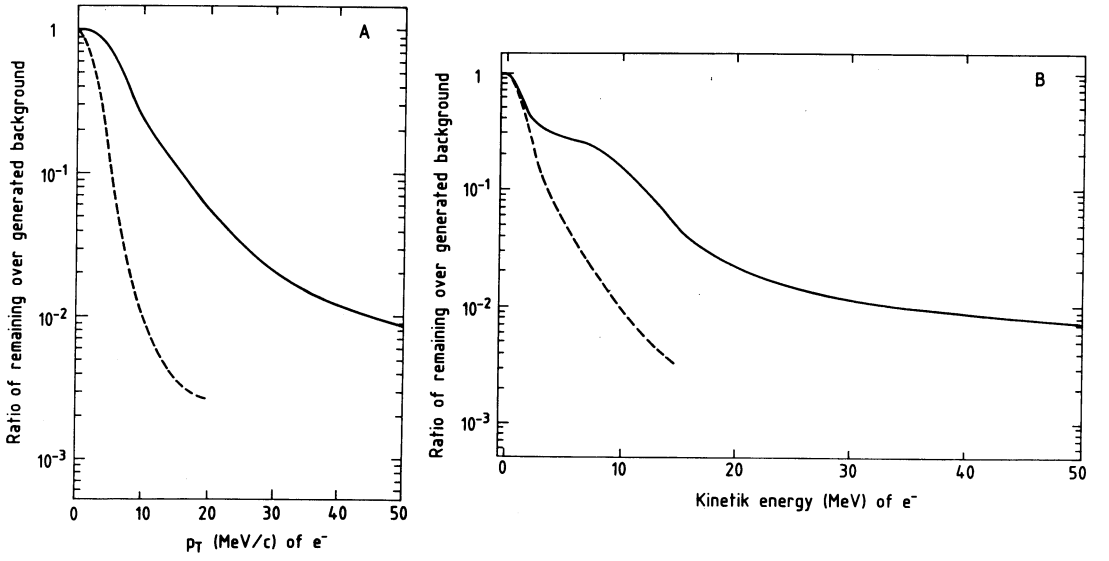

Figure 34: The pair rejection as a function of A) the P_T of the e^- and B) the kinetic energy of the e^-. The full line shows the rejection for π^0 Dalitz decays and the dashed line the same for converted photons originating from π^0 decays.

Figure 34 shows the probability that a pair would survive, the cuts in the analysis, as a function of the P_T and kinetic energy ($\simeq$ momentum) of the non – triggering electron in the pair. This is plotted for two different cases namely pairs from conversions of photons from π^0's and pairs from π^0 Dalitz decays. The difference in rejection depends mostly on where, in space, the pair was created. Dalitz pairs, which were produced at the vertex, would to a larger extent curl – up and never reach the drift chamber, than the conversion pairs which were produced closer to the DC and thus had a larger probability to enter it. In addition, the larger opening angle for Dalitz decays, compared to conversions, made it a bit more difficult to reject them with the cuts on unassigned digitizings.

6.2.2 HADRONIC BREMSSTRAHLUNG OF REAL PHOTONS

When a number of charged particles are suddenly created in a pp collision there will be a subsequent production of hadronic (or inner) bremsstrahlung [40] – [46]. Goshaw et al. [42], who studied direct photon production, used the following expression to calculate the yield of real photons from this process:

$$\frac{d^3\sigma_\gamma}{d\bar{k}} = \frac{\alpha}{4\pi^2} \cdot \frac{1}{\omega} \int d^3\bar{P}_1 \cdots d^3\bar{P}_n \left(\sum_{i,j} \frac{-Q_i Q_j P_i \cdot P_j}{(k \cdot P_i)(k \cdot P_j)} \right) \cdot \frac{d\sigma_H}{d^3\bar{P}_1 \cdots d^3\bar{P}_n} \quad \text{where}$$

σ_γ	the bremsstrahlung cross section;
σ_H	the charged hadron production cross section;
P_i	the four momentum of the charged hadron i;
$\bar{P}_i$	the three momentum of the charged hadron i;
Q_i	the charge of hadron i;
k	the four momentum of the bremsstrahlung photon;
$\bar{k}$	the three momentum of the bremsstrahlung photon;
ω	the energy of the bremsstrahlung photon;
α	the fine structure constant.

In this experiment a more classical approach was adopted and an expression by Cahn [44] in the following form was used in the MC program:

$$\frac{dN_\gamma}{dy dk_T^2} = \frac{\alpha}{4\pi} \cdot \frac{1}{\omega^2} \cdot \beta^2 \cdot \frac{\sin^2\Theta}{(1-\beta \cdot \cos\Theta)^2} \quad \text{where}$$

N_γ	the number of bremsstrahlung photons;
y	the rapidity of the photon;
k_T	the transverse momentum of the photon;
ω	the energy of the photon;
α	the fine structure constant;
β	the velocity of the charged particle;
θ	the angle between the charged particle and the photon.

With this formula the energy and angular dependence of the bremsstrahlung photons could be generated in the MC. Charged pions were used as the only parent particles. These pions had to be generated over a large rapidity interval because even pions at high rapidity could contribute to the bremsstrahlung spectrum at $y=0$. The result of the calculations with this MC program was compared to other calculations [40] – [41] and was found to give about 30 – 40% higher results.

The real photons originating from bremsstrahlung did not contribute to the measured e/π in a significant way since the rejection of conversion pairs was very effective. On the other hand, pairs originating from high mass virtual bremsstrah-

lung photons did contribute in a substantial way. This will be discussed in more detail in section 6.3.2 below.

6.3 e^+e^- PAIRS FROM VIRTUAL PHOTONS

6.3.1 DALITZ DECAY

The Dalitz decay (or internal conversion) of π, η and η' into a virtual photon and a real photon, with a subsequent decay of the virtual photon into a massive e^+e^- pair, was generated with the well known Kroll–Wada formula [98] – [100], [45]. This formula parameterizes the mass dependence of Dalitz decays:

$$\frac{dN_{ee}}{dMdydk_T^2} = \frac{4\alpha}{3\pi} \cdot \frac{1}{M} \cdot \sqrt{1-\frac{4m^2}{M^2}} \cdot \left(1+\frac{2m^2}{M^2}\right) \cdot \left(1-\frac{M^2}{\mu^2}\right)^3 \cdot \frac{dN_\gamma}{dydk_T^2} \quad \text{where}$$

N_{ee}	the number of massive e^+e^- pairs produced by Dalitz decay;
α	the fine structure constant;
M	the mass of the e^+e^- pair;
m	the mass of an electron;
μ	the mass of the parent meson;
N_γ	the number of produced real photons from conversion;
y	the rapidity of the real photon;
k_T	the transverse momentum of the photon.

The generated angular dependence in the MC was $1+\cos^2\theta$ [99] where θ was the angle between the directions of the electron and the virtual photon in the CM system of the electron pair. The generated events were processed through the full drift chamber MC. The P_T spectrum of generated photons and virtual photons had almost the same shape but differed in magnitude by a factor of 160 ($=2\cdot B$ where the factor 2 comes from the number of photons created in a γ conversion compared with a Dalitz decay).

6.3.2 HADRONIC BREMSSTRAHLUNG OF VIRTUAL PHOTONS

In section 6.2.2 the generation of real photons from hadronic bremsstrahlung was described. A larger contribution to the measured e/π ratio comes from hadronic bremsstrahlung of virtual photons since the e^+e^- pairs from this process have a larger probability to survive the mass cut and the other pair rejection cuts. If it is assumed that the cross section for hadronic bremsstrahlung of virtual photons is proportional to the cross section of the production of real bremsstrahlung photons and that the e^+e^- pairs are produced by internal conversion then the following formula [35] [46] describing the mass dependence is obtained:

$$\frac{dN_{ee}}{dMdydk_T^2} = \frac{2\alpha}{3\pi} \cdot \frac{1}{M} \cdot \sqrt{1-\frac{4m^2}{M^2}} \cdot \left(1+\frac{2m^2}{M^2}\right) \cdot \sqrt{1-\frac{M^2}{\omega^2}} \cdot \frac{dN_\gamma}{dydk_T^2}$$ where

N_{ee}	the number of massive e^+e^- pairs produced by bremsstrahlung;
M	the mass of the e^+e^- pair;
m	the electron mass;
α	the fine structure constant;
ω	the energy of the virtual photon;
N_γ	the number of produced real bremsstrahlung photons;
y	the rapidity of the real photon;
k_T	the transverse momentum of the photon.

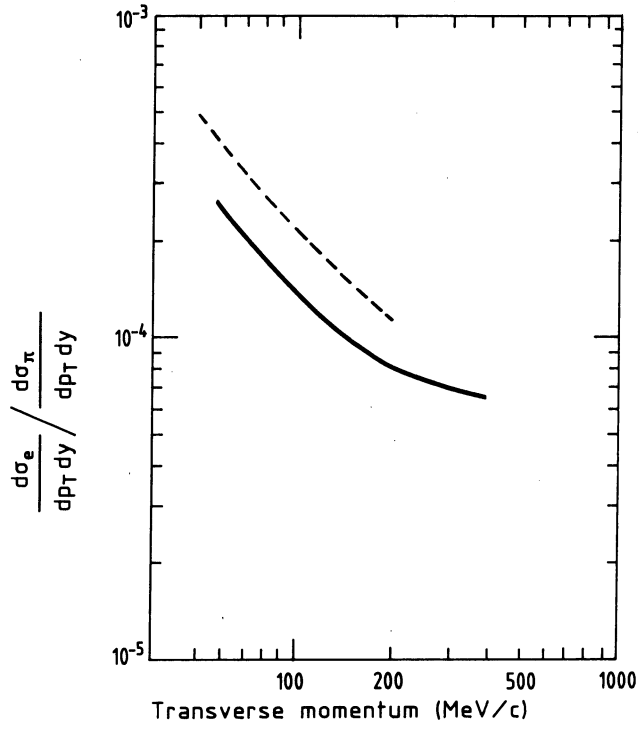

Figure 35: Calculations of the e/π ratio from hadronic bremsstrahlung. The full line is the calculation done by this experiment and the dashed line is from [41].

This formula is almost identical to the expression given in section 6.3.1 for the mass dependence of e^+e^- pairs from Dalitz decays. The expression for the real photons was given in section 6.2.2 above. The normalization in the MC is trivial since it is an absolute normalization which means that the ratio of the P_T spectrum of the generated positrons, which passed through the fiducial trigger volume, divided with the P_T spectrum of the parent pions, which passed through the same volume, directly gives the contribution to the measured e/π ratio. The main feature of hadronic bremsstrahlung (as well as for the Dalitz decays) is the 1/M behaviour of the mass spectrum and an increasing contribution to the e/π ratio with decreasing P_T, as can be seen in fig. 35 . A calculation (made by [41]) of the contribution to the e/π ratio from virtual bremsstrahlung photons, with a requirement of a minimum opening angle of the e^+e^- pair of 5^0, is also presented in this figure. This calculation gives a result which is about 50% higher than the calculation made in this experiment, but this can at least be partly explained with the difference between an angle cut of 5^0 and the somewhat harder mass cut of 100 MeV/c^2 which was used in this experiment. The systematic error in the bremsstrahlung calculation is estimated to be 40 – 50%. This error takes into account the fact that the contribution from real bremsstrahlung photons has not been subtracted from the measured e/π ratio (which is the same procedure that previous experiments have used).

6.3.3 THE DECAY OF ρ, ω, ϕ AND J/ψ INTO e^+e^-

The mesons ρ, ω, ϕ and J/ψ were decayed into virtual photons which subsequently were decayed into massive e^+e^- pairs (group b3). The contribution from these decays to the measured e/π ratio was small at low P_T (see fig. 42). This form of background was not subtracted from the data since previous experiments had not done so and it was desirable to get results that could be compared.

6.4 BACKGROUND OF SINGLE ELECTRONS AND POSITRONS

6.4.1 Ke_3 DECAY

The rejection of positrons originating from Ke_3 decays is described in section 5.2.1 . Two different MCs were written to calculate this background. One of the MC programs was used to estimate the background from Kaons decaying before the drift chamber and the other program was used to study Kaons that decayed after the drift chamber. The two MCs started in a similar way by generating the parent and then letting it decay, taking into account the V – A matrix element.

The first MC simulated the distance of closest approach between the positron track, extrapolated back by a circle approximation, and the vertex (the point where the kaon was generated). Fig. 36 shows the closest distance in the transverse plane from the trigger track to the primary vertex for positrons and pions. This figure also shows the vertex distribution, for positrons originating from kaons, calculated with the MC. A clear difference is seen in the data between the vertex distribution

for positrons and pions which can be explained by Ke_3 decay. In the analysis, it was required that the distance in the transverse plane was less than 1.5 cm while the distance in the Z direction had to be less than 12 cm.

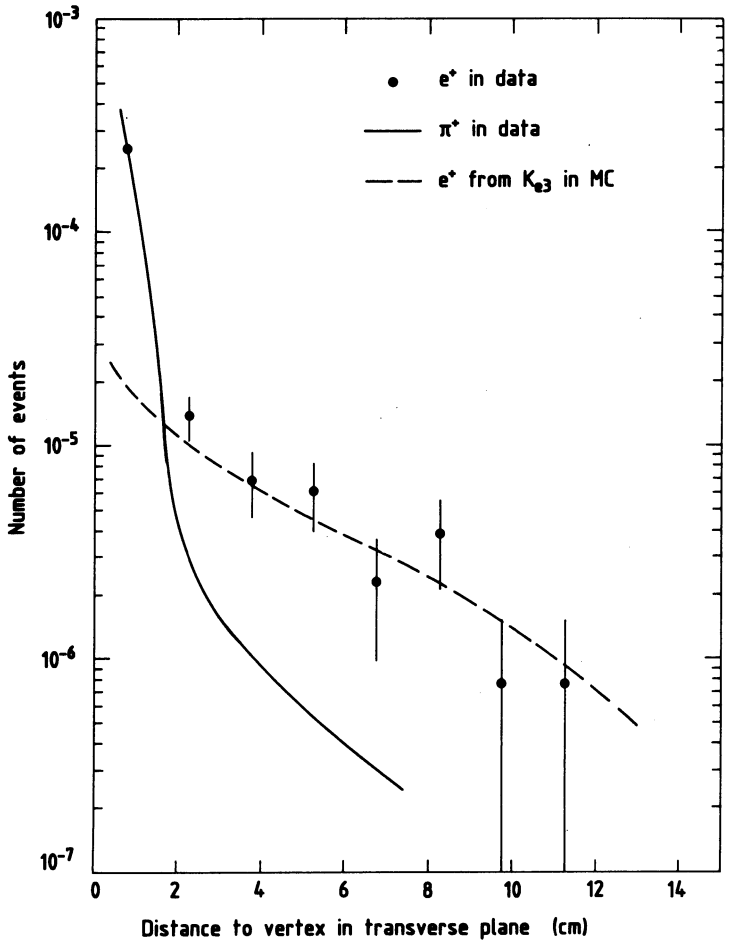

Figure 36: The vertex distribution.

The kaons which passed through the drift chamber and decayed before or inside the Cherenkov detector were studied by a separate MC program. In this program the kaons and positrons were tracked through the magnetic field until they reached the NaI detector. The different requirements on the position of the extrapolated trigger track at the NaI detector gave a large rejection against this type of back-

ground. The TOF and dE/dx requirements (which were incorporated in the MC) cut away almost all kaons with a momentum less than 700 MeV/c and, therefore, the P_T distribution of positrons originating from kaons decaying after the DC had a maximum at high P_T.

6.4.2 DECAY OF CHARMED PARTICLES

After the generation of the D mesons (described in section 6.1.5), the decay was made according to simple phase space considerations. An equal probability was used for the two semileptonic decays into $eK\nu$ and $eK^*\nu$ and the average branching ratio for semileptonic decays was taken to be 8% [16].

6.4.3 COMPTON SCATTERING

In order to test the MC, the contribution of electrons coming from Compton scattering of photons was measured. This contribution can be calculated with the data by subtracting the number of produced e^+ from the number of e^- since Compton scattering is the only process that creates a significant amount of only e^-. In the MC the energy and angle of the Compton scattered photons were generated with the quantum mechanical Klein – Nishina formula [101] – [103]:

$$\Phi(\omega,\omega') = C \cdot \frac{m}{\omega} \cdot \left(\varepsilon+\frac{1}{\varepsilon}\right) \cdot \left(1-\frac{\varepsilon\cdot\sin^2\Theta}{1+\varepsilon^2}\right) \quad \text{where}$$

$\Phi(\omega,\omega')$	the differential cross section for Compton scattering;
C	a material depending constant ($=X_0\cdot n\cdot\pi\cdot r^2$);
m	the electron mass;
ω	the energy of the incident photon;
ω'	the energy of the scattered photon;
ε	the ω'/ω ratio;
θ	the scattering angle.

From the calculated value of energy and angle of the scattered photons it was possible to calculate the momentum vector of the recoil electron assuming an elastic collision.

All generated photons were forced to undergo Compton scattering in a similar way as in the calculation of the background from γ conversions. The events were passed through the full drift chamber MC and then through the standard analysis programs. It was clear from this simulation that it was hardly possible to reject any electrons since the direction of the electron was very similar to that of the photon and thus pointed back to the vertex. The events that survived the vertex requirement and other cuts were weighted with $1-e^{-P}$ where P was the absolute probability for a photon to undergo Compton scattering. The following energy and material dependent parameterization of the probability for Compton scattering was used (from Rossi [93]) :

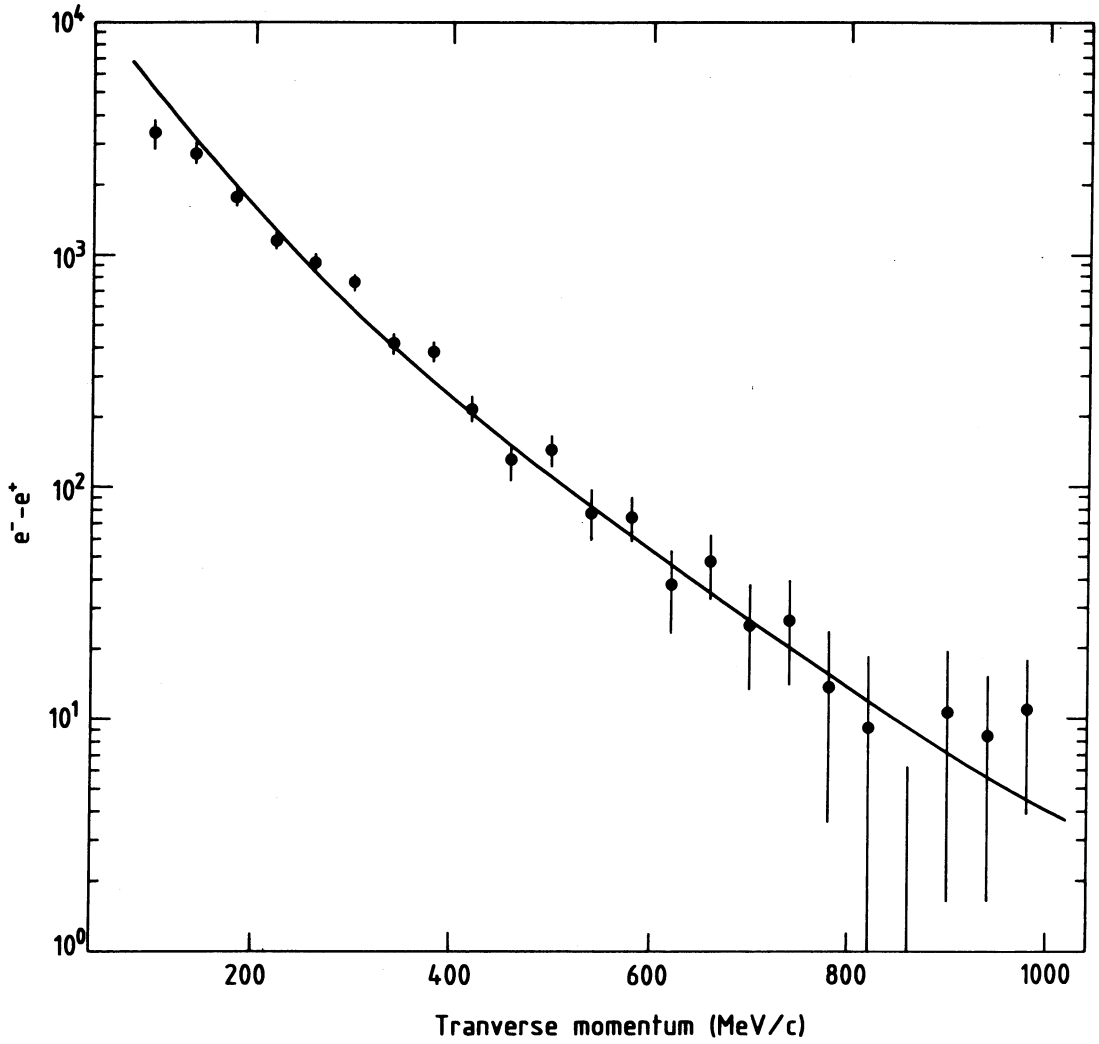

Figure 37: The distribution of the difference $e^- - e^+$, i.e. between the number of produced electrons and positrons, versus P_T. The curve shows the MC calculation of the expected contribution of electrons from Compton scattering normalized to the integrated π spectrum.

$$P(Z,e) = C \cdot X' \cdot (Z/A) \cdot (\ln(2 \cdot e) + 1/2)/e \quad \text{where}$$

P	the probability for Compton scattering;
C	a constant ($=\pi \cdot N \cdot r^2 \simeq 0.150\ g^{-1}cm^2$);
N	Avogadro's number;
r	the classical electron radius ($\simeq 2.818$ fm);

X'	the thickness of the material in g/cm^2;
Z	the atomic number of the material;
A	the mass number of the material;
e	$=\omega/m$;
ω	the energy of the incident photon;
m	the electron mass.

Fig. 37 shows the results of the measurement compared with the MC predictions. The importance of this test lies in the fact that the Compton background and the background from converted γ's are both depending on the amount of material between the vertex and the drift chamber, so this test proves that the amount of material has been correctly accounted for in the MC.

6.5 TESTS OF THE MONTE CARLO CALCULATIONS

Since the final results of this analysis depends crucially on an accurate MC calculation of the residual positron background, a large effort has gone into testing the MC. One of the major origins of large systematic errors at low P_T in previous experiments [18] was the unknown η/π ratio below a P_T of 1 GeV/c. Since the η/π ratio has been measured at low P_T in this experiment (fig. 47) and found to be compatible with m_T scaling, this source of systematic uncertainty has now been greatly reduced.

The comparison between the background from Compton scattering and the MC calculation for this process has been presented in figure 37 . In the lowest P_T bin (<100 MeV/c) a significant difference was observed between the data and the MC. This difference could be attributed to a systematic error either in the mass cut efficiency correction or in the parameterization of the pion P_T spectrum. The vertex cut could also result in an unaccounted loss of electrons at very low P_T. In the P_T region of $100-300$ MeV/c the MC calculation seems to be somewhat higher than the data and for $P_T > 300$ MeV/c the opposite occurs. The integrated value of the production of electrons in the data and the MC differ by only 5%, which implies that the amount of material that was used in the MC was correct.

A comparison was also performed, before any pair rejection cuts, between the sum of all background processes in the MC and the measured efficiency corrected e^+/π (the "raw" e/π), see fig. 38 . The normalization in this figure is an absolute normalization in e^+ per $(\pi^+ + \pi^-)/2$ and the agreement between data and MC is good. Perhaps the MC is overestimating the background somewhat in the P_T region $100-200$ MeV/c, but it seems as if the generated e^+/π background was essentially correctly normalized and had the correct P_T dependence.

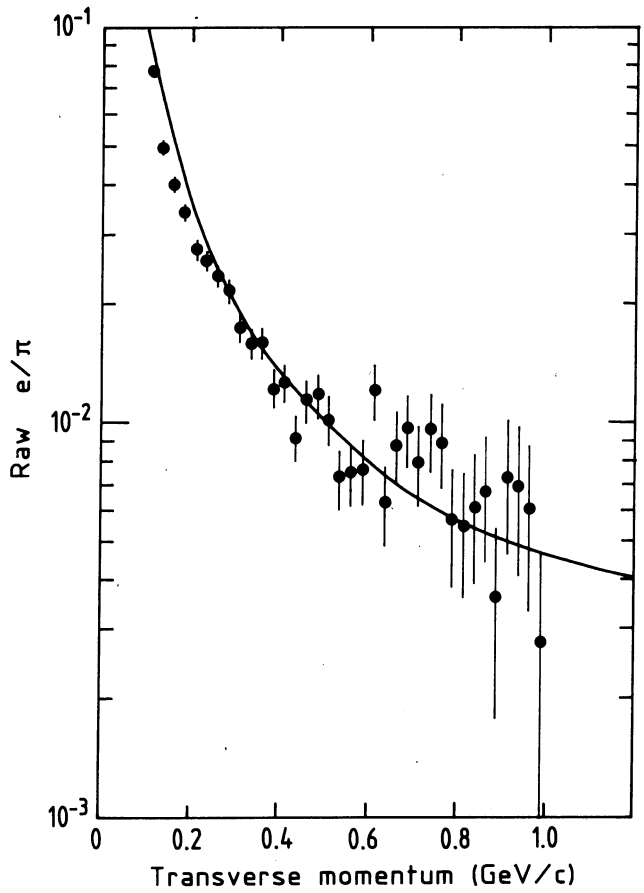

Figure 38: The raw e/π ratio in data and MC. The full line is the e/π ratio from the MC calculation.

The generation of γ conversions was tested by comparing the helicity and the mass distributions in the data and the MC. Figure 39 shows the absolute normalized helicity distribution for pairs with masses < 30 MeV/c^2. Again the shape is very well reproduced by the MC, this is particularly important at low and high helicity which corresponds to very asymmetric pairs. Once again the absolute magnitude of the background seems to be somewhat overestimated in the MC calculations. The mass distribution of $e^+x^- - e^+x^+$, where x is any other track found by the drift chamber, is plotted in fig. 40 and compared to the MC prediction. The agreement between data and MC is excellent for $m < 40$ MeV/c^2 where the combinatorial background in the data is negligible. This proves that the mass and hence the momentum resolution of the drift chamber is well described by the MC program.

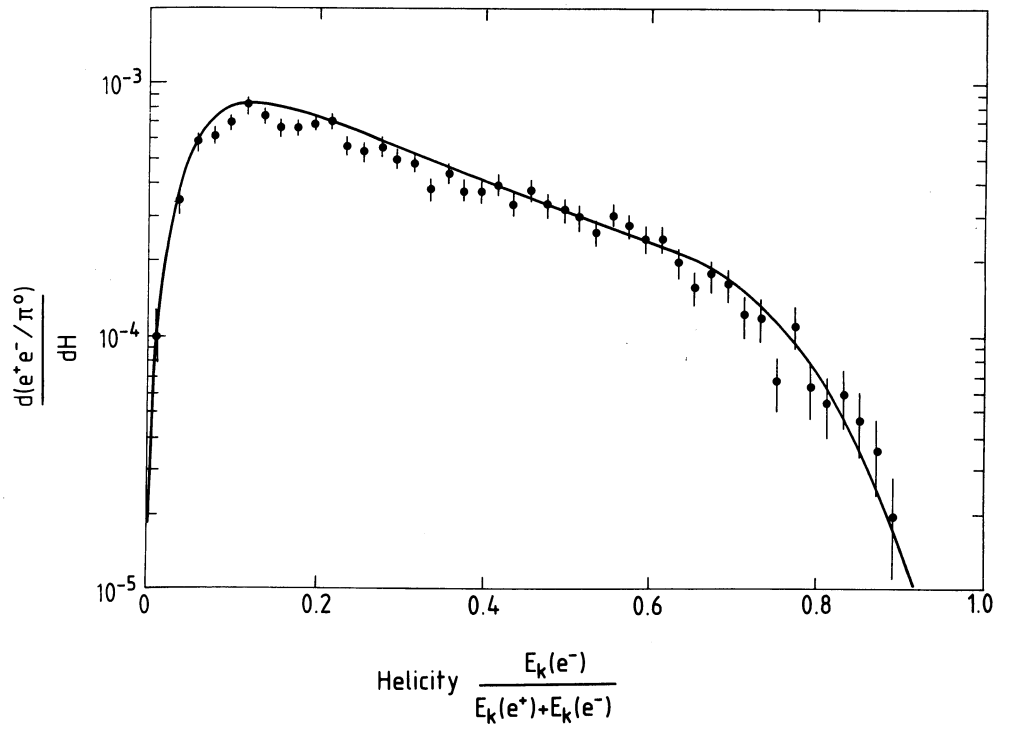

Figure 39: The helicity distribution.

The Kroll – Wada formula (see section 6.3.1) that was used to calculate the mass dependence of Dalitz decays is not strictly correct. A more exact description includes an electromagnetic form factor [35]. This form factor is estimated to change the shape of the mass distribution of pairs from π^0 Dalitz decays by 3 to 6% (at $m > 50$ MeV/c^2) [104] – [106]. The error, due to the form factor, in the MC calculated total background is therefore small.

The rejection of single positrons relied heavily on the vertex requirement. A comparison between data and MC is presented in section 6.4.1 (fig. 36). The positron sample has a long tail of events with a large distance (in the transverse plane) between the trigger track and the primary vertex which is not the case for the pion triggered events. The absolute normalized vertex distribution, calculated with the MC for positrons originating from Ke3 decays, can fully explain this tail as seen in fig. 36 .

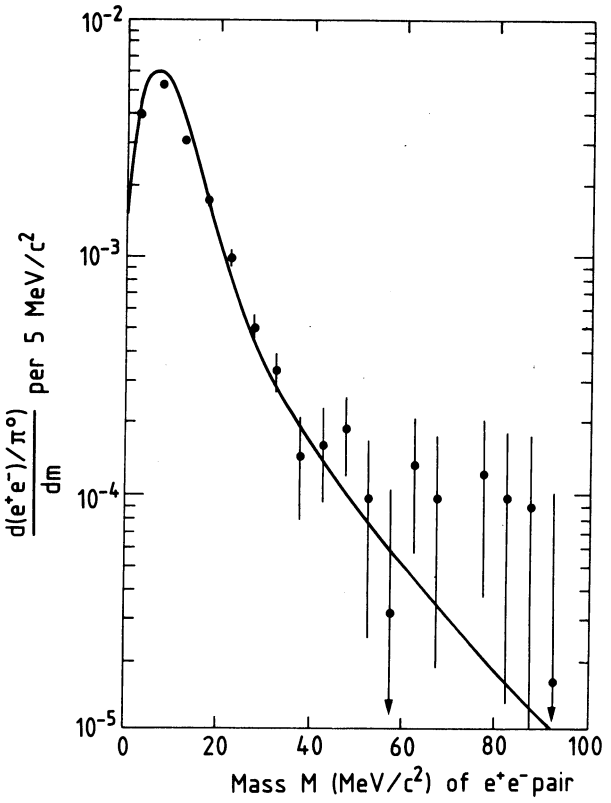

Figure 40: The mass distribution.

The vertex requirement was not only important for the rejection of different background sources of single positrons, but it was also useful in the rejection of low–mass pairs for which the mass was measured to be higher than the true mass because of multiple scattering. The sensitivity of the MC calculations to multiple scattering was tested by comparing the final calculated background with different assumptions about the multiple scattering in the MC. The simplest estimate of multiple scattering was done by using a Gaussian approximation of the scattering angle distribution with the rms of the distribution given by the well known formula [69] [107]:

$$\theta_{rms} = C \cdot (P \cdot \beta)^{-1} \cdot \sqrt{(x + \varepsilon(x))} \qquad \text{where}$$

θ_{rms}	the rms of the scattering angle distribution;
C	a constant (= 14.1 MeV/c);
P	the momentum of the particle in MeV/c;
β	the ratio of velocity to the speed of light;

x the thickness of the material in fraction of radiation length;
ε a correction function.

The Gaussian approximation does not describe large angle scattering very well. This type of scattering is most often due to one or a few deflections which give a large displacement of the particle trajectory, instead of the many small angle elastic scattering processes which are typical for normal multiple scattering. A method [108] was used in the MC in which the Moliere theory [109], and thus large angle scattering, was better described than by the Gaussian approximation. It turned out that the calculated remaining background was the same for the two different methods of calculating the multiple scattering. From this study it was clear that, because of the stringent vertex requirement, large angle scattering of individual electrons from low–mass pairs (< 100 MeV/c^2) did not introduce a background problem in the final positron sample.

An important input to the MC was the shape of the pion P_T spectrum. Here the parameterization used in the MC and the measured spectrum agree very well above a P_T of 200 MeV/c (fig. 44 below) which is the P_T region in which pions can be studied in this experiment. Different parameterizations were used to estimate the sensitivity of the calculations at low P_T to the shape of the pion spectrum.

The weakest point of the MC calculation was the generation of the dE/dx in the drift chamber and especially the generation of dE/dx from unresolved close pairs that were removed as doubly ionizing trigger tracks in the data. The number of Z measurements, which was also used to remove close pairs, was generated reasonably well in the MC. The combined rejection by the two cuts was assumed to give a similar result in the data and the MC, possibly with a small discrepancy resulting in an overestimate of the background. This would occur mainly at high P_T since for the two tracks to be unresolved both the electron and the positron in the pair had to have a high momentum.

6.6 SUMMARY OF REMAINING POSITRON BACKGROUND

The calculated remaining trivial background in the efficiency corrected measured e^+/π ratio is shown in fig. 41 . The main background comes from the decay of π^0's followed by the contribution from the η meson decay. At high P_T the background from kaons, especially those decaying after the drift chamber, becomes important. The full line corresponds to the sum of all trivial background sources. The systematic error in the MC calculation is estimated to be between $\pm 15\%$ and $\pm 20\%$, this uncertainty is illustrated as a shaded band in fig. 41 .

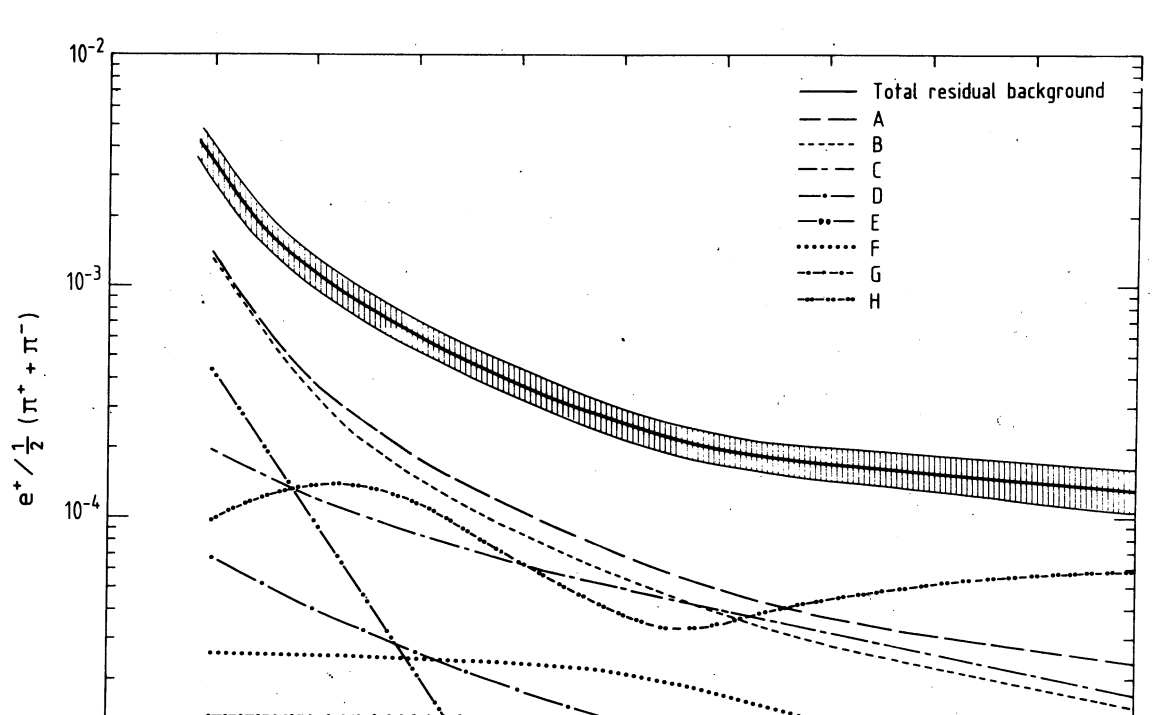

Figure 41: The trivial background sources of positrons.
A: π^0 γ conversions *B: π^0 Dalitz decay*
C: η^0 Dalitz decay *D: η^0 γ conversions*
E: $\eta^0 \rightarrow \pi^0\pi^0\pi^0$ Dalitz + γ conv. *F: η' Dalitz + γ conv.*
G: ω^0 Dalitz + γ conv. *H: K_{e3} decay*

The trivial remaining background was subtracted from the measured e^+/π as opposed to the so–called interesting positron sources (fig. 42). The most interesting known sources at low P_T are hadronic bremsstrahlung and semileptonic decay of charmed particles. The processes in fig. 42 , that were not included in the MC calculation, were beauty decay, Drell–Yan and ypsilon decay which all give a negligible contribution of positrons at low P_T. The curves in fig. 42 , which represent these processes, originate from [47].

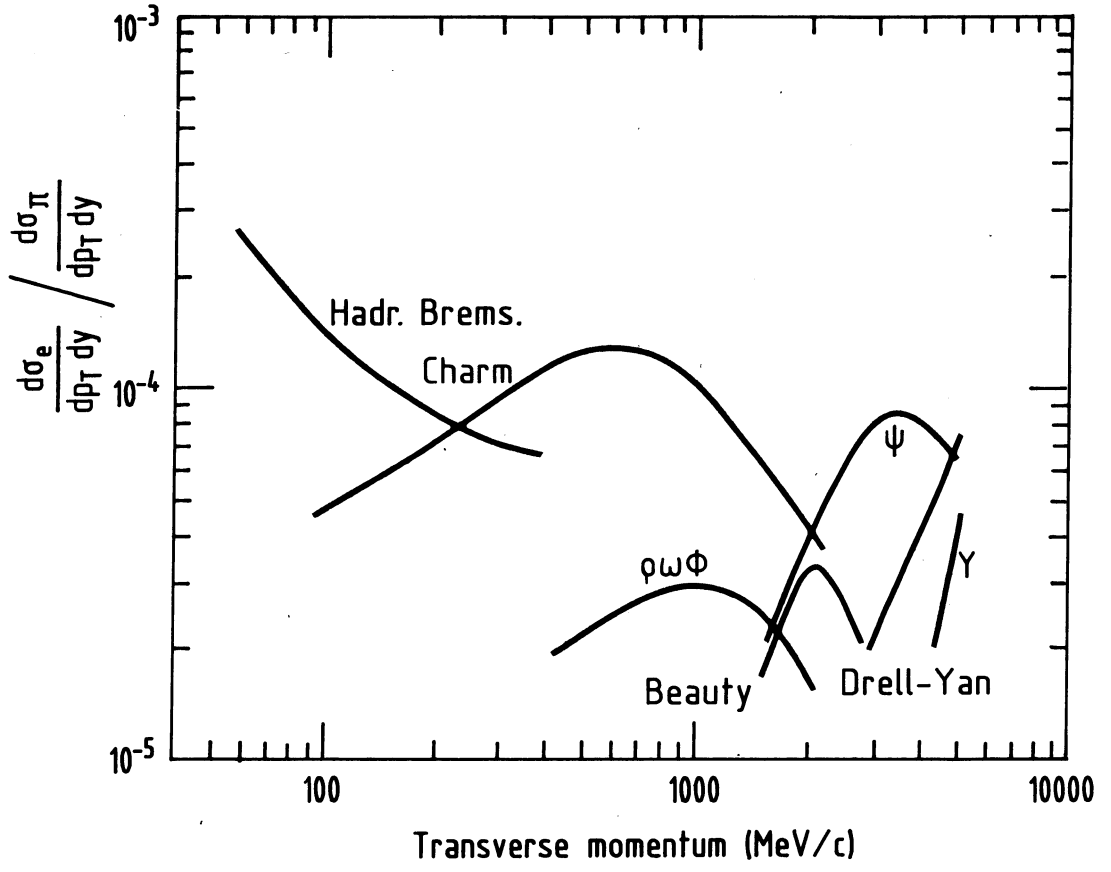

Figure 42: The interesting sources of positrons.

7. PIONS

The production of positrons was normalized to the production of pions for three reasons: Firstly, it was easier to do a pion normalization than to do a cross section measurement. The second reason was that many systematic uncertainties were the same for positrons and pions which meant that they cancelled when the e/π ratio was calculated. The final reason was that by calculating the e/π ratio, instead of the cross section, it was possible to compare the results of this experiment with previous ISR experiments.

Four different corrections had to be made to the measured pion P_T spectrum:

- an acceptance correction (correction factor A);
- correction for decay losses (correction factor D);
- correction for the efficiency of the NaI detector (correction factor N);
- correction for kaon contamination (correction factor K);

In the center–of–mass system the phase space in y and ϕ that was covered by the triggering scintillation counters depended on the momentum of the triggering pion. This was not true for positrons since they were relativistic in the momentum range of this experiment. The scintillator acceptance versus P_T for pions was calculated by the MC and the result is given in fig. 43 .

At low P_T a significant fraction of pions was lost due to decay into $\mu\nu$. This fraction was calculated with a separate MC program in which the pion was tracked through the magnetic field and decayed. The muon that was created in the pion decay was tracked to the scintillation counters. The number of pion triggers that were lossed due to decay was negligible if no position requirement (on the triggering pion) was made. The reason for this was that the number of pions which would have hit the scintillation counter, and where the muon escaped detection, was nearly the same as the number of pions that would have missed the counter, but where the muon triggered the scintillator. However, the requirement of a match between the position of the shower in the NaI detector and the position of the extrapolated track from the drift chamber, made the decay losses substantial at low P_T (see fig. 43).

All the different position requirements that were made on the positrons (see section 4.2) were also made on the pions. This was done since the NaI detector was not fully efficient in the whole region covered by the scintillation counters. The requirement of a shower in the NaI detector for both positrons and pions introduced an inefficiency which was to a large extent cancelled when the e/π ratio was calculated. However, it was found that positrons had a somewhat higher probability of giving a shower than the pions and this difference had to be corrected for (see fig 43). At low P_T (<200 MeV/c) a large fraction of the pions could not reach the NaI crystals anymore due to energy losses in the material between the vertex and the detector. A photodiode was glued to the front face of each NaI crystal and the diode was connected to a preamplifier also positioned in front of the crystals. This material, which

covered about 50% of the front area of the crystals, was equivalent to as much as 26 mm of Aluminium. The rest of the material between the vertex and the NaI crystals was more uniformly distributed and was equivalent to about 16 mm of Aluminium.

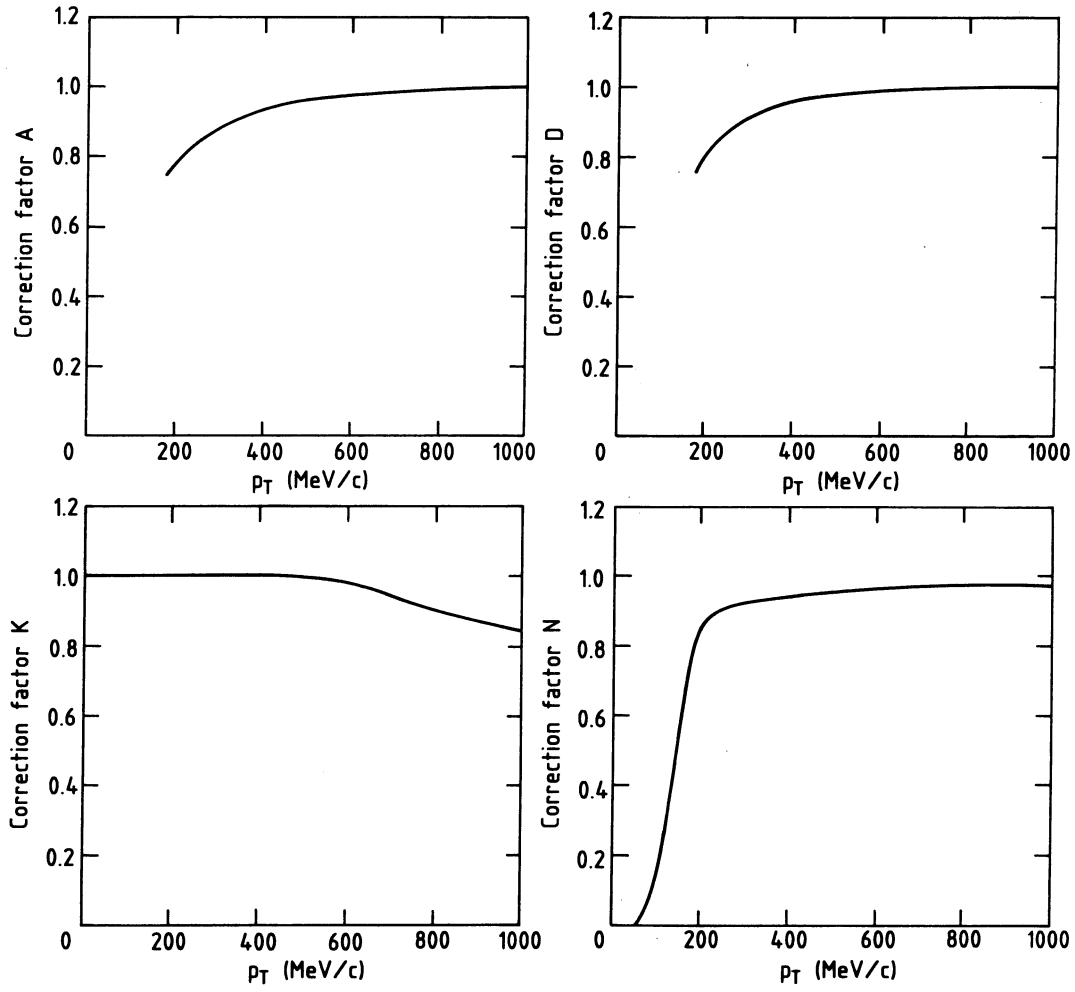

Figure 43: The four correction functions for the pions:
A) Acceptance corrections.
D) Decay corrections.
N) Efficiency corrections.
K) Correction for kaon contamination

The final correction that had to be done was due to kaon contamination. Two cuts were used to remove protons and kaons; one on the dE/dx and one on the TOF. These cuts were very loose (efficiency = 99%) but they removed nearly all protons and a large fraction of the kaons. The remaining fraction of kaons in the pion sample was calculated and the result of this calculation is given fig. 47 .

The P_T spectrum of the measured $\pi^+ + \pi^-$, after corrections, is shown in fig. 44 . Below a P_T of 200 MeV/c (in CM) pions could not be measured due to energy and decay losses. Note that the Lorentz boost was in the opposite direction to the triggering scintillators. The parameterization from [70] for $\pi^+ + \pi^-$ is plotted as a full line in fig. 44 . The normalization to this parameterization was made to the integral of the P_T spectrum between 200 and 1000 MeV/c. The parameterization of the pion P_T spectrum in [71] is more accurate at very low P_T than the parameterization that was used, but this second formula describes the pion spectrum only up to $P_T \approx 400$ MeV/c and was therefore difficult to normalize to. It was, however, used in the estimate of the systematic errors. In the final calculation of the e/π ratio, the measured corrected pion spectrum was used for $P_T > 200$ MeV/c and the pion spectrum from [70] was used for $P_T < 200$ MeV/c.

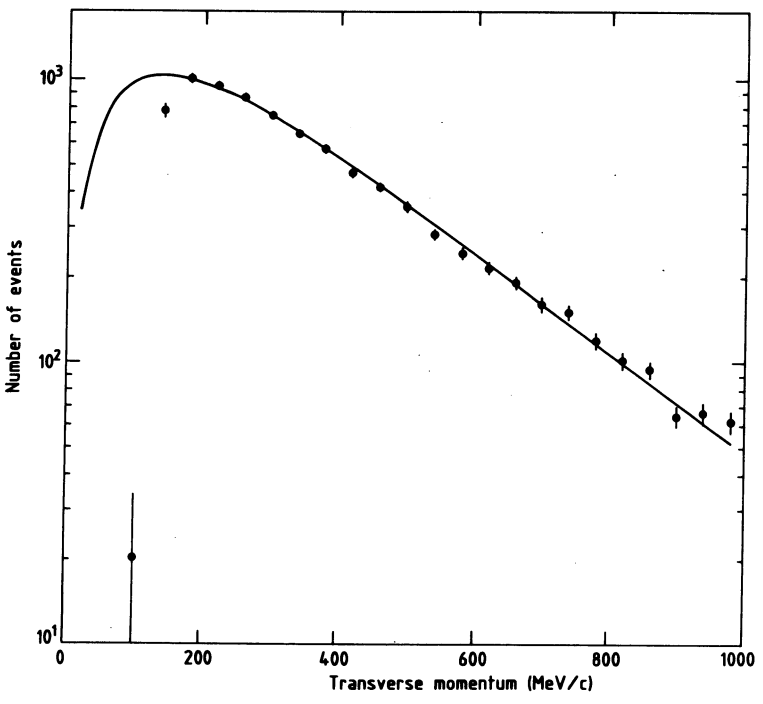

Figure 44: The pion P_T spectrum after corrections.

8. INCLUSIVE η PRODUCTION

It has already been mentioned in section 6.1.3 that the decay of η mesons is one of the largest sources of background in the measurement of single low $-P_T$ positrons and low $-$ mass e^+e^- pairs. However, most previous measurements of the η cross section have been carried out at high P_T. For this reason a measurement was performed of the η/π ratio at low P_T, through the channel $\eta \rightarrow \gamma\gamma$, in order to check the m_T scaling model which was used in the MC calculations.

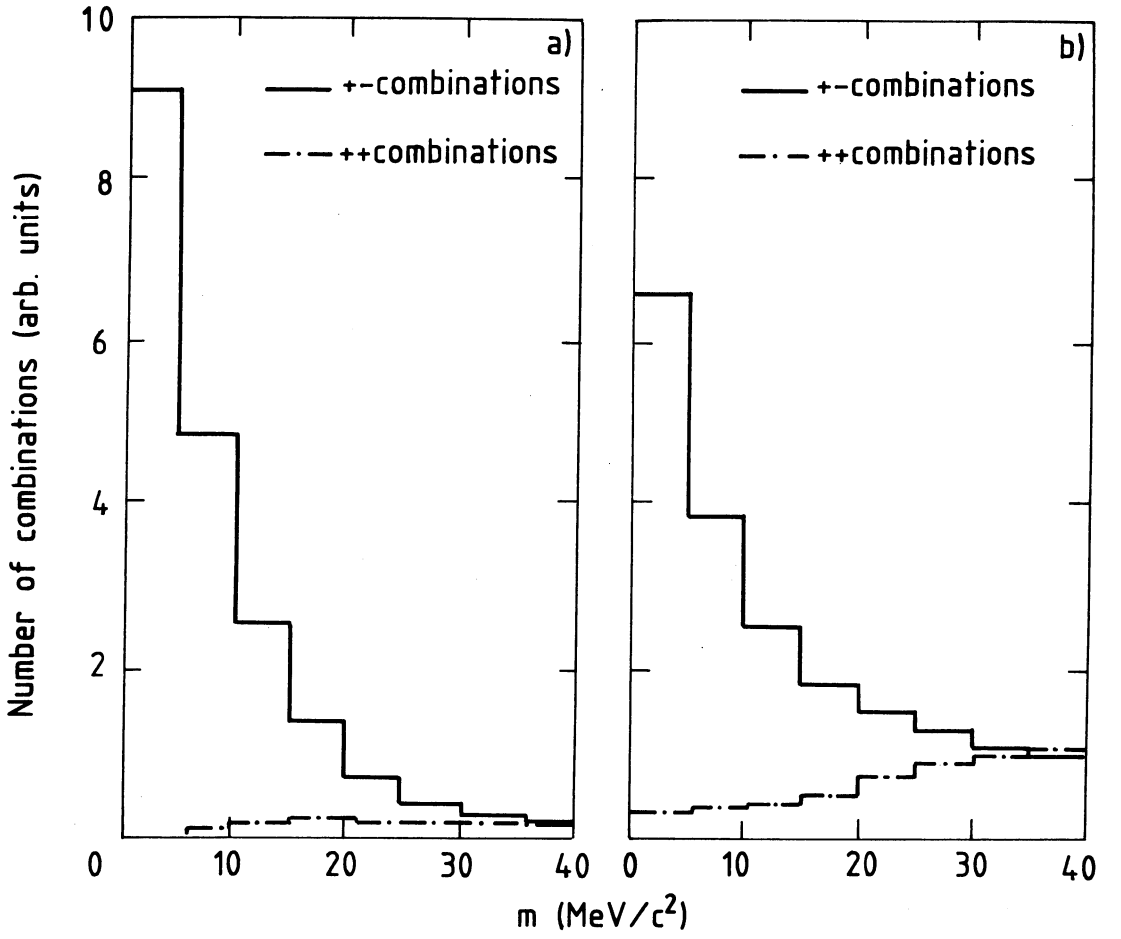

Figure 45: Invariant mass distributions of electron pairs.
A) The pair comes from the triggering γ.
B) The pair comes from the non $-$ triggering γ.

The events that were used in this analysis belonged to the large data sample recorded with the MB trigger and the PT trigger, where an e^+e^- pair from a converted γ had triggered the spectrometer, i.e. those events that were cut away in the normal e/π analysis. The second photon in the decays $\pi^0 \rightarrow \gamma\gamma$ and $\eta \rightarrow \gamma\gamma$ was also found by looking for converted photons (i.e. zero – mass pairs) in the drift chamber.

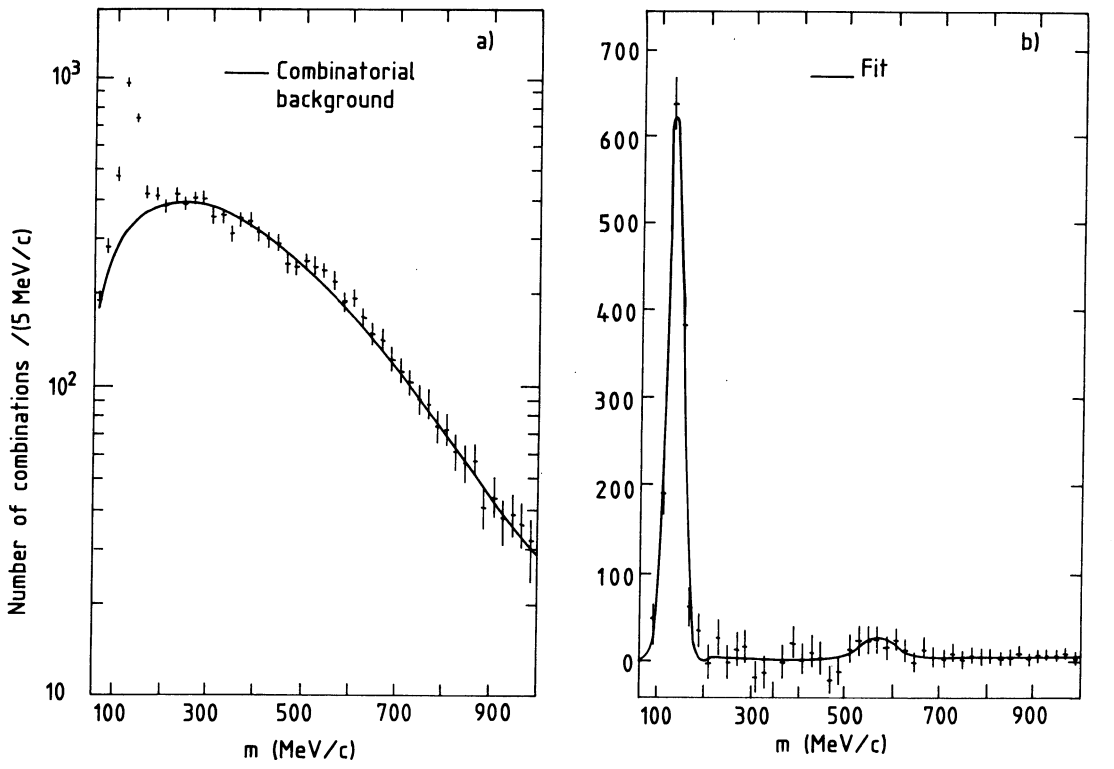

Figure 46: Invariant mass distributions of the two converted photons.
A) Before subtracting combinatorial background.
B) After subtracting combinatorial background.

The same requirement was made on the trigger track as in the standard e/π analysis except for the pair rejection cuts. The following requirements were made in order to find genuine γ conversions:

- a secondary vertex could be reconstructed close to the beam pipe, inner hodoscope or the inner drift chamber wall;
- the opening angle between the particles was small ($<18^0$) and the invariant mass was less than 25 MeV/c^2;
- the reconstructed photon pointed back to the primary vertex;
- the dE/dx information of the second track was consistent with electron identification.

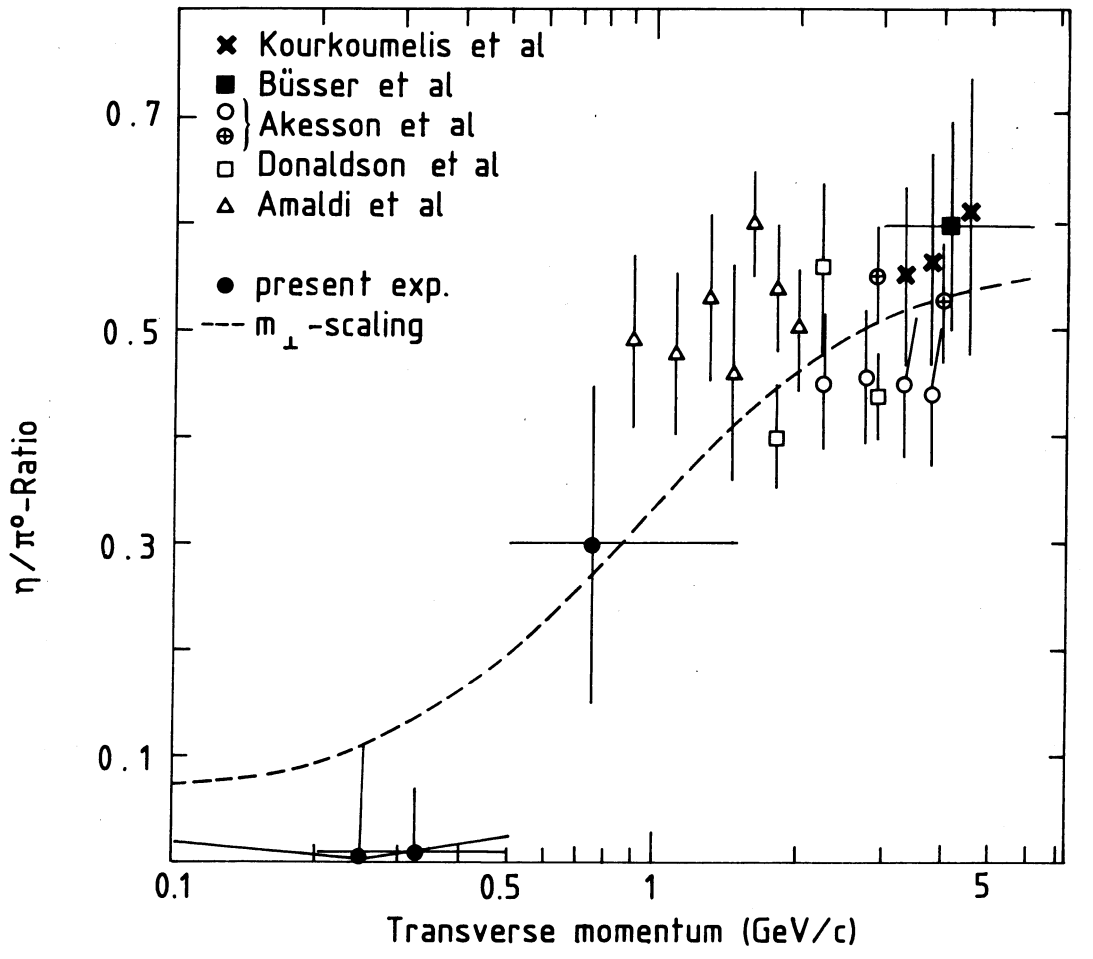

Figure 47: The η/π ratio versus transverse momentum. The dashed line is the prediction from m_T scaling.

In about 10% of the events a second converted γ could be found. The combinatorial background (estimated by like–sign combinations) was somewhat higher ($<10\%$) for the second photon compared to the triggering one ($<1\%$) because of the difference in electron identification (see fig. 45).

The two photon invariant mass distribution for the PT triggered data is shown in fig. 46 a, restricting the $\gamma\gamma$ system to $|y|<0.6$ and $P_T=0.2-1.5$ GeV/c. The combinatorial background (drawn as a full line in fig. 46 a) was calculated by mixing events and the remaining mass distribution after background subtraction is shown in fig. 46 b. A clear π^0 peak can be seen and in the mass region of the η, a small excess of data over background is found at a 3σ level.

When calculating the η/π ratio where both mesons are decaying into $\gamma\gamma$ most systematic uncertainties cancel. The remaining corrections due to reconstruction efficiency and different Q values for the π and η decays were calculated with Monte Carlo. The systematic uncertainty in the final η/π ratio was estimated to be negligible compared to the statistical errors.

The result of the measurement of the η/π ratio (divided into two P_T bins) is presented in fig. 47 and table 12 . Figure 47 also shows the result of another independent low–P_T measurement carried out with the AFS. In this second measurement [61] (which will not be described here) only an upper limit ($\eta/\pi<0.22$ 2σ) was obtained. A compilation of high–P_T measurements done in other experiments is also presented in fig. 47 together with the m_T scaling expectation (the dashed line). It is clear from the new results presented here that the η/π ratio decreases with decreasing P_T as expected from m_T scaling. This experimental verification of the m_T scaling prediction significantly reduced the systematic error in the MC calculation of the remaining background.

Table 12: The η/π ratio versus P_T.

P_T (MeV/c)	η/π
200 – 500	0.01 ± 0.06
500 – 1500	0.30 ± 0.15

9. SINGLE POSITRONS

9.1 INCLUSIVE PRODUCTION OF SINGLE POSITRONS

The measured ratio of the inclusive positron – to – pion cross section at y = 0 is plotted in fig. 48 for a subsample of the available data, triggered by the MB trigger. The $\pi = (\pi^+ + \pi^-)/2$ distribution was corrected as described in chapter 7. Owing to strongly increasing energy losses and decay losses at low P_T, it was not possible to measure the pion yield accurately at $P_T < 0.2$ GeV/c. The three lowest data points in fig. 48 were therefore calculated using a parameterization of the pion spectrum given in [70]. This parameterization showed good agreement with the measurement of this experiment at $P_T > 0.2$ GeV/c, as can be seen in fig. 44 .

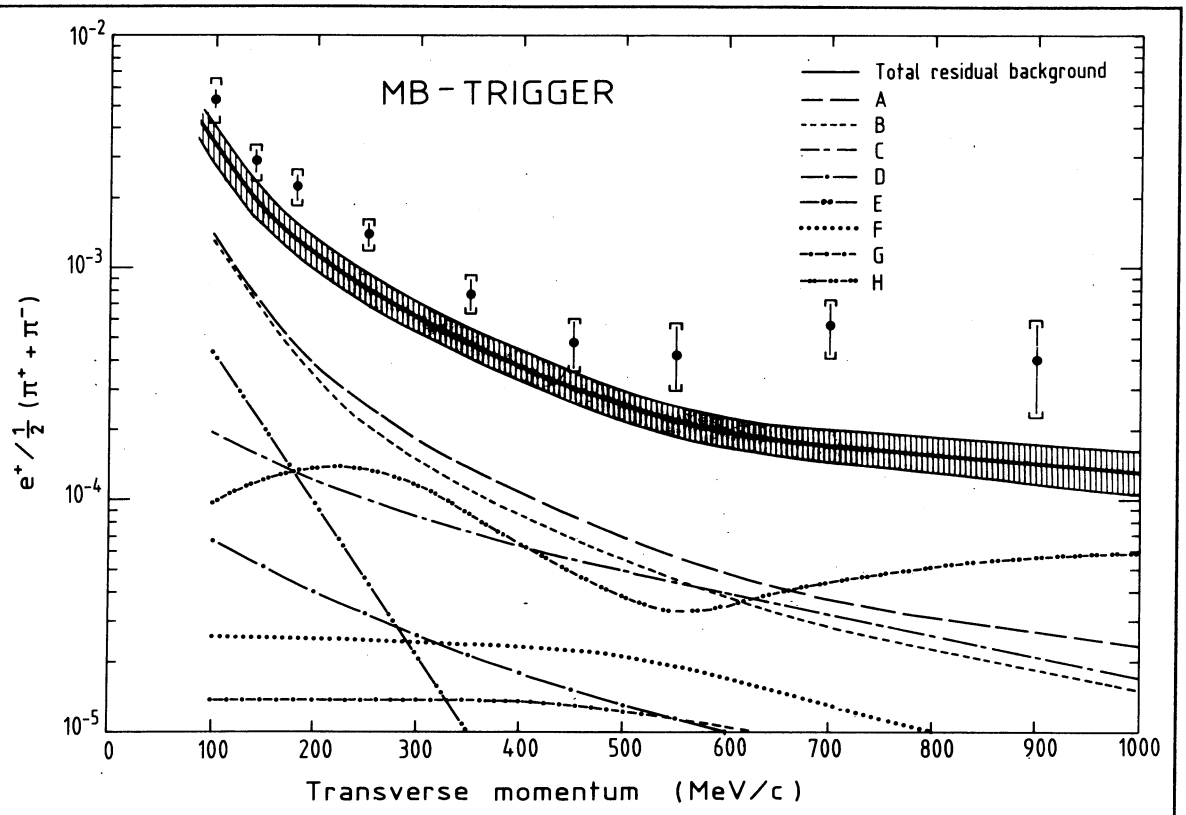

Figure 48: The measured e/π distribution after efficiency corrections (MB triggered data only).

A: π^0 γ conversions
B: π^0 Dalitz decay
C: η^0 Dalitz decay
D: η^0 γ conversions
E: $\eta^0 \rightarrow \pi^0\pi^0\pi^0$ Dalitz + γ conv.
F: η' Dalitz + γ conv.
G: ω^0 Dalitz + γ conv.
H: K_{e3} decay

The e^+ spectrum was corrected for the efficiency of the mass cut (which was not imposed on the π triggers) and for the efficiency of the different hadron rejection cuts. Other cut efficiencies were assumed to be the same for positrons and pions. The Monte Carlo calculation of the residual background from γ conversions, Dalitz decays and Ke_3 decays is also included in fig. 48 . Clearly, an excess of positrons exists above the systematic uncertainties in the Monte Carlo simulation of the residual background. In table 13 the e^+/π ratio is presented, before and after the background subtraction, for the full event sample (MB + PT triggered data). Figure 49 shows the remaining e^+/π ratio measured in this and in other ISR experiments. In the region of overlap, the new results are consistent with previous measurements. However, the data extends to lower P_T values than what was previously achieved. The continuous rise of the e/π ratio is not only confirmed but is seen to continue to a level of $\sim 1.6 \cdot 10^{-3}$ at $P_T = 0.1$ Gev/c.

Table 13: The e^+/π ratio ($\cdot 10^4$).

	MB trigger		PT trigger		Weighted average
P_T bin	**e/π**	**e/π_r**	**e/π**	**e/π_r**	**e/π_r**
80 – 120	53.49	15.93±5.17	46.88	7.43±6.00[1]	15.93±5.17±12.37[2]
120 – 160	28.78	8.78±3.30	28.20	7.21±2.73[1]	8.78±3.30 ±5.43[2]
160 – 200	22.36	9.74±2.82	23.65	10.40±1.68[1]	9.74±2.82 ±3.38[2]
200 – 300	13.93	6.00±1.53	12.96	4.56±0.72	4.82±0.65 ±1.89[2]
300 – 400	7.81	2.86±1.21	6.67	1.43±0.48	1.62±0.45 ±1.03[2]
400 – 500	4.82	1.53±1.10	4.97	1.50±0.47	1.50±0.43 ±0.70[2]
500 – 600	4.32	1.84±1.27	5.02	2.41±0.60	2.31±0.54 ±0.63[2]
600 – 800	5.72	3.76±1.39	5.07	3.00±0.56	3.11±0.52 ±0.66[2]
800 – 1000	4.05	2.25±1.68	4.96	3.07±0.79	2.92±0.71 ±0.66[2]

[1] these values were not used in the weighted average since the trigger efficiency in this P_T range was less than 50%.
[2] both statistical and systematic errors are given.

P_T	The transverse momentum in MeV/c.
e/π	The measured efficiency corrected positron – to – pion ratio.
e/π_r	The residual e/π ratio after background subtraction.

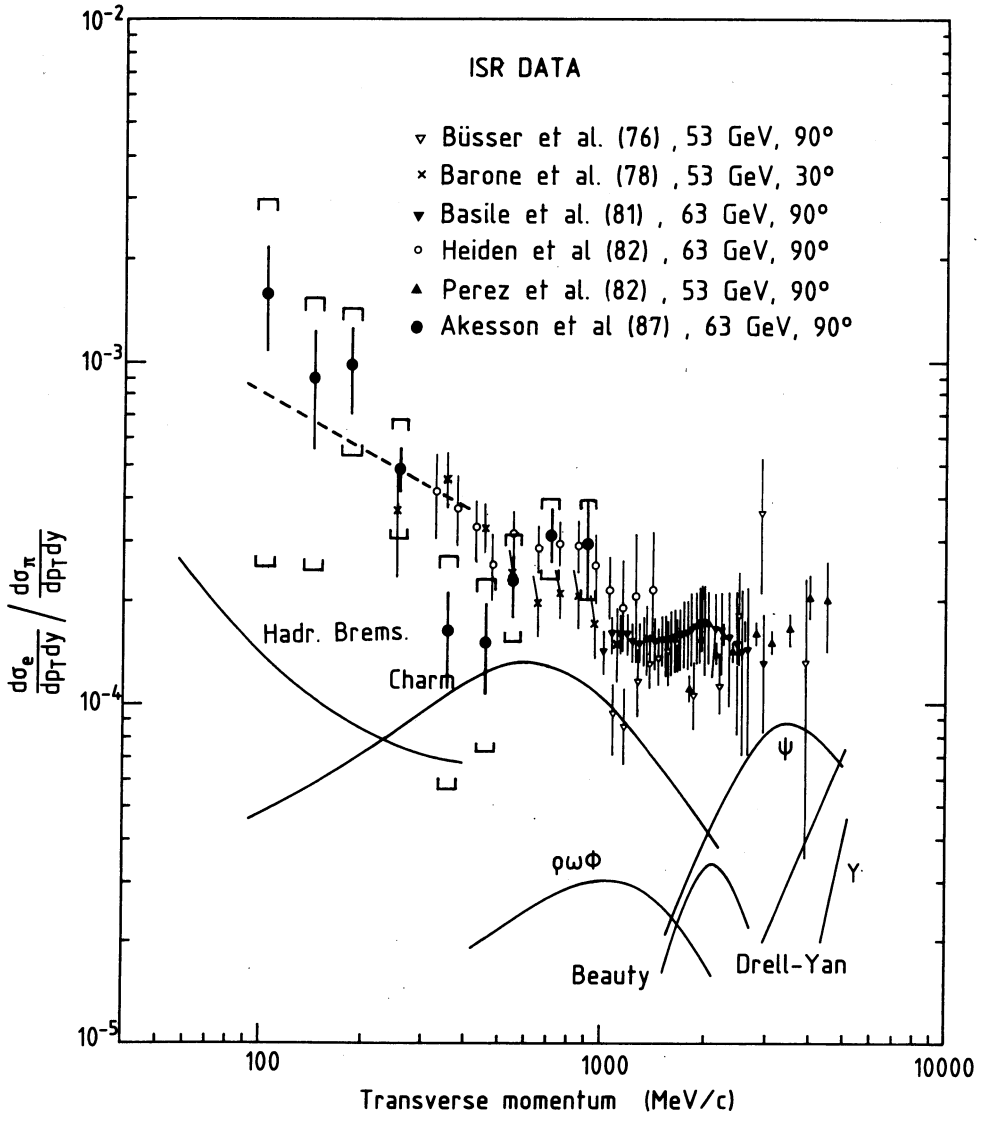

Figure 49: The final e/π distribution.

In order to be able to compare the results of the measurement of the inclusive single positrons with the measurement of e^+e^- pairs, a model for the signal had to be assumed. In the simplest model, the measured signal was compared with the calculated contribution of positrons from η Dalitz decay. The dashed line in figure 42 is the e/π ratio from all known processes (i.e. charm and bremsstrahlung) with an extra contribution of three times η Dalitz decay. This very simple model of the sig-

nal does not fully reproduce the rapid rise of the e/π ratio at the lowest P_T but it can quantitatively reproduce the signal for $P_T > 200$ MeV/c. This will be discussed further in chapter 10 where the signal in the pair measurement will also be compared to the expected number of pairs from three times η Dalitz decay.

9.2 THE MULTIPLICITY DEPENDENCE

The total energy (E_{tot}) in the calorimeter was calculated by summing up all showers with an energy > 0.05 GeV/c, disregarding the showers in the retracted wall. It should be stressed that the term "E_{tot}" in this experiment means the total energy measured by three of the calorimeter walls. Since the calorimeter covered only the central rapidity region, E_{tot} was essentially proportional to the transverse energy density (dE_T/dy). In fig. 50 the distribution of E_{tot} for the final single positron sample is depicted. The ETOT triggered data is shown as a dashed line in fig. 50 and it is clear that, although the E_{tot} data is only a small part of the total data, it dominates the tail towards high total energy.

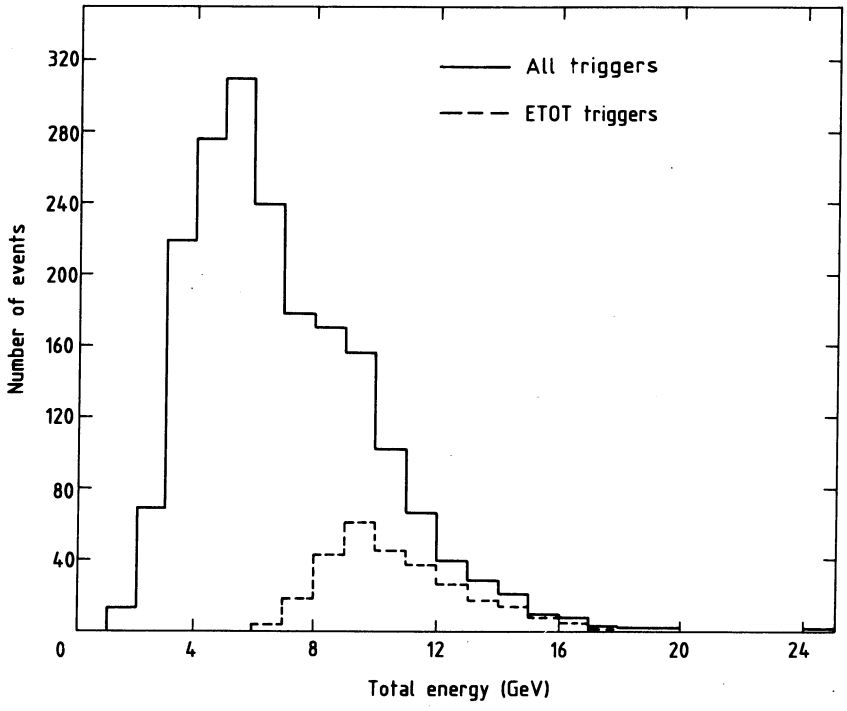

Figure 50: The E_{tot} distribution.

The event sample was divided into four E_{tot} bins and the mean charged multiplicity (including the trigger track) in the rapidity region $|y| < 1$ was calculated. Fig. 51 shows the multiplicity distributions for the four different E_{tot} bins. The efficiency and acceptance corrected mean multiplicity was a factor of 1.2 higher than the measured multiplicity, according to Monte Carlo calculations.

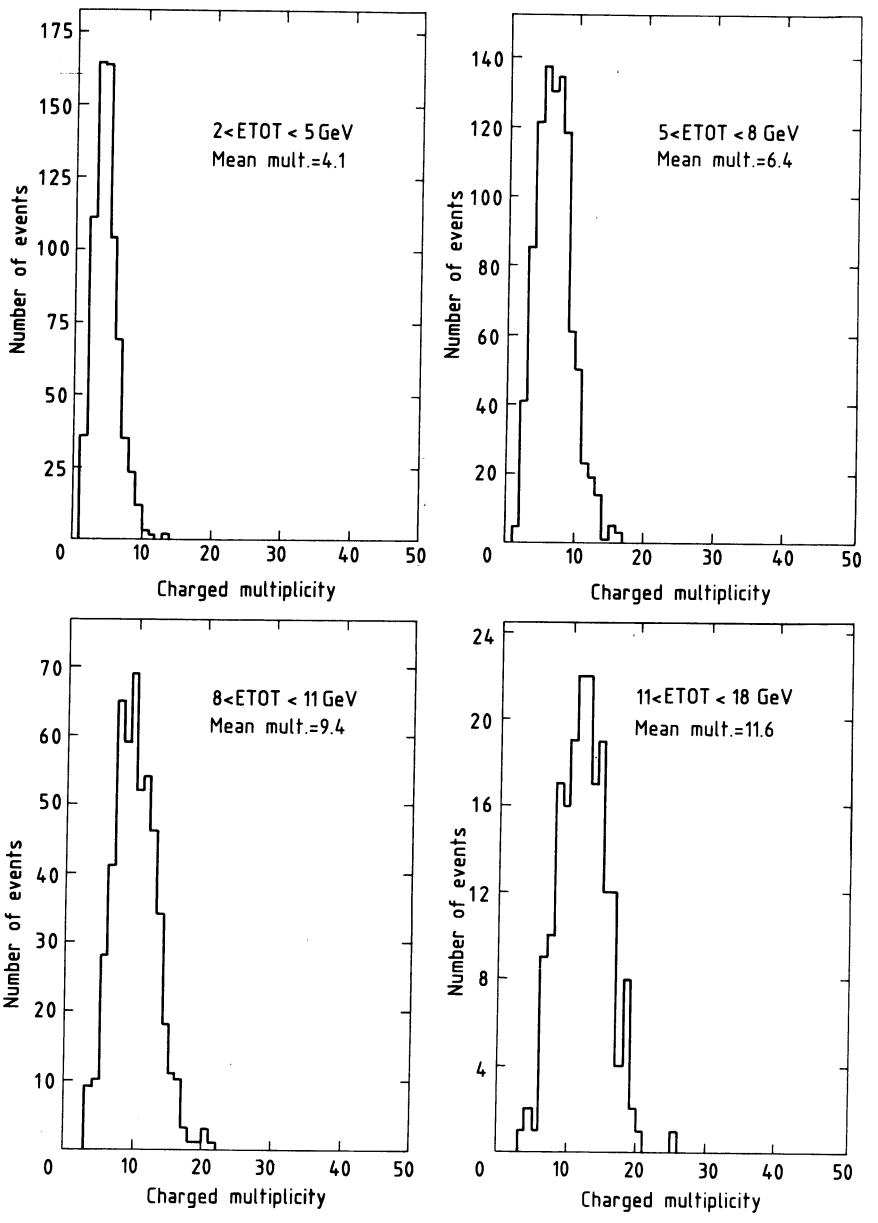

Figure 51: The multiplicity distributions for the four E_{tot} bins.

It is well known that in minimum bias events the mean charged multiplicity (in the central rapidity region) is proportional to the transverse energy (E_T) [110] – [112]. However, this is not the case in high E_T events where jet production starts to be significant. For this reason, the ETOT trigger in this experiment had a threshold energy that was only slightly higher than the E_{tot} in minimum bias events. Table 14 and figure 52 show the correlation between E_{tot} and mean charged multiplicity in this experiment. From figure 52 it is evident that there exists a perfect linear relationship between E_{tot} and multiplicity for the three lowest E_{tot} bins. The highest E_{tot} bin, however, is 9% lower than the line fitted to the three lowest measurements. Judging by previous experiments one would expect a discrepancy from a linear dependence of about 3 – 4% [111] – [112] which indicates that the calculation of the track finding efficiency is ~5% too low at high E_{tot}. In any case, the difference in the highest E_{tot} bin, between the measured value and what would be expected from a linear relationship, is so small that it introduces a negligible systematic uncertainty.

Table 14: The total energy and the corresponding charged multiplicity.

E_{tot} bin	$<E_{tot}>$	$<n>$
2 – 5	3.98	4.98±0.09
5 – 8	6.32	7.76±0.11
8 – 11	9.36	11.50±0.17
11 – 18	12.86	14.20±0.31

$<E_{tot}>$ The mean total energy in GeV.
$<n>$ The efficiency corrected mean charged multiplicity.

The division into E_{tot} bins rather than into multiplicity bins was necessary in order to avoid a trivial distortion of the measured e/π ratio versus multiplicity. If the trigger positrons originated from a pair source, the multiplicity distribution for these events, compared with the distribution from pion triggered events, was shifted to higher values due to the second electron in the pair. This form of trigger bias would give an artificial increase in the e/π ratio with increasing multiplicity but it could be avoided by using E_{tot} rather than multiplicity bins.

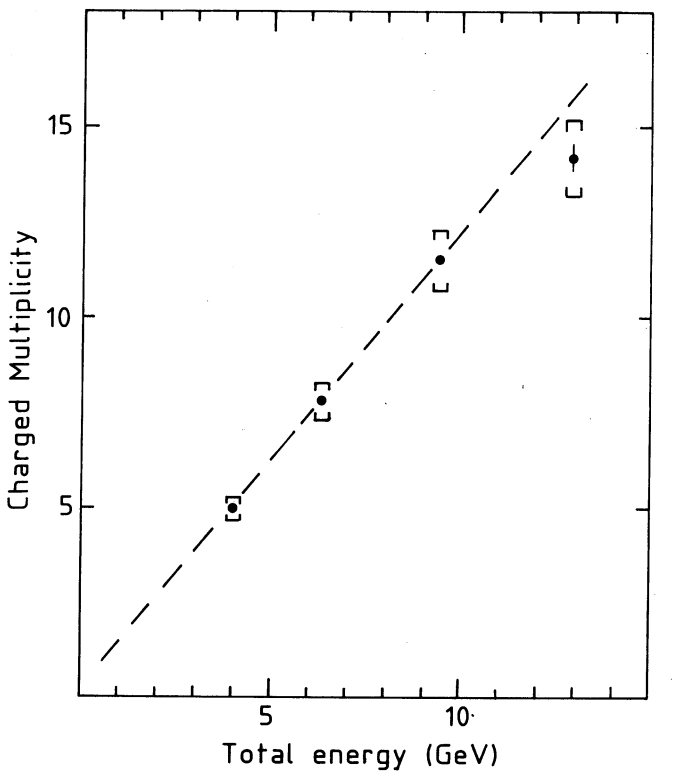

Figure 52: The multiplicity as a function of total energy.

In the final analysis it was required that the electron trigger track did not combine with any track of opposite sign to form a pair with an invariant mass <0.1 GeV/c^2. The efficiency of this cut was strongly dependent on the multiplicity, and therefore this efficiency had to be calculated separately for each E_{tot} bin (see fig. 53). This was the only efficiency correction that was different for different E_{tot} bins since all other cut efficiencies were either independent of E_{tot} or were the same for electrons and pions.

The residual background from γ conversions and Dalitz decays was calculated with the Monte Carlo simulation program described in chapter 6 and subtracted from the measured e/π. By doing this it was assumed that the residual e/π background was independent of E_{tot} as confirmed below.

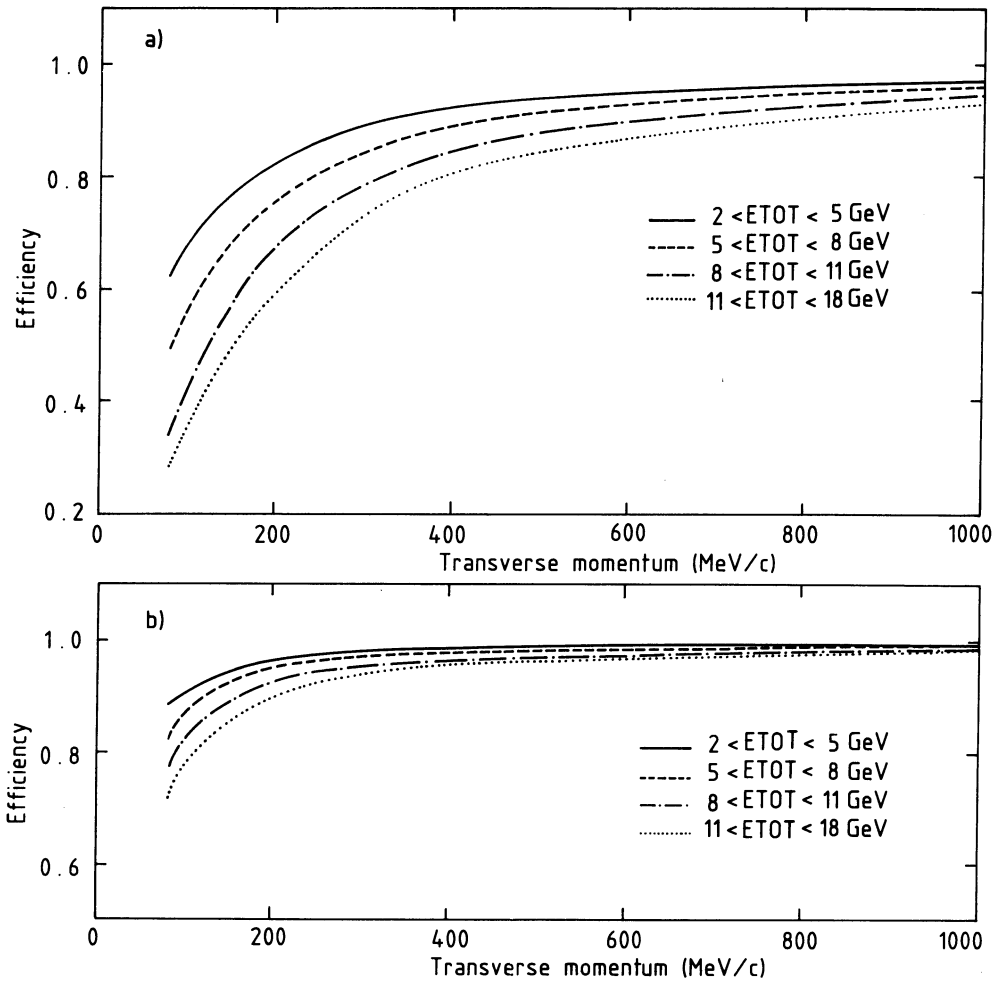

Figure 53: The efficiency for a mass cut at a) 100 MeV/c^2 and b) 50 MeV/c^2.

The event sample in each E_{tot} bin was subdivided into three P_T bins. Fig. 54 shows the e^+/π ratio after background subtraction and efficiency corrections versus mean E_{tot} for the three different bins. A striking difference is observed for the E_{tot} dependence of the e/π ratio in the different P_T intervals. In the highest P_T region there seems to be no significant rise of the e/π ratio as E_{tot} increases, while the confidence levels for a constant value of e/π in the two lowest P_T bins are only 5% and 2% and with the two bins combined the CL is as low as 0.7%. The lines in fig 54 show linear least square fits to the data with the resulting parameters given in table 15 .

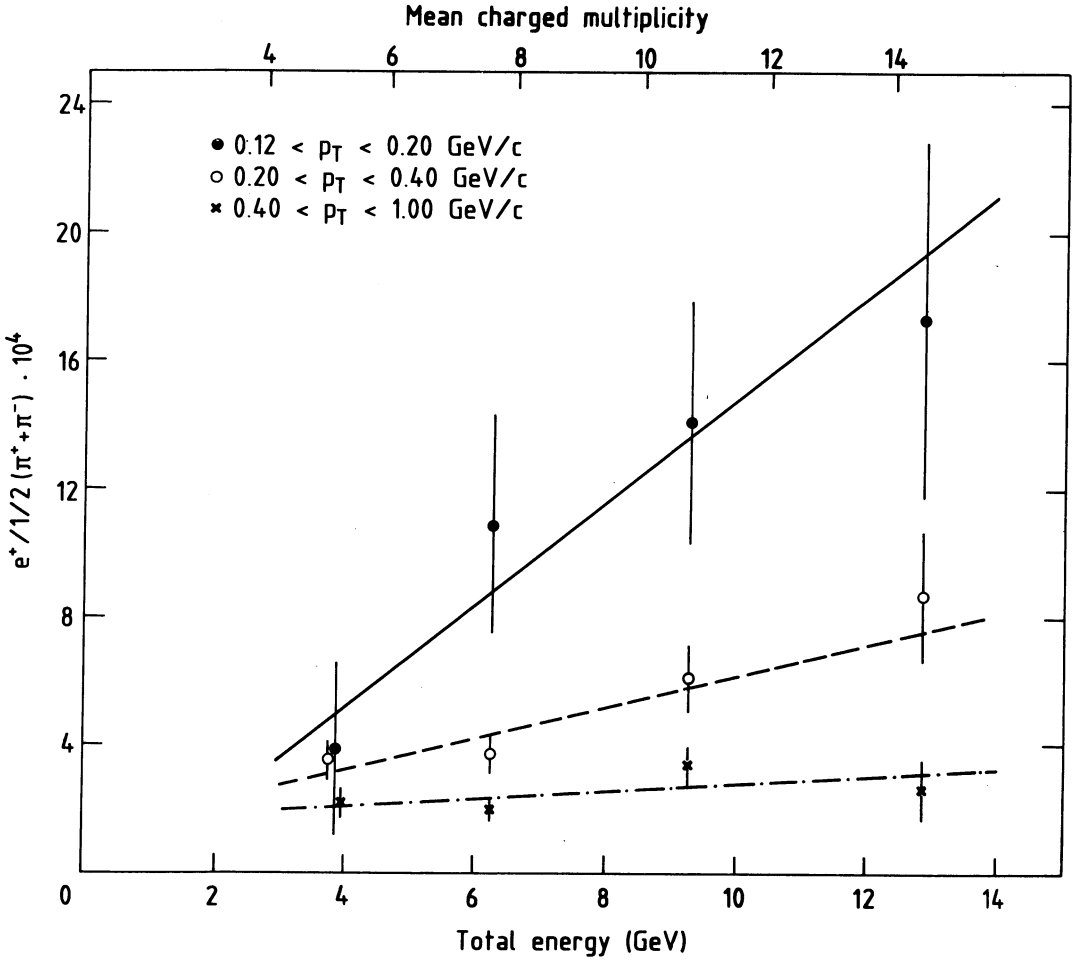

Figure 54: The residual e^+/π ratio as a function of E_{tot}. The top scale indicates the mean charged multiplicity.

Table 15: Fit to the function $e/\pi = (A + B \cdot E_{tot}) \cdot 10^{-4}$

P_T (MeV/c)	A	B	χ^2	NDF
120 – 200	-1.7 ± 4.3	1.6 ± 0.6	0.70	2
200 – 400	1.2 ± 1.1	0.50 ± 0.18	1.78	2
400 – 1000	1.6 ± 0.7	0.12 ± 0.10	2.31	2

The results in fig. 54 are the weighted average of data taken with the three different electron triggers. As can be seen in table 16 , all three data samples were consistent and showed the same increase of the e^+/π ratio with E_{tot} at low P_T. From this it was concluded that there was no large trigger bias.

Table 16: The residual e^+/π ratio $\cdot 10^4$ for different E_{tot} bins.

		MB trig.	PT trig.	ETOT trig.	Weighted average
E_{tot}	P_T	e/π	e/π	e/π	e/π
2 – 5	120 – 200	3.84±2.70	3.65±2.12[1]	–	3.84±2.70
5 – 8	120 – 200	10.85±3.37	10.96±2.27[1]	–	10.85±3.37
8 – 11	120 – 200	8.77±6.49	14.91±4.33[1]	16.75±4.64	14.05±3.77
11 – 18	120 – 200	–	25.63±11.44[1]	17.27±5.54	17.27±5.54
2 – 5	200 – 400	3.40±1.29	3.59±0.76	–	3.54±0.65
5 – 8	200 – 400	5.15±1.57	3.51±0.62	–	3.73±0.58
8 – 11	200 – 400	8.23±3.49	5.07±1.28	8.07±2.11	6.09±1.04
11 – 18	200 – 400	–	10.58±3.69	7.82±2.50	8.69±2.07
2 – 5	400 – 1000	1.74±0.93	2.35±0.49	–	2.22±0.43
5 – 8	400 – 1000	1.33±0.87	2.16±0.41	–	2.01±0.37
8 – 11	400 – 1000	10.73±3.17	3.44±0.78	2.34±1.11	3.37±0.63
11 – 18	400 – 1000	–	2.78±1.47	2.61±1.21	2.68±0.93

[1] these values were not used in the weighted average since the trigger efficiency in this P_T range was less than 50%

E_{tot} The total energy in GeV.
P_T The transverse momentum in MeV/c.
e/π The residual e/π ratio after background subtraction.

Since the result depends strongly on the efficiency corrections for the mass cut, the analysis was repeated with a mass cut at 0.05 GeV/c^2. With this mass cut the efficiency corrections were much smaller (see fig. 53) but the trivial background that

had to be subtracted was a factor of two higher. The same strong E_{tot} dependence was observed as with the higher mass cut at 0.1 GeV/c² (see fig. 55), and from this it was concluded that there was not a large systematic error in the efficiency calculations which could produce the observed increase of the e/π ratio with increasing multiplicity.

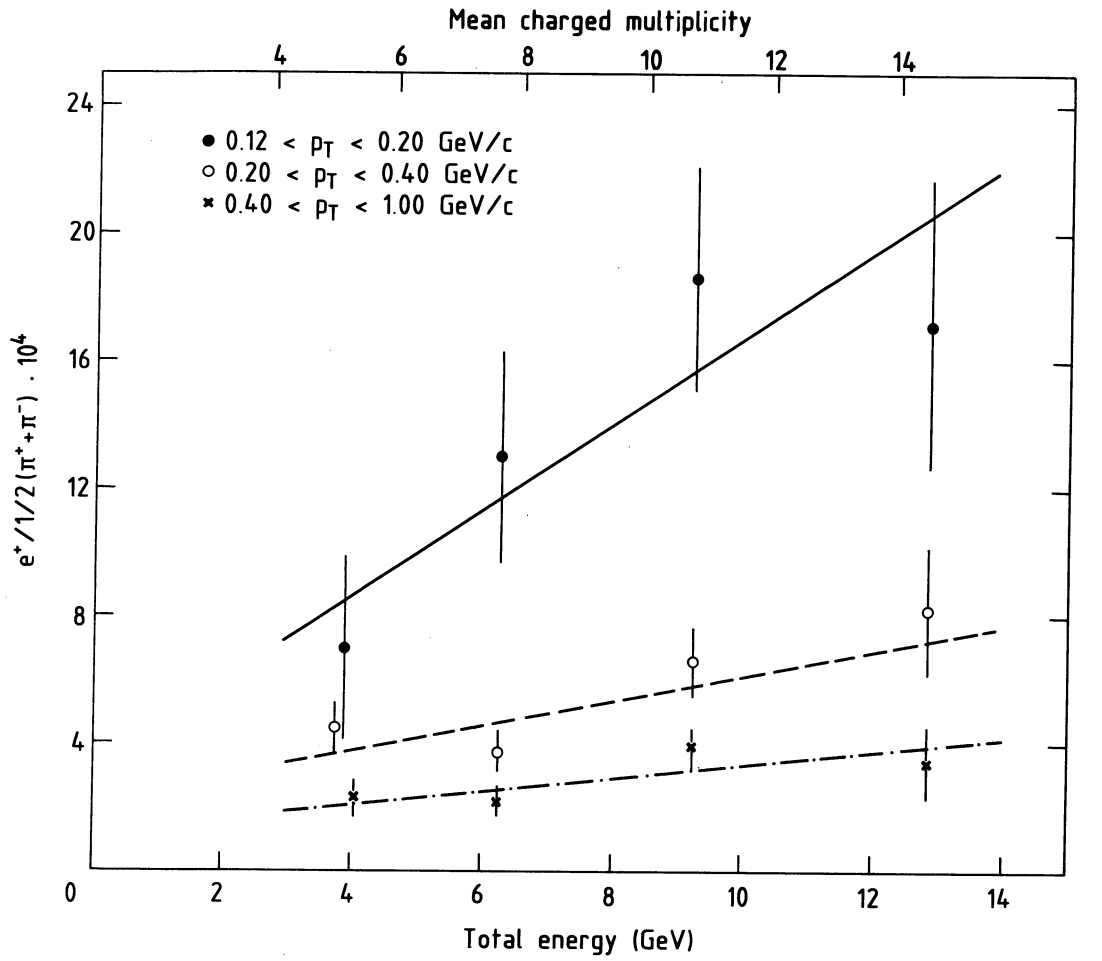

Figure 55: The e/π ratio versus E_{tot} calculated with a lower mass cut.

The rise of the e/π ratio with increasing associated multiplicity could be due to an increase in the production of positrons but it could also be due to a change of the shape of the pion P_T spectrum. For this reason, the pion spectrum for the four dif-

ferent E_{tot} bins was compared. No statistically significant difference was observed between the shape of the pion spectrum in the low E_{tot} sample compared with that of the high E_{tot} sample. The SFM experiment has made a similar measurement but with smaller statistical errors and over a larger P_T range [111]. The P_T distribution of charged particles produced in high multiplicity events was, in this experiment, compared with the distribution in low multiplicity events and a difference was observed at $P_T > 700$ MeV/c. However, the P_T range of interest to the AFS experiment is 120 – 400 MeV/c and in this region the fraction of charged particles was almost identical in high and low multiplicity data.

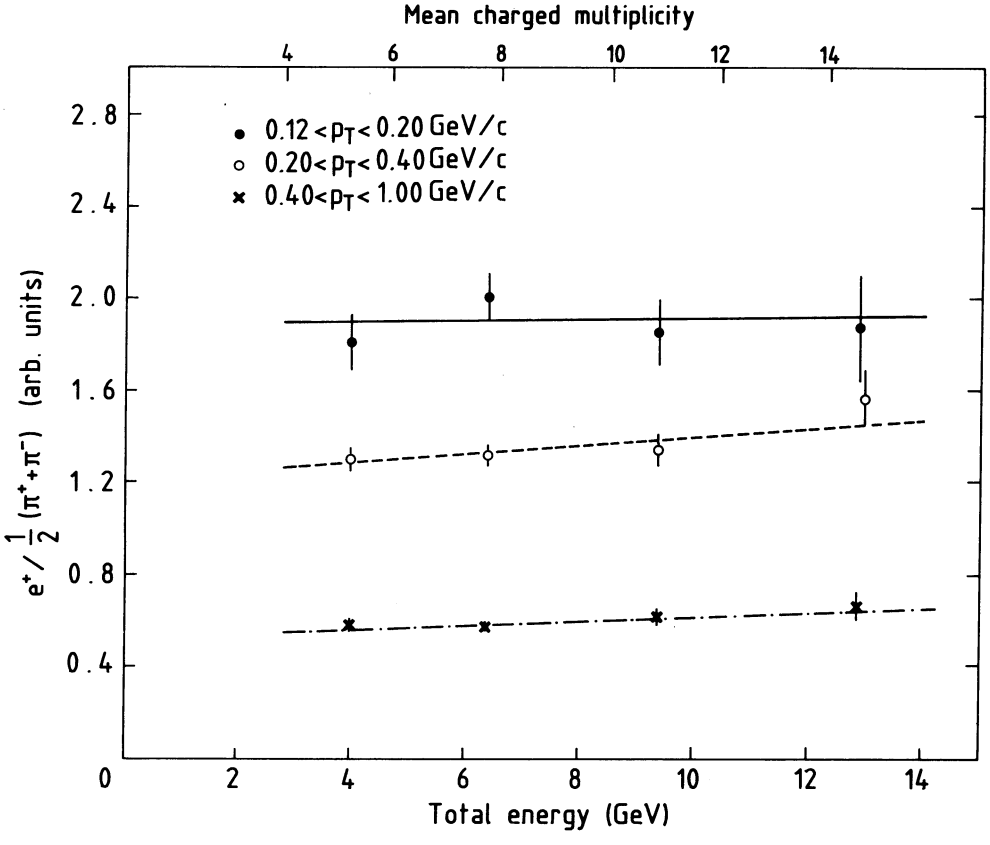

Figure 56: The e/π ratio versus E_{tot} when the e originates from a real photon.

Finally, the same analysis was done with zero – mass electron pairs that were originating from photons converting before the drift chamber. This measurement of

e/π is presented in figure 56 . In this case the e/π ratio at low P_T is constant. The result of this measurement showed that the division of the sample into E_{tot} bins did not introduce a biased selection and that the background from photons relative to the number of pions did not increase strongly with multiplicity. This is important, since it indicates that the assumption, that the background from trivial sources is independent of the multiplicity, was correct.

9.3 DISCUSSION OF SYSTEMATIC ERRORS

Appendix B describes how the statistical and systematic errors were calculated and propagated in this experiment. In this section, the individual systematic uncertainties in the e/π analysis, will be discussed.

The different systematic errors in the calculation of the efficiency corrected e/π ratio is given in table 17 . For the PT triggered data, the correction for the PT trigger efficiency was so large at low P_T that even a small systematic error in the efficiency correction gave a large error in the final e/π. It was for this reason that the PT triggered data with a P_T less than 200 MeV/c was disregarded. At low P_T the MB and ETOT triggered data had the largest systematic uncertainties due to the large efficiency correction for the mass cut and because of the pion normalization which was done with a parameterization at low P_T. At higher P_T (> 200 MeV/c) the systematic error was dominated by the uncertainties in the efficiency correction for the hadron rejection cuts. In this P_T region the systematic error was approximately the same for MB, PT and ETOT triggered data.

Section 6.5 describes some of the tests that were made in the MC in order to estimate the systematic uncertainty in the calculation of the remaining electron background. The systematic error in the parent production depends on how well the pions and η's can be simulated. In the pion case, there exists accurate measurements down to 40 MeV/c which can be used. Different parameterizations were tried in the MC calculations in order to estimate the sensitivity of the results to this part of the MC analysis. The η/π ratio was measured in this experiment and this greatly reduced the systematic error in the calculation of the background from η decays. The uncertainty in the calculation of γ conversions was dominated by the precision with which the amount of material between the vertex and the drift chamber was known. After the ISR had been closed down, the IH counters were removed and dismantled so that the precise amount of material in the small region, which the trigger particles passed through, could be measured accurately. It is believed that the uncertainty in the estimation of the total amount of material between the vertex and the drift chamber is less than 10%, which gives an error of $\sim$5% in the MC calculation, since about half of the background originates from γ conversions.

It has been discussed in section 5.1 how the background could be treated differently depending on whether the second electron in a pair reached the drift chamber or not. The major part of the remaining background consisted of pairs where one of

the electrons did not reach the DC and the fraction of these events in the final event sample could be estimated accurately since it depended only on geometrical acceptance, energy loss and multiple scattering. The difficult part of the MC simulation was to calculate the rejection of pairs where the second electron reached the drift chamber. It has been shown in fig. 40 that the mass distribution generated with the MC was in good agreement with the same distribution from the data, i.e. the rejection of reconstructed pairs was quite well simulated by the MC. The rejection of unreconstructed pairs relied mostly on the requirement imposed on the unassigned digitizings. The distributions of unassigned digitizings had the same shape in the data and the MC but there was a higher background level of digitizings in the data due to other tracks than from the trigger pair. This was understandable as only two tracks were generated in the MC while a typical real event had on average 6 charged tracks. This discrepancy between data and MC resulted in a somewhat higher rejection from the cut on unassigned digitizings in the data analysis compared to what was estimated in the MC calculation.

By changing the parameterized rejection function (fig. 34) in the "geometrical" MC the effect of an error in the rejection of pairs in the MC could be estimated. A maximum error of 50% in the rejection of true pairs that had reached the drift chamber was assumed, this gave an error that was less than 15% in the overall MC calculation of the remaining electron background.

In the P_T range above 1 GeV/c, the systematic error in the final e/π ratio started to grow rapidly for several reasons. One reason was that the hadron rejection rapidly became worse (see fig. 26). It was estimated that the error on the calculated hadron background was less than 50%. At low and medium P_T the total error was not at all sensitive to this error, however, this was not the case at high P_T where the hadron contamination became significant. Another problem at high P_T was the simulation of the detector response to the pairs that had a sufficiently high momentum so that they did not open up in the magnetic field and therefore were reconstructed as one track. This background was rejected by the dE/dx measurement and by the measurement of the number of Z measurements. The dE/dx, in particular, was poorly simulated in the full drift chamber MC. Finally the Ke_3 decay, where the kaons decayed after the drift chamber, became important at high P_T. The calculation of this background had a larger systematic uncertainty than the MC calculation of the pair background since this simulation relied heavily on the calculated kaon rejection (by dE/dx and TOF) which was used as an input to this MC. For the above reasons (and because of a lack of events) the e/π ratio was not evaluated above a P_T of 1 GeV/c in this experiment which was aimed at measuring low-P_T positrons.

Table 17: Systematic errors

P_T (MeV/c)	H.R	M	P	π	C	NaI	H.C.	MC
80 – 120	8.5%	12%	4%	9%	5%	51.3%	50%	20%
120 – 160	8.5%	8%	4%	7%	4%	25.2%	50%	17%
160 – 200	8.5%	5.5%	4%	5%	2%	12.2%	50%	16%
200 – 300	8.5%	3%	4%	3%	2%	6.9%	50%	15%
300 – 400	8.5%	2%	4%	3%	0%	5.2%	50%	15%
400 – 500	8.5%	2%	4%	3%	0%	4.9%	50%	15%
500 – 600	8.5%	2%	4%	4%	0%	4.6%	50%	15%
600 – 800	8.5%	2%	4%	5%	0%	4.5%	50%	16%
800 – 1000	8.5%	2%	4%	6%	0%	4.4%	50%	18%

H.R.	Error of efficiency corrected e/π due to hadron rejection cuts.
M	Error of efficiency corrected e/π due to mass cut.
P	Error of efficiency corrected e/π due to position match of trigger track and shower in NaI.
π	Error of efficiency corrected e/π due to pion normalization.
C	Error of efficiency corrected e/π due to unknown Cherenkov trigger efficiency.
NaI	Error of efficiency corrected e/π due to NaI trigger efficiency.
H.C.	Error of the estimation of hadron contamination.
MC	Error of Monte Carlo calculated background.

9.4 COMPARISON WITH OTHER EXPERIMENTS

There exist two previous ISR experiments which have studied the production of positrons at a transverse momentum less than 1 GeV/c (see table 18). The first experiment [17] was performed at $\sqrt{s} = 53$ Gev and $\theta_{cm} = 30^0$ and measured positrons in the P_T range 0.2 – 2.0 GeV/c. The second experiment [18] was done at $\sqrt{s} = 63$ GeV and $\theta_{cm} = 90^0$ and the P_T interval for this experiment was 0.3 – 1.5 GeV/c. The results of these two experiments are plotted in fig. 49 . Both experiments observed a rise at low P_T in agreement with this experiment, but the conclusions

Table 18: A compilation of low – P_T l/π experiments.

Colliding beam experiments measuring e/π:

Ref.	Exp. location	B&T	P_b	$\sqrt{s}$	P_T	θ_{cm}
*	AFS at ISR/CERN	pp	31.5	63	80	90°
[17]	at ISR/CERN	pp	26.5	53	200	30°
[18]	SFM at ISR/CERN	pp	31.5	63	300	90°

Fixed target experiments measuring e/π:

Ref.	Exp. location	B&T	P_b	$\sqrt{s}$	P_T	θ_{cm}
[19]	at AGS/BNL	pp,πp	10 – 24	4 – 7	500	90°
[20]	at KEK	pBe	13	5[1]	250	90°
[21]	at ZGS/ANL	pp,pBe	12	5[1]	200	20° – 84°
[22]	BEBC at SPS/CERN	πp	70	12	250[2]	–

Fixed target experiments measuring μ/π:

Ref.	Exp. location	B&T	P_b	$\sqrt{s}$	P_T	θ_{cm}
[23]	at FNAL	pFe	350	24[1]	300[2]	–
[24]	UCCS at FNAL	pFe	200	20[1]	250[2]	–

* this experiment
[1] calculated for pp collisions
[2] the mean value

Ref.	Reference.
Exp.	Experimental.
B&T	Beam and Target.
P_b	The beam momentum in GeV/c.
$\sqrt{s}$	The center of mass energy in GeV.
P_T	The minimum transverse momentum measured in MeV/c.
θ_{cm}	The center of mass angle in relation to the beam.

made by the two experiments were different. The first experiment reported a significant rise at low P_T, which could not be explained by conventional sources, while the second experiment did not rule out charm decay as the explanation for the observed increase of the e/π ratio. The reason for the different conclusions was due to the estimation of the systematic errors. While the first experiment regarded the rise at low P_T as significant, the second experiment assigned very large systematic errors to the results at low P_T mainly because of the uncertainties in the η/π ratio used in the background calculations. Now, since the η/π ratio at low P_T has been measured in this experiment, it is perhaps possible to claim that both previous experiments observed a significant rise above known sources at low P_T.

The fixed target experiments, which have studied low $-P_T$ production of single positrons and electrons, have all been carried out at a $\sqrt{s}$ which is significantly lower than in this experiment. One of these experiments, performed at Brookhaven (at a maximum energy of $\sqrt{s}=7$ GeV, at $\theta cm=90^0$ and with a minimum P_T of 500 MeV/c), reported a rise of the e/π ratio at low P_T which could not be explained by conventional sources. However, this experiment did not include the semileptonic decay of D mesons into its definition of conventional background sources and it is possible that this process contributed in a substantial way to the measured e/π ratio in the P_T region covered by this experiment.

Out of two similar fixed target experiments at $\sqrt{s}=5$ GeV, which have measured positron and electron production down to 200 MeV/c in P_T, one experiment [20] found a rise in the e/π ratio and the other experiment [21] reported no rise at low P_T and no excess of electrons above previously known sources. A bubble chamber experiment performed at BEBC [22] reported no rise at low P_T ($<P_T>=250$ MeV/c) and an e/π ratio, integrated over P_T, of $(1.2\pm0.3)\cdot10^{-4}$.

Finally, two experiments have been carried out at Fermilab [23] [24], which have studied single prompt muons at low P_T. The conclusion from these experiments is that no strong rise in the μ/π ratio at low P_T is observed, however, this is not in contradiction with a rise of the e/π ratio at low P_T provided the electrons originate from low $-$ mass pairs (because of the mass difference between muons and electrons).

It can be concluded that the experimental evidence for a rise of the e/π ratio with decreasing P_T has been somewhat controversial. However, with the new results obtained by this experiment, the excess of low $-P_T$ positrons above known sources has been confirmed. In addition, the excess has been studied at lower P_T values than what was previously achieved.

10. ELECTRON – POSITRON PAIRS

Previous experiments have mostly measured either e^+e^- pairs or the single inclusive e/π ratio and consequently there exists few published results where the rise in the e/π ratio at low P_T has been experimentally connected to the production of low – mass pairs. For this reason, it would be valuable if the measurement of the rise in the e/π ratio carried out by this experiment could be accompanied by a measurement of e^+e^- pairs in the same data. This would perhaps make it possible to determine if the rise in the e/π ratio below a P_T of 1 GeV/c is due to the low – mass e^+e^- continuum with masses < 0.6 GeV/c^2. In order to understand the physical processes, which produce these low – mass pairs, it is of importance to study the dependence of the pair cross section on the associated charged multiplicity. It has already been shown in section 9.2 that the single inclusive positron cross section increases with the square of the charged multiplicity. An important consistency check would be to look for the same multiplicity dependence for pairs.

In order to be able to do a measurement of electron pairs one must find and reconstruct the second electron (the non – trigger electron) in the pair with a reasonable acceptance and, in addition, it was necessary to identify the second electron against a large background of hadrons. This experiment fulfilled the first requirement, but as far as electron identification of the second track was concerned, it was limited to the use of dE/dx in the drift chamber (as described in section 4.1).

10.1 THE COMBINATORIAL BACKGROUND

There are events where the e^+ and e^- originate from different parents or processes, even with a 100% identification of the second electron in the pair. Take for example an event with an e^+ trigger originating from a γ conversion and a second electron somewhere in the event originating from a Compton scattering. The number of these so – called "combinatorial background pairs" will increase if the identification of the second electron is reduced so that random pairs can be formed between the electron trigger and hadrons in the event.

In this experiment, one had the possibility to either limit the momentum range of the second track to 40 – 140 MeV/c which resulted in a good electron identification, or to use the full momentum range with a poor identification. The disadvantage of a lower P_T range was the low acceptance for pairs and a large problem arising from the charge asymmetry introduced by the Compton electrons. This charge asymmetry complicated the calculation of the combinatorial background. The disadvantage with the full momentum range (40 – 1000 MeV/c) was the large combinatorial background due to the poor electron identification. The results presented below are based on an analysis in which the full momentum range of the second track was used but the analysis was also carried out with the lower momentum range as an internal check.

The combinatorial background can be estimated by combining like-sign tracks into pairs (i.e. the combinatorial background = $e^+x^+ + e^-x^-$ where e is the trigger electron and x is the second track in the pair). This method of calculating the combinatorial background is not completely correct since the real background consists of uncorrelated e^+x^- and e^-x^+ combinations. In particular, when using second tracks with low P_T, the charge asymmetry introduced by electrons from Compton scattering gives a large error in this method of calculating the background.

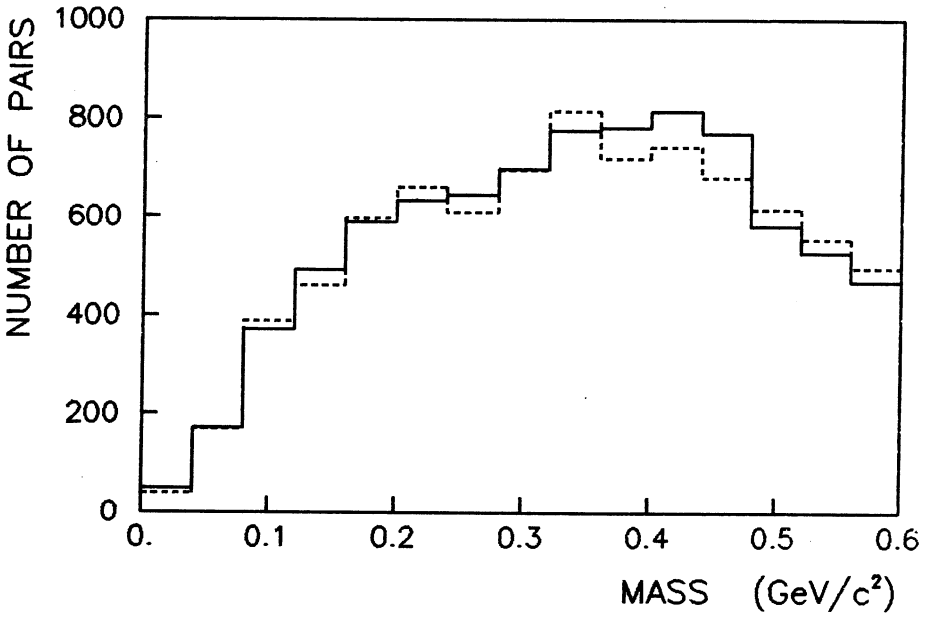

Figure 57: The mass distribution of $e^+x^+ + e^-x^-$ pairs. The full line shows the distribution obtained with the "conversion" sample and the dashed line is the distribution of the "single" sample.

In this experiment the combinatorial background was calculated by using the large sample of triggering zero-mass e^+e^- pairs originating from γ conversions. The following method was used. The P_T spectrum of the triggering electrons in the normal "single" data sample was plotted. The conversion sample was processed through exactly the same analysis program as the normal data sample (except for the mass cut which was removed) and the P_T spectrum for this sample was also plotted. The conversion sample was then used to plot the mass distribution of e^+x^- and e^-x^+ combinations with each event given a weight determined by the ratio of the two P_T spectra from conversions and singles. In this way the P_T spectrum of the

conversion sample was modified in order to correspond to the P_T spectrum of the normal data sample. The weighted e^+x^- and e^-x^+ mass distributions from the conversion sample were used as a measurement of the combinatorial background above a mass of 50 MeV/c^2.

In order to check that this method worked, the mass distribution of $e^+x^+ + e^-x^-$ was plotted, both with this method of using electrons from conversions and by using the normal single data sample (fig. 57). The shape of these distributions was the same within statistical errors and the integrated number of pairs between 0 and 600 MeV/c^2 differed by only 0.6%. The E_{tot} distribution of the data sample from γ conversions and from the single sample was also plotted and found to be identical (fig. 58).

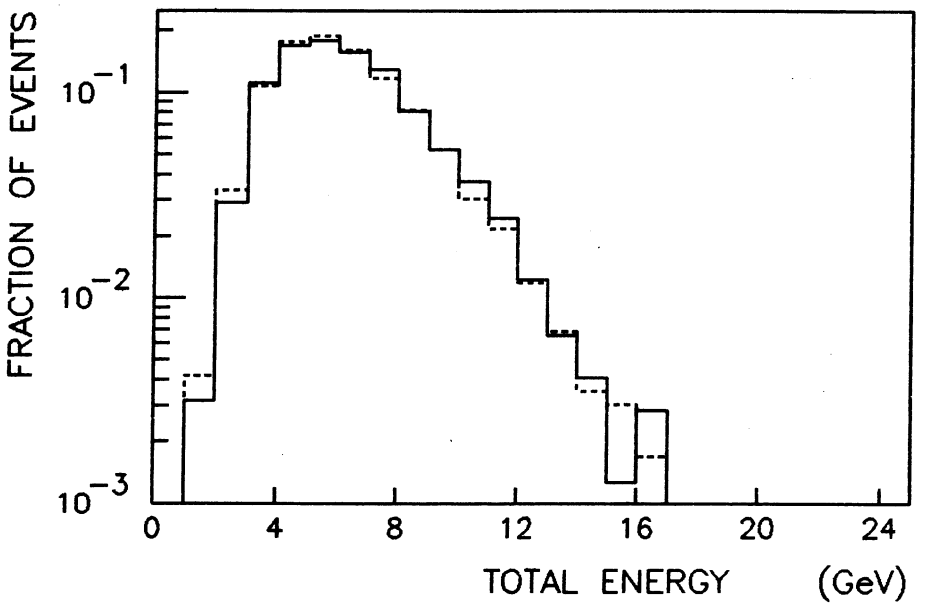

Figure 58: The E_{tot} distribution for the single sample (dashed line) and the conversion sample (full line).

It can be seen from figure 57 that the combinatorial background is smaller at low mass (<100 MeV/c^2) than at high mass. The background at high mass (100–600 MeV/c^2) was studied for three different momentum intervals of the second electron in the pair (see table 19). In the smallest momentum interval, the signal to background ratio was the highest, which is what one would expect since it is only

at low momentum that the dE/dx identification is effective. However, by restricting the second electron to the smallest momentum interval most of the signal would be cut away and the pairs that were left would be very asymmetric (one electron would have low and the other high momentum). For this reason the large momentum range was used and it should be stressed that this resulted in a poor signal to background ratio at $m > 100$ MeV/c^2 which means that the results depend crucially on a correct calculation of the combinatorial background.

Table 19: The signal to combinatorial background ratio (SB) for pairs with $100 < m < 600$ MeV/c^2 as a function of the momentum (P_2) of the second electron in the pair.

P_2 (MeV/c)	SB
40 – 100	0.41
40 – 140	0.21
40 – 1000	0.10

10.2 THE BACKGROUND FROM KNOWN PAIR SOURCES

The calculation of the number of expected pairs from different known sources was made with the same Monte Carlo program that was used in the e/π analysis (see chapter 6). The problem was less complicated in the pair case since the rejection of different types of background from real converted photons was not needed, only the acceptance of high mass (> 50 MeV/c^2) pairs from virtual photons had to be calculated, i.e. mainly the pairs from π^0 Dalitz and η Dalitz decays.

10.3 THE ANALYSIS

The requirements on the trigger track were slightly modified in the pair analysis since the mass cut was changed from 100 MeV/c^2 to 50 MeV/c^2. In order not to cut away low – mass pairs the dE/dx cut (on the upper side of the electron band) was not done if there was a second track in the same DC sector as the trigger track. In the same way, the required number of Z measurements was lowered from 25 to 15 if there was a second track in the same DC sector as the trigger track. Since it was desirable to use the large sample of PT triggered data, a minimum P_T of 200 MeV/c

was required for the trigger electron. Both e^+ and e^- triggered data were used in the pair analysis so that the smallest possible statistical and systematic errors could be achieved. A pulse height cut was made on the inner hodoscope signals (if the trigger particle was an e^-) as described in section 5.2.2 . This reduced the combinatorial background caused by Compton scattering.

The quality requirements on the second track in the pair were the following: a minimum number of Z measurements (10), a minimum track length (15 cm), a minimum momentum (40 MeV/c) and an extrapolated vertex position close to the primary vertex. The same dE/dx cut on the lower side of the electron band was made as for the trigger track but the upper dE/dx cut was made only if the second track was isolated in its DC sector.

10.4 THE RESULTS

Figure 59 a shows the mass distribution of unlike–sign pairs and the calculated combinatorial background. At low mass (50 – 100 MeV/c^2), the number of unlike–sign pairs rises dramatically due to the background from π^0 Dalitz decays, while at higher masses the main source of background originates from the combinatorial pairs. It is clear from fig. 59 a that this analysis suffers from a low signal to background ratio and that the results rely heavily on the systematic uncertainties in the estimation of the background. However, the background at low mass (<100 MeV/c^2) and the background at high mass (>100 MeV/c^2) are of completely different origin and the background calculation should therefore be dominated by different systematic problems in different mass intervals.

In fig. 59 b, the mass distribution for pairs after subtracting the combinatorial background is depicted. The expected mass distributions from known pair sources calculated by MC, and normalized to the integrated $(\pi^+ + \pi^-)/2$ spectrum[2] at $y=0$, are also shown. A signal above the MC calculation of the contribution from known sources can be seen in the whole mass range of this experiment. The distribution in fig. 59 c shows what remains after subtracting the known sources calculated by the MC. The signal is statistically significant both at low mass (50 – 100 MeV/c^2) and at high mass (100 – 600 MeV/c^2).

The mass spectrum in fig. 59 c is not acceptance corrected. For comparison, the mass distribution of three times the η Dalitz contribution has been plotted as a dashed line. The signal seems to be somewhat flatter than pairs from η Dalitz but a firm conclusion about the shape cannot be drawn with the limited statistics available and the large systematic uncertainty due to the background subtraction.

---

[2] The cross section of the $(\pi^+ + \pi^-)/2$ spectrum from [70] integrated over P_T at $y=0$ is 31 mb.

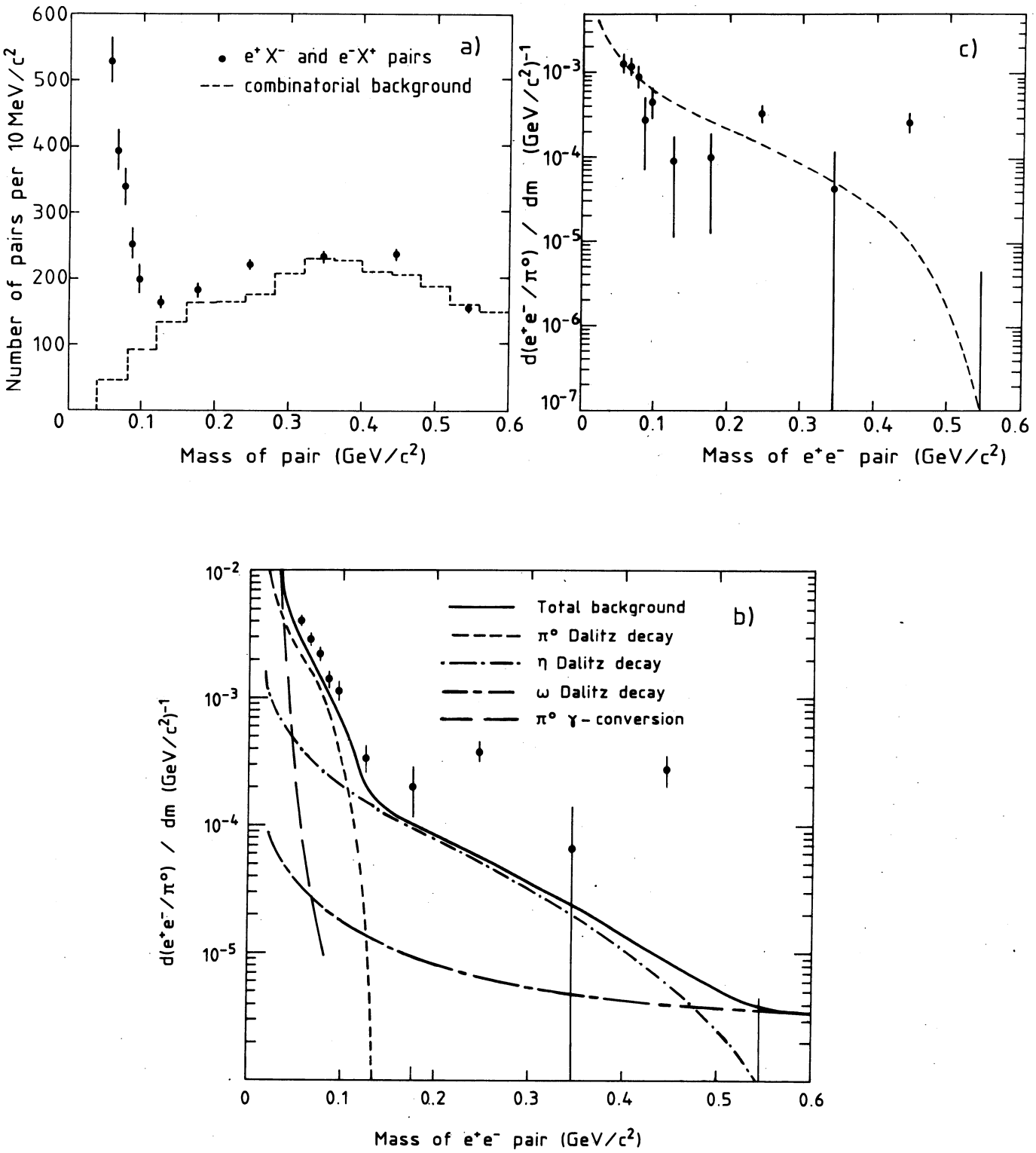

Figure 59: The mass distribution of e^+e^- pairs. a) before and b) after subtracting the combinatorial background. c) the remaining signal after subtracting the background from known sources (the dashed line is explained in the text).

The level of the signal at approximately three times the η Dalitz is in good agreement with the signal observed in the single positron measurement (see section 9.1 and figure 49). Of course, this does not mean that the signal originates from η Dalitz decays but only that η Dalitz can be used as a very simple model of the signal which demonstrates that the amount of signal seen in the e/π measurement is in quantitative agreement with what is measured in the pair analysis.

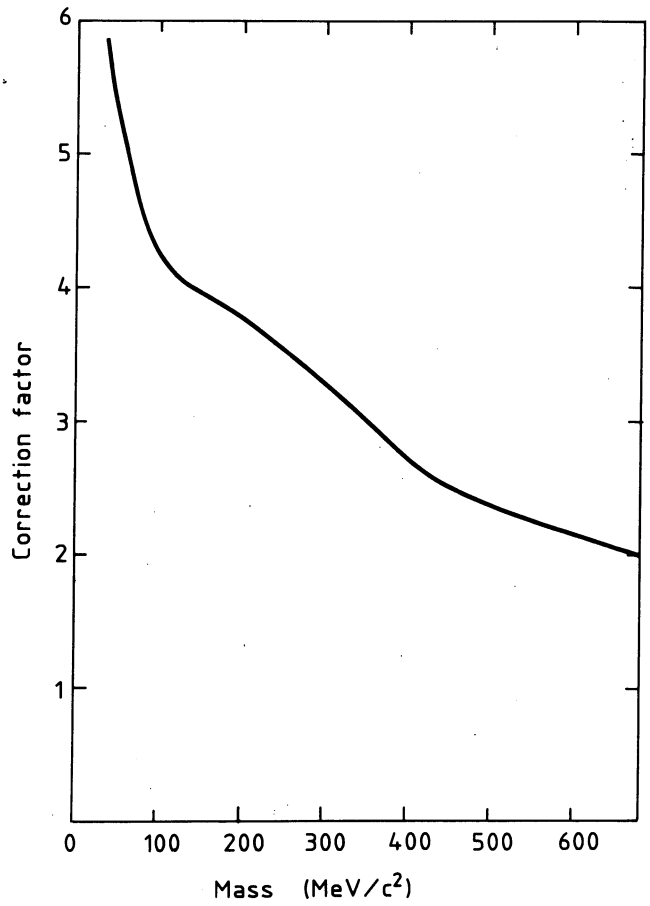

Figure 60: The acceptance correction.

In order to be able to compare these results with other experiments, the mass distribution had to be acceptance corrected. This correction function (see fig. 60) was calculated with MC assuming that the momentum spectrum of the signal was similar to that of the electrons from η and ω Dalitz decays. Acceptance in this con-

text incorporates not only the loss due to insufficient detector coverage but also the loss because of the momentum cuts imposed on the trigger electron ($200 < P < 1000$ MeV/c^2) and second electron ($40 < P < 1000$ MeV/c^2) in the pair. The assumption that the momentum spectrum of the signal resembles that of the spectrum from η and ω Dalitz decays has been verified by other experiments [34] but this assumption nevertheless introduces a systematic uncertainty into the results.

Table 20: The number of pairs (times 10^4 and per GeV/c^2) after efficiency corrections, normalized to the integrated pion spectrum at $y=0$.

m (MeV/c^2)	ee/π	ee/π_r	ee/π_r acc. corr.
50 – 60	41.22±2.87	12.97±2.87	66.13±14.65±33.3[1]
60 – 70	29.16±2.53	11.77±2.54	57.71±12.43±23.7[1]
70 – 80	22.86±2.38	9.02±2.39	41.50±10.97±17.4[1]
80 – 100	13.08±1.39	3.74±1.39	16.44±6.12±9.1[1]
100 – 200	2.75±0.59	0.96±0.59	3.83±2.38±2.6[1]
200 – 400	2.27±0.49	1.83±0.49	6.05±1.61±2.8[1]
400 – 600	1.11±0.45	1.00±0.45	2.38±1.08±1.6[1]

[1] both statistical and systematic errors are given.

ee/π	The number of pairs after efficiency correction.
ee/π_r	ee/π with known sources subtracted.
ee/π_r acc. corr.	ee/π_r after acceptance correction.

The result of the final acceptance corrected measurement of e^+e^- pairs is given in table 20 and fig. 61, together with a compilation of data from other experiments. The agreement between the different experiments is good, considering the large systematic errors involved in the extrapolation of the other experiments to $x_F = 0$ and the large systematic errors in this experiment due to the background subtraction and the large acceptance correction. It seems as if the compiled data in fig. 61 favors a $1/M^2$ dependence, however, a $1/M$ dependence cannot be ruled out. This is the first experiment which (in high energy hadron – hadron collisions) has attempted to follow the low mass pair continuum down to a mass of 50 MeV/c^2, i.e. into the mass

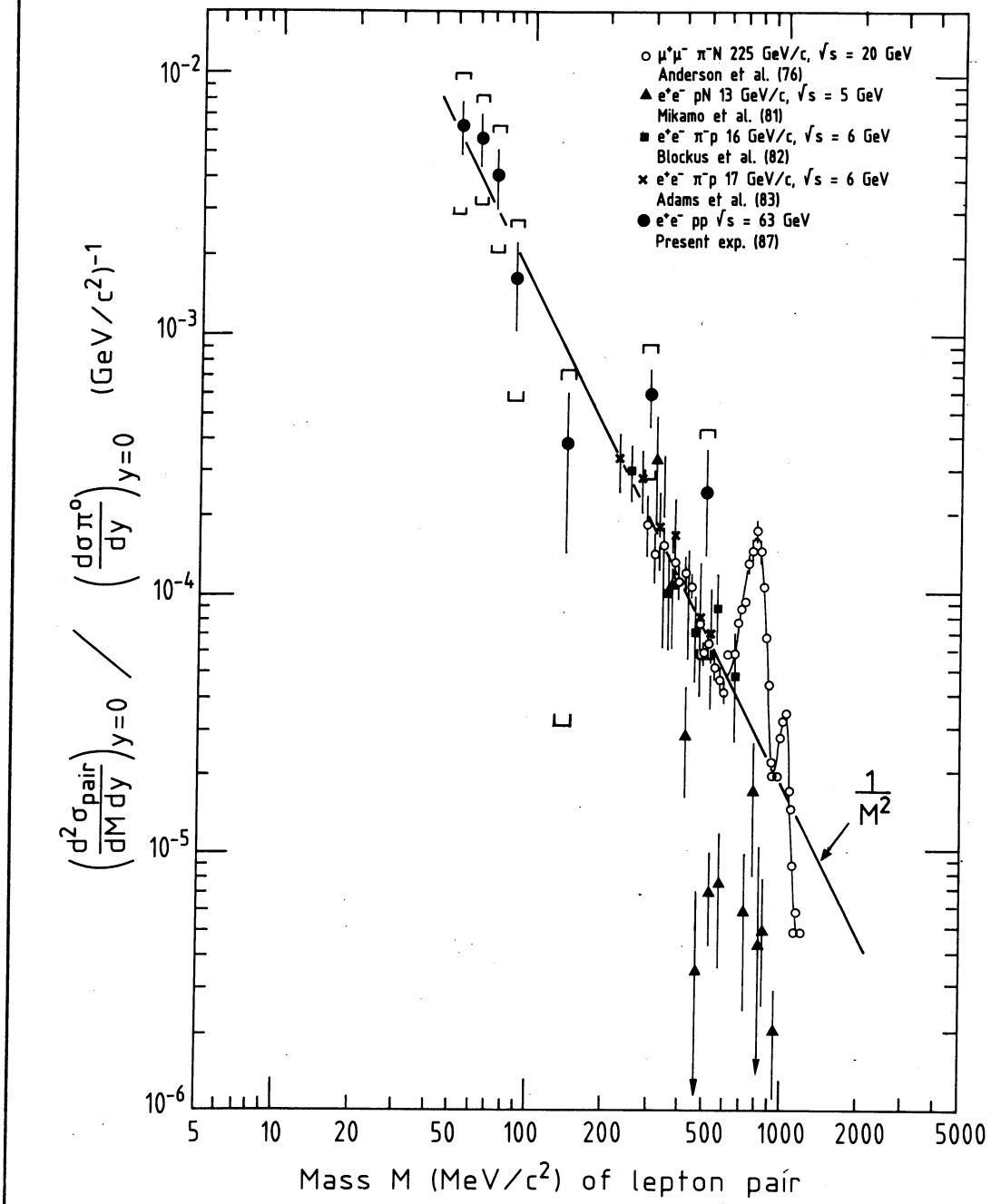

Figure 61: The acceptance corrected mass distribution.

region dominated by π^0 Dalitz decays. It should be stressed that the shape of the mass spectrum at low mass in figure 61 is strongly depending on the assumption, in the calculation of the acceptance correction, that the momentum distribution of the signal is similar to that of η and ω Dalitz decay.

10.5 THE PRODUCTION OF PAIRS AND THE E_{tot} DEPENDENCE

In the e^+/π analysis, a strong dependence of the signal on E_{tot} (or multiplicity) was observed, and an important confirmation of these results would be to see the same dependence of the pair production. In the pair analysis, the sample was divided into only three E_{tot} bins by combining the two highest bins used in the e/π analysis. Figure 62 shows the mass distributions for the three different E_{tot} bins. An increase of the signal is seen with increasing E_{tot}. This is better illustrated in fig. 63 and table 21 where the MC calculated background has been subtracted and the data has been integrated over two different mass intervals. An increase is seen both in the low-mass interval (50 – 100 MeV/c^2) and in the high mass region (100 – 600 MeV/c^2). This is in good agreement with what was found for the dependence of e^+/π on E_{tot}.

Table 21: The residual ee/π signal ·10⁴ for different E_{tot} bins.

m (MeV/c^2)	E_{tot}	$<E_{tot}>$	<n>	ee/π_r
50 – 100	2 – 5	3.9	4.9	$5.10\pm1.84\pm3.0^1$
50 – 100	5 – 8	6.3	7.7	$7.76\pm1.62\pm3.2^1$
50 – 100	8 – 18	10.3	12.0	$13.32\pm2.42\pm3.7^1$
100 – 600	2 – 5	3.9	4.9	$0.092\pm0.043\pm0.034^1$
100 – 600	5 – 8	6.3	7.7	$0.023\pm0.043\pm0.045^1$
100 – 600	8 – 18	10.3	12.0	$0.387\pm0.079\pm0.094^1$

[1] both statistical and systematic errors are given.

E_{tot}	The E_{tot} bin in GeV.
$<E_{tot}>$	The mean E_{tot} in GeV.
<n>	The mean charged multiplicity.
ee/π_r	ee/π with known sources subtracted per GeV/c^2.

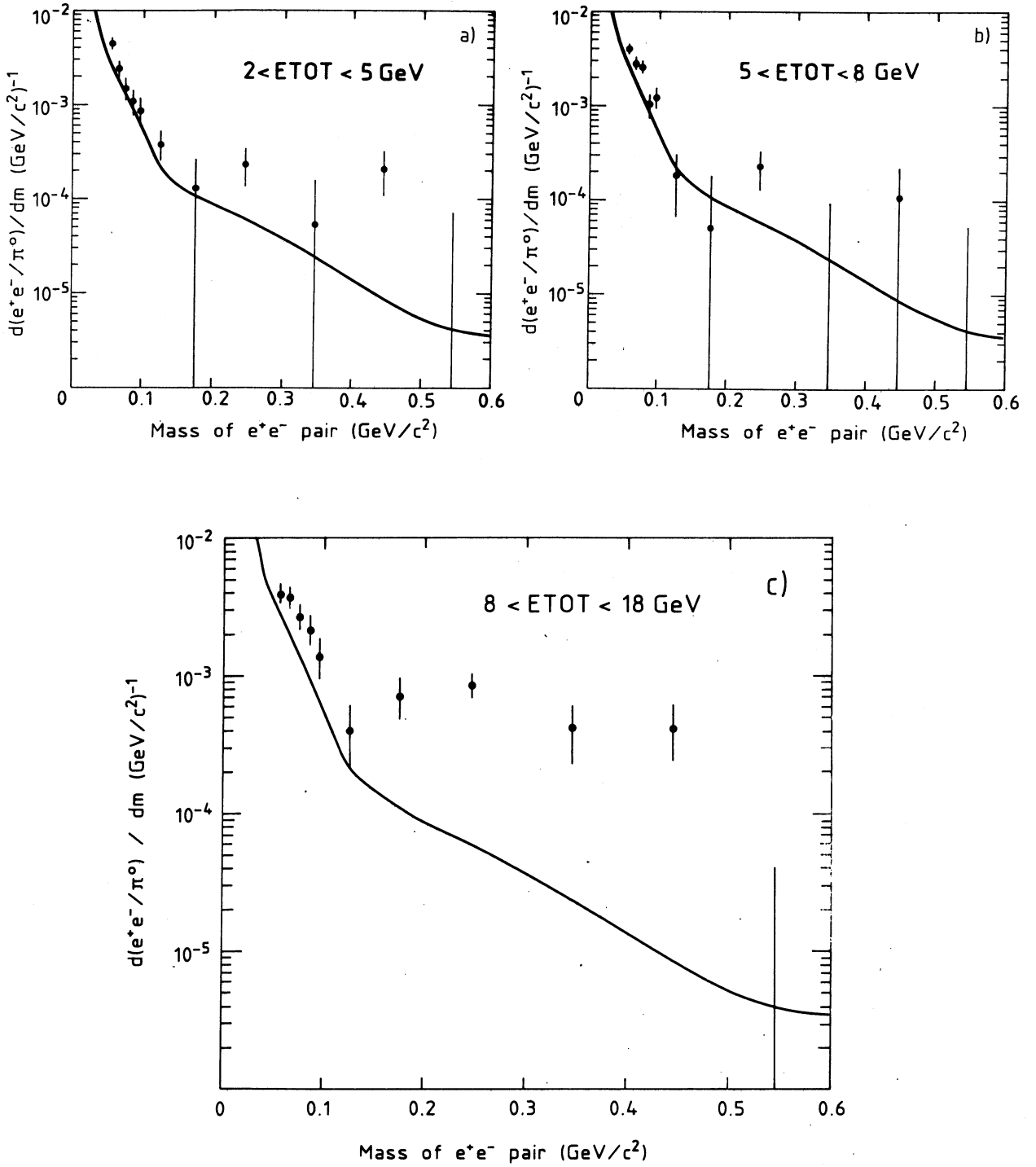

Figure 62: The mass distributions for different E_{tot} bins.
The expected contribution from all known sources is shown as a line.

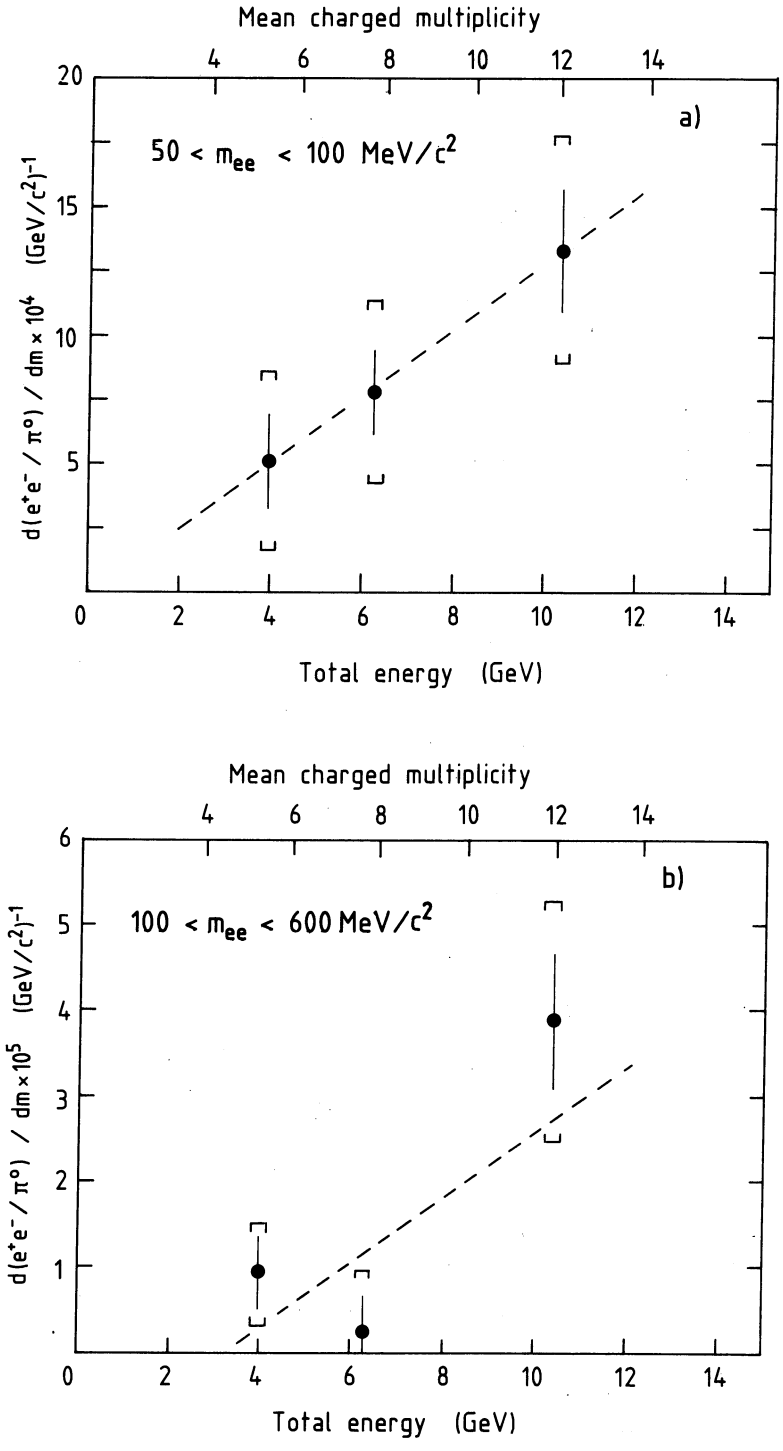

Figure 63: The pair signal as a function of E_{tot}.

A linear least square fit to the data was made in the same way as in the single e/π measurement and the resulting parameters are given in table 22 . The CL for a constant value was in the low–mass region 0.03 and in the high mass region only 0.0002, which means that the rise was even more statistically significant in the pair measurement than in the e/π measurement. However, the systematic uncertainties were much larger in the pair measurement.

Table 22: Fit to the function $ee/\pi = (A + B \cdot E_{tot}) \cdot 10^{-4}$.

m (MeV/c^2)	A	B	χ^2	NDF
50–100	-0.1 ± 3.2	1.3 ± 0.5	0.02	1
100–600	-0.12 ± 0.08	0.038 ± 0.014	9.1	1

NDF Number of Degrees of Freedom.

10.6 TESTS OF THE RESULTS AND POSSIBLE SYSTEMATIC ERRORS

The estimated systematic error due to normalization and efficiency corrections was $\pm 11\%$ (see table 23). In order to further check this aspect of the analysis, the abstraction of the MB triggered data was repeated without a mass cut so that the mass spectrum could be followed down to the zero–mass peak which is mainly due to the converted photons. As can be seen in fig. 64 the signal disappears for masses less than 40 MeV/c^2, which is what one would expect since the signal to background ratio should be more or less zero in the mass region dominated by pairs from γ conversions. This indicates that the observed signal is not due to a simple normalization error.

The systematic error in the MC calculation is estimated to be $< 12\%$. This limit on the systematic error is surely correct for $m > 100$ MeV/c^2 but is more questionable in the 50–100 MeV/c^2 mass range where a difference in the mass resolution between data and MC could introduce a large systematic error in the final result. However, studies of the effect of multiple scattering (see section 6.5) on the calculated residual background indicated that the results are not sensitive to this process. It should be noted that a systematic error in the estimated mass resolution in the MC cannot explain the observed strong increase of the signal with increasing E_{tot}.

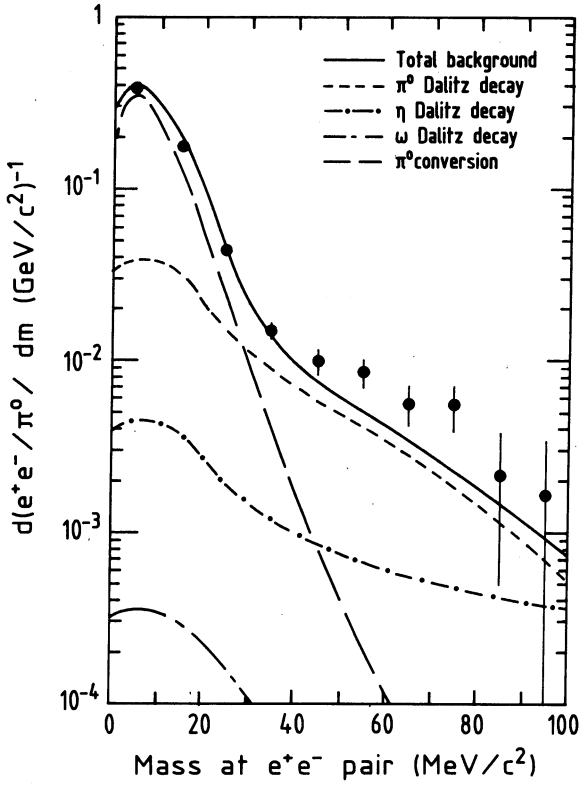

Figure 64: The lower end of the mass spectrum (MB triggered data only).

Table 23: The systematic errors in the pair analysis.

11%	error in the calculation of ee/π (efficiency corr.,pion norm. etc);
12%	error in the MC calculation of background from known pair sources;
25%	error in the acceptance correction;
4%	error in the calculated combinatorial background.

The largest systematic problem in the high mass range (>100 MeV/c^2) was the calculation of the combinatorial background. Some of the tests, which were made to check that nothing obvious was wrong with the method used to calculate the combinatorial background, have already been mentioned in section 10.1 . As an additional test, the background was estimated with $e^+x^+ + e^-x^-$ without using the conversion sample and this gave both a similar signal (see table 24) and a similar E_{tot} dependence. In a final test, the conversion sample was used after the P_T of the trigger track had been changed (as described in section 10.1). The combinatorial background calculated with like–sign pairs was subtracted from the combinatorial background calculated with unlike–sign pairs, i.e $(e^+x^- + e^-x^+) - (e^+x^+ + e^-x^-)$. This difference was zero within the statistical errors (see table 24), also as a function of E_{tot}.

Table 24: Results of the pair analysis done with combinations of different event samples.

m	Signal	Comb. Back.	ee/π	ee/π_r
50–100	$e^+x^- + e^-x^+$ S	$e^+x^+ + e^-x^-$ S	22.8±1.1	7.20±1.1
50–100	$e^+x^- + e^-x^+$ S	$e^+x^- + e^-x^+$ C	23.9±1.1	8.25±1.1
50–100	$e^+x^- + e^-x^+$ C	$e^+x^+ + e^-x^-$ C	−1.01±0.40	–
100–600	$e^+x^- + e^-x^+$ S	$e^+x^+ + e^-x^-$ S	2.00±0.35	1.44±0.35
100–600	$e^+x^- + e^-x^+$ S	$e^+x^- + e^-x^+$ C	1.90±0.29	1.35±0.29
100–600	$e^+x^- + e^-x^+$ C	$e^+x^+ + e^-x^-$ C	0.25±0.21	–

m	The mass bin in MeV/c^2.
Comb. Back.	Combinatorial background.
S	The "single" sample.
C	The "conversion" sample.
ee/π	The measured ee/$\pi \cdot 10^4$ per GeV/c^2.
ee/π_r	ee/π with known sources subtracted.

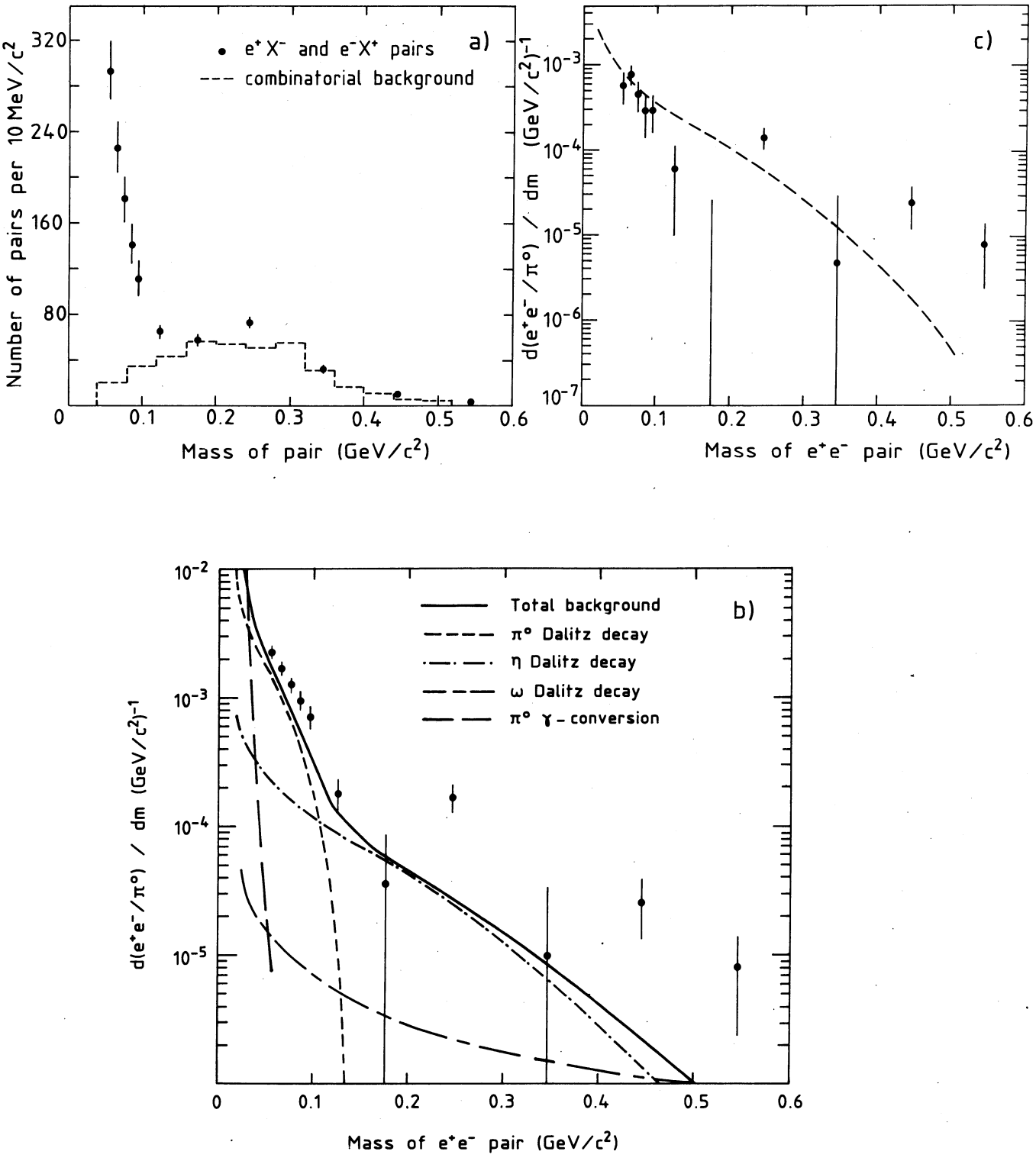

Figure 65: The mass distribution of e^+e^- pairs when $40 < P_2 < 140$ MeV/c². a) before and b) after subtracting the combinatorial background. c) the remaining signal after subtracting the background from known sources.

Finally, the analysis was repeated with the low momentum range (40 – 140 MeV/c) for the second electron which gave less combinatorial background but also larger statistical errors (and a much smaller acceptance for the pairs of interest to this experiment). The signal measured with this momentum cut was in good quantitative agreement with three times η Dalitz decay (the dashed line in figure 65 c) and thus comparable with the signal measured in the high momentum range (fig. 59 c). An increasing pair signal with increasing E_{tot} was also observed with the low momentum range.

If one takes the results of all these tests into consideration, it is highly unlikely that the signal at $m > 100$ MeV/c^2 is due solely to an error in the calculation of the combinatorial background.

10.7 COMPARISON WITH OTHER PAIR EXPERIMENTS

Two previous ISR experiments have studied the production of low – mass (< 600 MeV/c^2) e^+e^- pairs (see table 25). The first experiment [5] found only about 18 low – mass pairs while the second experiment [4] observed a statistically significant low – mass pair continuum. Both experiments concluded that the observed production rate of pairs could be explained by Dalitz decays and semileptonic decays of $D\bar{D}$ pairs. It should be noted, that these experiments measured pairs with a high P_T^2 ($P_T^2 > 4$ (GeV/c)^2 for [5] and $P_T^2 > 3.2$ (GeV/c)^2 for [4]) and that the present experiment and other experiments which have observed the so – called "anomalous" pair continuum have concluded that these pairs are mostly produced at low P_T^2 (< 1 (GeV/c)^2). For this reason the two previous ISR experiments do not contradict the results of this and other experiments which have observed the anomalous low – mass pair continuum.

Two πp fixed target experiments at $\sqrt{s} = 6$ GeV, i.e. at an energy one order of magnitude lower than that of this experiment, have studied the low – mass e^+e^- pair continuum in about the same x_F range (see table 25). The first experiment [35] (carried out at SLAC) reported the observation of a low – mass signal containing 59 events, while the second experiment [34] (carried out at BNL) found a signal of 98 pairs. Comparisons between the x_F and P_T^2 distributions as measured by these two experiments are given in figure 66 . The x_F dependence suggests that most of the low – mass signal is produced centrally (at low x_F). It is also clear from figure 66 that the low – mass pair signal is produced at low P_T^2 (< 1 (GeV/c)^2).

The results of a measurement of the e/π ratio by a collaboration at KEK [20], has already been discussed in section 9.4 . The center – of – mass energy in this pBe fixed target experiment was ~5 GeV. The same collaboration has studied the production of low – mass e^+e^- pairs [37] at $x_F \simeq 0$ and they found 144 pairs before subtracting the known sources. This experiment also concluded that the measured low – mass continuum could not be fully explained by conventional sources.

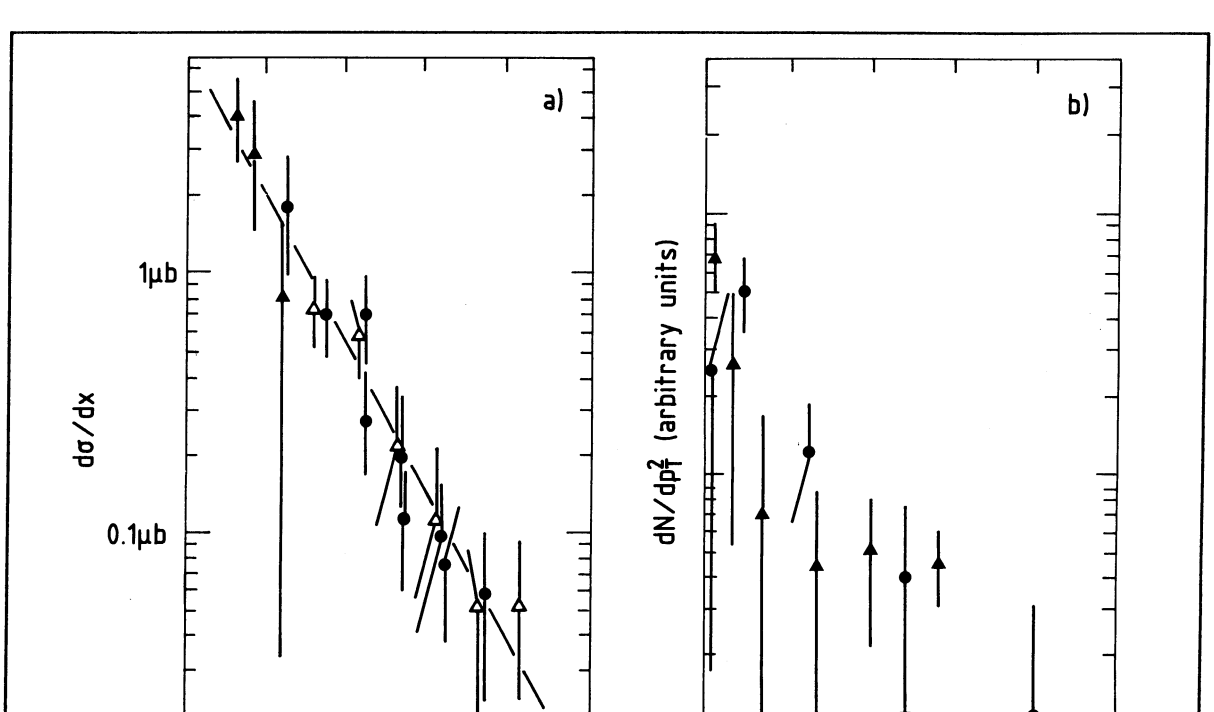

Figure 66: A compilation [34] of previous measurements of x_F and P_T^2 for "anomalous" pairs. In the x_F plot circles are from [34], closed triangles from [35] and open triangles from [28]. In the P_T^2 plot circles are from [34], and triangles from [35].

In addition to these experiments there are three πp bubble chamber experiments that have studied the production of low-mass e^+e^- pairs with a $\sqrt{s}$ ranging from 3 to 12 GeV [38] [39] [22]. A main feature of these experiments was the small pair sample which was typically < 20 events. One of the experiments [39], observed an excess of 16.1±4.7 pairs above Dalitz decays sources in π^-p collisions but no excess in π^+p interactions, while another experiment [22], found 15.2±4.6 pairs above Dalitz decays which were attributed to $D\bar{D}$ decays. The lowest energy experiment [38], had 7 events with $m > m_\pi$ and concluded that these events could all be explained by known sources. What is perhaps more interesting, is that this experiment also studied pairs with $m < m_\pi$ with high statistics. No excess of pairs above what would be expected from π^0 Dalitz decays was reported.

Table 25: A compilation of low–mass l^+l^- experiments.

Colliding beam experiments measuring e^+e^-:

Ref.	Exp. location	B&T	P_b	$\sqrt{s}$	m	X_F
*	AFS at ISR/CERN	pp	31.5	63	50	≈0
[4]	R702 at ISR/CERN	pp	27,31.5	53,63	60	≈0
[5]	R806 at ISR/CERN	pp	27,31.5	53,63	200	≈0

Fixed target experiments measuring e^+e^-:

Ref.	Exp. location	B&T	P_b	$\sqrt{s}$	m	X_F
[35]	LASS at SLAC	πp	16	6	200	0.1 – 0.45
[34]	at BNL	πp	17	6	200	0.2 – 1.0
[37]	at KEK	πBe	13	5[1]	300	≈0
[38]	RLCBC at RAL	πp	4	3	≈0	–
[39]	1BC at SLAC	πp	18	6	135	–0.25 – 0.25
[22]	BEBC at SPS/CERN	πp	70	12	135	–

Fixed target experiments measuring $\mu^+\mu^-$:

Ref.	Exp. location	B&T	P_b	$\sqrt{s}$	m	X_F
[25]	UCCS at FNAL	pBe,πBe	150	17[1]	210	0.15 – 1.0
[26]	UCCS at FNAL	πC	225	21[1]	210	0.15 – 1.0
[33]	at AGS/BNL	pW,pFe,pC	29	8[1]	210	0.3 – 0.7
[28]	2SC at SLAC	πp	16	6	210	0.3 – 1.0
[27]	at FNAL	pCu	400	27[1]	210	0.15 – 0.5
[29]	at AGS/BNL	πCu	16,22	6[1]	210	0.25 – 0.65
[30]	LEPTON at Serpukov	πp	18	6	210	–0.25 – 0.25
[32]	at SLAC	$K_L{}^0$Cu	4 – 20	6[1]	210	> 0.25

* this experiment
[1] calculated for pp collisions

B&T	Beam and Target.
P_b	The beam momentum in GeV/c.
$\sqrt{s}$	The center–of–mass energy in GeV.
m	The minimum mass measured in MeV/c^2.
X_F	The Feynman X interval covered by the experiment.

There are many fixed target experiments which have been investigating low-mass ($2m_\mu < m < 600$ MeV/c^2) $\mu^+\mu^-$ pair production (see table 25) but there have been no colliding beam experiments. The $\sqrt{s}$ range covered by these experiments is larger than that for the fixed target e^+e^- experiments but the highest energy experiments [27] [26] are still at a significantly lower $\sqrt{s}$ than what was reached at the ISR. The $\mu^+\mu^-$ pair experiments have, in contrast to the e^+e^- experiments used a wide range of target materials (p,Be,W,Fe,C,Cu) and beam particles (π,p,K,$\bar{p}$,K_{0L}). The first observations of the low-mass dilepton continuum were reported by the Chicago-Princeton collaboration at FNAL in 1976. This collaboration used 150 GeV/c π^+ and p beams on beryllium targets [25] and in a later study, a 225 GeV/c π^- beam on a Carbon target [26].

One of the problems which has been studied in relation to the low-mass lepton continuum is whether these pairs follow Feynman scaling, i.e. if the x_F distribution is independent of the center-of-mass energy $\sqrt{s}$. The BNL e^+e^- experiment [34] compared their x_F distribution with that of the SLAC e^+e^- experiment [35] and with another $\mu^+\mu^-$ experiment done at SLAC [28]. All three experiments were performed at the same $\sqrt{s}$ and agree (after "converting" ee pairs to $\mu\mu$ pairs) within statistical errors (see fig. 66). An exponential fit to the combined data in x_F gave a slope of 6.0 ± 0.9. The more interesting question is what happens if x_F distributions obtained at different $\sqrt{s}$ are compared. Here the situation is a bit more confused. The SLAC e^+e^- experiment [35] compared its x_F distribution with that which was measured by the 225 GeV/c $\mu^+\mu^-$ experiment at FNAL [26]. As mentioned above the SLAC data showed an exponential slope of ~6 while the FNAL data was much steeper (the exponential slope was ~16). On the other hand, a $\mu^+\mu^-$ experiment at BNL [33] compared its $\mu^+\mu^-$ data from pp collisions at 28 GeV/c with data recorded with 150 GeV/c protons on Beryllium [25] and with 400 GeV/c protons on Copper [27]. The result from this comparison was that Feynman scaling was obeyed. It seems as if more high energy, high statistics data over a large x_F range is needed to settle this question.

Another problem is how the production cross section depends on the target material. It has been shown that the dependence on the the atomic number (A) is well described by a power law like $\sigma = \sigma_0 \cdot A^\alpha$ [26] [46]. The value for α at low mass ($<$ 1 GeV/c^2) has been measured to be ~2/3, while α approaches 1 at high mass.

As far as the beams are concerned, it does not seem as if positive or negative pions make a large difference. The streamer chamber experiment at SLAC [28] found the following ratio of cross sections, for the production of low-mass $\mu^+\mu^-$ pairs, in measurements with different pion beams: $\sigma(\pi^-p\rightarrow\mu^+\mu^-) \,/\, \sigma(\pi^+p\rightarrow\mu^+\mu^-) = 1.28\pm0.23$. However, a comparison [25] of measurements with a π^+ beam and a p beam showed that the x_F distribution was steeper when a p beam was used. The crossing point was at $x_F \simeq 0.2$ which means that a p beam is more effective than a π beam in producing $\mu\mu$ pairs at low x_F (<0.2) while the opposite is true at high x_F (>0.2).

11. PHYSICS DISCUSSION

As described in detail in section 10.7, a number of experiments have reported observations of an excess of low–mass lepton pairs (sometimes called the "anomalous" lepton pair continuum) which cannot be explained by known pair sources, such as Dalitz decays and direct decays of the vector mesons ρ, ω and ϕ. Fig. 67 shows the mass spectrum for lepton pairs in a qualitative way. The lepton pair continuum can be divided into three parts, the low–mass continuum ($m < m_\rho$) which is of interest to this experiment, an intermediate continuum ($m_\rho < m < m_{J/\psi}$), possibly originating from the decay of $D\bar{D}$ pairs, and the well understood high mass Drell–Yan continuum ($m > m_{J/\psi}$).

In this experiment, both single positron production and low–mass e^+e^- pair production have been studied. Although, large systematic uncertainties exist in the pair analysis, it seems as if the signal seen in the e^+/π analysis, can be attributed to the low–mass pair continuum. Several previous e^+e^- experiments [34] [35] have tried to extract the expected low–P_T e/π ratio from a pair measurement but only one other experiment, at KEK [20] [37], has actually measured both single electrons and e^+e^- pairs. The conclusion from the KEK experiment, although carried out at a higher P_T and mass than this experiment, was that the rising e/π ratio at low P_T could be explained by the low–mass dilepton continuum.

Many different types of processes have been given to explain the low–mass lepton pair continuum. The following lists some of these:

1. The decay of η mesons
2. The decay of vector mesons (ρ,ω and ϕ)
3. The decay of tensor mesons (f and A_2)
4. The semileptonic decay of $D\bar{D}$ pairs
5. The decay of a new broad non resonant state into $e^+e^-\gamma$
6. Hadronic bremsstrahlung
7. Quark bremsstrahlung
8. $q\bar{q}$ annihilation as described by the soft annihilation model
9. $q\bar{q}$ annihilation as described by the thermodynamic models

The most trivial explanation for the rise of the e/π ratio and perhaps for some of the signal seen by the pair experiments would be a large underestimation of the contribution from η production. One previous experiment [18] did not believe that

the observed rise in the e/π ratio at low P_T was significant considering the systematic uncertainty due to the unknown production rate of η mesons with low P_T. In this AFS experiment it was found that about three times more e^+e^- pairs than what was expected from η decays could explain the signal. For this reason, it is of great importance that this experiment, for the first time, has measured the η/π ratio at low P_T so that it is possible to firmly exclude this type of background as the explanation for the rise of the e/π ratio at low P_T. The BNL e^+e^- experiment [34] which studied the associated photons in the low–mass pair events, concluded that the signal was not produced with an $e^+e^-\gamma$ configuration. This tends to rule out an explanation invoking Dalitz decays of any type, including that of η mesons.

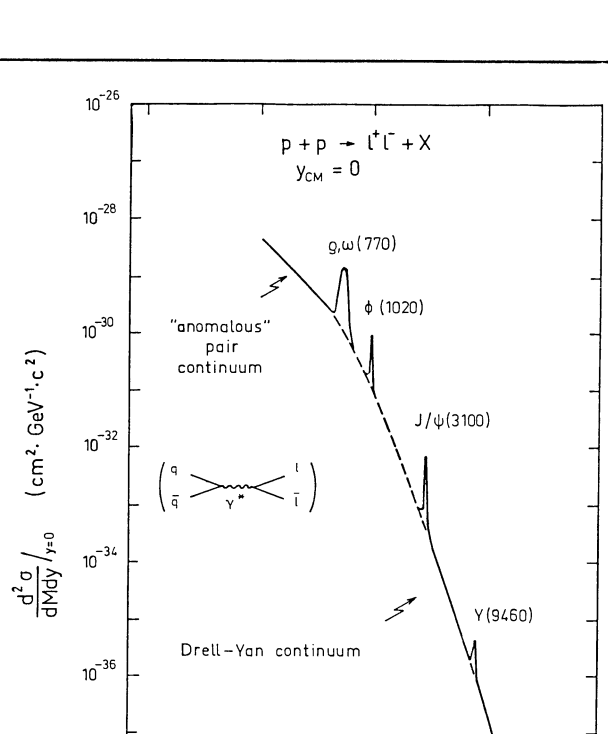

Figure 67: The lepton pair continuum [114].

Craigie and Schildknecht [113] have suggested that a large fraction of the low–mass lepton pair continuum could be due to the decay of the ρ meson into a lepton

pair. The reason for this should be that a narrow resonance approximation for $\rho \rightarrow l^+l^-$ decay does not correctly take into account the photon propagators dependence on q^2 which should, if taken into account, give a low–mass tail. The streamer chamber experiment at SLAC [28] observed a good agreement between the measured $\mu^+\mu^-$ mass distribution and the calculation of Craigie and Schildknecht but they pointed out that the x_F distribution of the low–mass pair continuum is steeper than what would be expected for the lepton pairs from ω and ρ decay. The calculated single e/π ratio, due to the decay of vector mesons, rises as $1/P_T$. The total contribution to e/π at low P_T, however, seems to be at least one order of magnitude lower than what is observed in this AFS measurement.

Dunbar [115] has suggested that the decay of the tensor mesons f and A_2 into a lepton pair and a vector meson could explain the low–mass pair continuum. However, several experiments [34] [28] studying the associated event structure have concluded that tensor meson decay can only account for a small part of the continuum.

The known sources which contribute to the measured e/π ratio are plotted in fig. 49 . In the P_T region of 0.5 – 1 GeV/c, the semileptonic decay of charmed particles, in particular that of the D mesons, is the dominant source of the inclusive lepton yield. Owing to large systematic errors at low P_T in some previous experiments [18], the reported e/π ratio has been consistent with the expected contribution from open charm. The systematic errors in this experiment and the shape of the charm P_T spectrum now makes it possible to exclude charm as the dominant part of the low–P_T yield, in spite of the existing uncertainties in the absolute production cross section.

The semileptonic decay of D mesons can produce not only single leptons but also lepton pairs if both members in a $D\bar{D}$ pair decay into $eK\nu$. Fischer and Geist [14] have shown that the same arguments used in connection with the single P_T spectrum from charm can be used for the dilepton mass spectrum from $D\bar{D}$ decays, i.e. although the charm production cross section is not well known, the shape of the dilepton mass spectrum is such that it can be excluded as the main explanation for the observed low–mass continuum. While the measured pair continuum is observed to rise rapidly with decreasing mass, the expected mass distribution from $D\bar{D}$ decay has a maximum at about 0.5 GeV/c^2 and is rapidly decreasing below this peak.

As has been reported in section 6.3.2, calculations by this experiment and by e.g. Craigie and Thompson [41] show that hadronic bremsstrahlung cannot explain more than 10% of the rise of the e/π ratio at low P_T. Since the signal seen in the e/π measurement in this experiment is consistent with originating from the pair continuum, it is clear that hadronic bremsstrahlung cannot be the major source of low–mass dileptons.

In addition to virtual photons originating from the acceleration of charged hadrons created in the interaction, it is possible to conceive a contribution from bremsstrahlung photons due to the acceleration of quarks created in the collision. This source of lepton pairs was proposed by Farrar and Frautschi [116] but a quantitative estimate was not given and this source can therefore not be compared with the measured qualities of the dilepton continuum. It is not inconceivable that internal conversion of photons from quark bremsstrahlung can contribute in a significant way to the dilepton continuum.

The Drell – Yan mechanism [117] can describe the high mass ($m > m_{J/\psi}$) lepton pair continuum very well. In this model, the annihilation of a quark and an antiquark in the incoming hadrons results in the production of a lepton pair ($q\bar{q} \rightarrow \gamma^* \rightarrow l^+l^-$). Extrapolation of the Drell – Yan continuum to the low – mass region (< 0.6 GeV/c^2) shows that the production rate is more than one and perhaps as much as two orders of magnitude lower [34] [118] than what is seen experimentally. For this reason Bjorken and Weisberg [52] suggested that the quarks and antiquarks, that are produced in the collision, should be taken into account. By doing this, the Drell – Yan mechanism could be significantly enhanced at low masses. Difficulties in reproducing the x_F and P_T^2 distributions with this model, made the SLAC e^+e^- experiment [35] suggest a Dalitz like decay of a $q\bar{q}$ continuum ($q\bar{q} \rightarrow \gamma\gamma^* \rightarrow \gamma e^+e^-$) so that the photon could carry away some of the momentum and thus soften the P_T spectrum of the e^+e^- pair. However, the BNL e^+e^- – experiment [34] did not see accompanying photons in the low – mass pair events and it has therefore been suggested that a more likely decay process is one where the photon in the Dalitz decay has been replaced by a gluon ($q\bar{q} \rightarrow g\gamma^* \rightarrow ge^+e^-$). Cerny, Lichard and Pisut developed these ideas into a quantitative model, the so – called soft annihilation model, and incorporated the concept of space time evolution of the collision into it [51]. The soft – annihilation model has been shown to reproduce the data fairly well.

Another group of models, closely related to the soft annihilation model, are the thermodynamic models, e.g the one proposed by Shuryak [49] [50] [53]. In these models, like in the soft annihilation model, a so – called "quark – gluon soup" is produced after the collision and the e^+e^- pairs are created through quark – antiquark annihilations. The difference between the soft – annihilation model and the thermodynamic models is that while the former model assumes that all quarks and antiquarks finally recombine to mesons, the latter models use thermodynamic language to describe the "soup".

It has recently been pointed out by Cerny et al. [48] that information about the production mechanism of the low – mass e^+e^- continuum can be obtained by studying the associated charged multiplicity in a rapidity region close to that of the lepton pairs. If the dileptons are created after the final hadrons have been produced (e.g. by hadron decays or hadronic bremsstrahlung), the mean number of dileptons per event will be proportional to the number of final hadrons, thus giving a constant value of the e/π ratio. In another class of models, the production of dileptons should

be proportional to the square of the charged multiplicity. This class of models contains the thermodynamic models [53] [54] and the soft annihilation model [48]. It should be noted that while the production of hadronic bremsstrahlung is expected to show a linear dependence on the associated charged multiplicity, quark bremsstrahlung would give a square dependence in the same way as quark–antiquark annihilation [119].

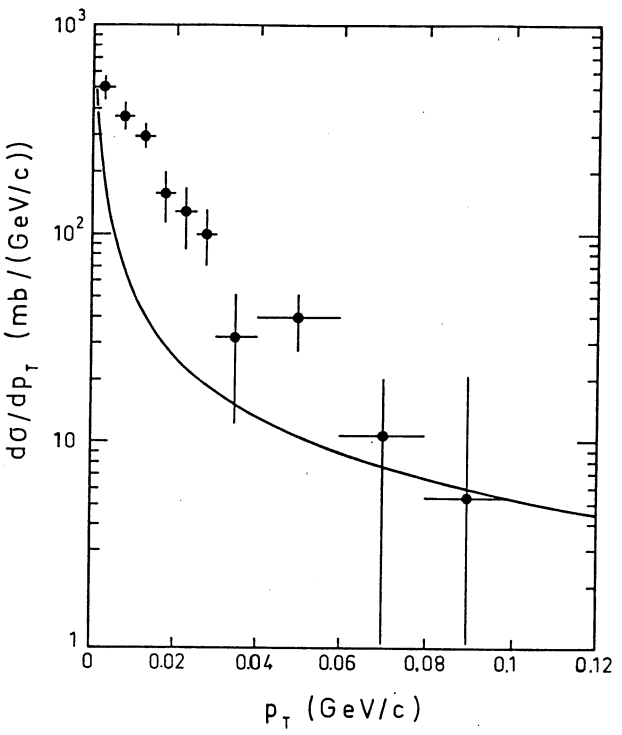

Figure 68: P_T spectrum of soft real photons [120].

In this analysis it has been shown that the e/π ratio increases significantly with increasing charged multiplicity in the low–P_T region, where an excess of positrons has been seen above known sources, i.e. charm and bremsstrahlung. Also the production rate of e^+e^- pairs, normalized to the integrated pion spectrum, shows a striking increase with increasing charged multiplicity. This means that there now exists another way (than by Monte Carlo calculation) of excluding the six first explanations in the list above.

One previous e^+e^- experiment [34] at BNL has studied associated photon and charged particle production. No measurement of the dependence of the pair signal on charged multiplicity was presented but the following statement about the anomalous pair events was made:*"There is no enhancement over ordinary events in associated photon or charged particle production."*

The observation of a new form of lepton pair production, most likely with an electromagnetic origin, also makes it interesting to study the production of real photons. The BNL experiment estimated an accompanying signal of direct real photons of the order of $\gamma/\pi = 0.08$ assuming that the virtual photons can be connected to the real photons by the standard internal conversion prescription. The SLAC e^+e^- experiment [35] came to a similar conclusion and estimated a γ/π ratio of a few percent at $P_T \sim 1$ GeV/c for all x_F, increasing to 10–20% at low P_T and x_F.

Table 26: A compilation of low – P_T γ/π experiments.

Colliding beam experiments

Ref.	Exp. location	B&T	P_b	$\sqrt{s}$	P_T	θ_{cm}
[121]	AFS at ISR/CERN	pp	31.5	63	15	90°

Fixed target experiments

Ref.	Exp. location	B&T	P_b	$\sqrt{s}$	P_T	θ_{cm}
[42]	BC at SLAC	pp	11	5	≈0	–
[120]	BEBC at SPS/CERN	Kp	70	12	≈0	–
[122]	at AGS/BNL	pp	24	7	500	90°

B&T	Beam and Target.
P_b	The beam momentum in GeV/c.
$\sqrt{s}$	The center of mass energy in GeV.
P_T	The minimum P_T measured in MeV/c^2.
θ_{cm}	The center of mass angle in relation to the beam.

Two bubble chamber experiments have seen a signal of direct real photons at low P_T and x_F (see table 26). The first experiment [42] at SLAC reported a pho-

ton signal in 10.5 GeV/c πp interaction which could be attributed to hadronic bremsstrahlung. Another experiment at CERN [120] which also observed a real photon signal, claims that this signal cannot be explained by hadronic bremsstrahlung. The P_T spectrum of the γ/π ratio measured by this experiment is plotted in fig. 68 . The signal is only seen at very low x_F and P_T (<60 MeV/c). Within the AFS collaboration two independent attempts have been made to look for such a soft real photon signal. Both analysis have resulted in upper limits of the order of $10-15\%$ [121]. New high accuracy measurements of soft real photons are clearly needed. However, the expected γ/π ratio is low ($\sim 10\%$) in minimum bias events and one way of increasing the signal to background ratio might be to study the production rate of the photons as a function of associated charged multiplicity.

12. SUMMARY AND CONCLUSIONS

In this experiment the production of inclusive single positrons down to a P_T of 80 MeV/c has been measured, which is lower than that of any previous experiment. The e/π ratio is found to rise, with decreasing P_T, to a level of $\sim 1.6 \cdot 10^{-3}$ at $P_T = 100$ MeV/c. This is one order of magnitude higher than what would be expected from known sources such as hadronic bremsstrahlung and the decay of charmed particles.

One of the largest systematic uncertainties in previous experiments has been the unknown background of electrons originating from the decay of low $-P_T$ η mesons. It is therefore of importance that the η/π ratio has been measured in this experiment. The η/π ratio, integrated over the P_T range 0.2 – 1.5 GeV/c, was found to be 0.07 ± 0.055 which is consistent with the predictions of m_T scaling.

This is the first ISR experiment that has studied the production of pairs with low mass and P_T. It is also one of the first experiments anywhere which has measured both the production of single low $-P_T$ positrons and low – mass e^+e^- pairs. The production of so – called "anomalous" pairs has been measured down to a mass of 50 MeV/c which is a considerably lower value than what has been reported by previous experiments. It has been found that the excess of pairs above known sources is at such a level that it can explain the signal seen in the single measurement. Although the pair signal has limited statistics and a large systematic uncertainty, it is highly probable that the signal observed in the single positron measurement is due to the low mass pair continuum.

Several previous experiments have also observed the production of lepton pairs with masses less than 600 MeV/c^2. The origin of these pairs, however, has been mysterious. With the observation, in this experiment, of a dependence on the associated charged multiplicity of both the single and the pair signal, some new insight into the possible production mechanism is now available. It is believed that this form of multiplicity dependence is described by collective models such as the thermodynamical models and the soft annihilation model while it rules out hadronic decays and hadronic bremsstrahlung as an explanation for the signal.

It has been suggested that the phase transition between hadronic matter and quark matter in very high energy nucleus – nucleus collisions could be detectable by measuring the production rate of lepton pairs [53] [55] – [58]. Among other features, a square dependence of this rate on particle multiplicity is predicted as one of the signatures for the quark – gluon plasma [54]. As the same characteristic increase of the lepton production rate is seen already in pp collisions, it must be in the quantitative analysis of the lepton pair production in ultrarelativistic nuclear collisions that new effects should be sought.

REFERENCES

[1] F.W. Busser et al.,Phys. Lett. 53B(1974)212;
F.W. Busser et al.,Nucl. Phys. B113(1976)189.
[2] J.P. Boymond et al.,Phys. Rev. Lett. 33(1974)112.
[3] V.V. Abramov et al.,Phys. Lett. 64B(1976) 365.
[4] A. Chilingarov et al.,Nucl. Phys. B151(1979)29.
[5] J.H. Cobb et al.,Phys. Lett. 78B(1978)519.
[6] R. Singer et al.,Phys. Lett. 60B(1976)385.
[7] M.G. Albrow et al.,Nucl. Phys. B155(1979)39.
[8] C. Kourkoumelis et al.,Phys. Lett. 84B(1979)277.
[9] M. Diakonou et al.,Phys. Lett. 89B(1980) 432.
[10] J.H. Cobb et al.,Phys. Lett. 68B(1977)101.
[11] M. Basile et al.,Nuovo Cimento 65A(1981)421.
[12] P. Perez et al.,Phys. Lett. 112B(1982)260.
[13] M. Basile et al.,Nuovo Cimento 65A(1981)457.
[14] H.G. Fischer and W.M. Geist,Z. Phys. C19(1983)159.
[15] W.M. Geist,Proc. 2nd Moriond Workshop on New flavours (Les Arcs,1982) (Editions Frontieres,Gif – sur – Yvette,1982) p.407.
[16] G.H. Trilling,Phys. Rep. 75(1981)57.
[17] L. Baum et al.,Phys. Lett. 60B(1976)485.
M. Barone et al.,Nucl. Phys. B132(1978)29.
[18] M. Heiden,Ph.D.Thesis,CERN EP Internal Report 82 – 05(1982).
[19] E.W. Beier et al.,Phys. Rev. Lett. 37(1976)1117.
[20] A. Maki et al.,Phys. Lett. 106B(1981)423.
[21] Y. Makdisi et al.,Phys. Rev. Lett. 41(1978)367.
[22] R. Barloutaud et al.,Nucl. Phys. B172(1980)25.
[23] J.L. Ritchie et al.,Phys. Rev. Lett. 44(1980)230.
[24] J.G. Branson et al.,Phys. Rev. Lett. 38(1977)457.
[25] K.J. Anderson et al.,Phys. Rev. Lett. 37(1976)799.
[26] J.G. Branson et al.,Phys. Rev. Lett. 38(1977)580;
J.G. Branson et al.,Phys. Rev. Lett. 38(1977)1331;
J.G. Branson et al.,Phys. Rev. Lett. 38(1977)1334;
G.G. Henry,Ph.D. thesis,Enrico Fermi Institute,Univ. of Chicago (1978).
[27] H. Kasha et al.,Phys. Rev. Lett. 36(1976)1007.
[28] K. Bunnell et al.,Phys. Rev. Lett. 40(1978)136.
B. Haber et al.,Phys. Rev. D22(1980)2107.
[29] J. Alspector et al.,Phys. Lett. 81B(1979)397.
[30] R.I. Dzhelyadin et al.,Nucl. Phys. B179(1981)189.
[31] M.J. Cordon et al.,Phys. Lett. 68B(1977)96.
[32] M. Faessler et al.,Phys. Rev. D17(1978)689.
[33] W.M. Morse et al.,Phys. Rev. D18(1978)3145;
D.M. Grannan et al.,Phys. Rev. D18(1978)3150.
[34] J. Stekas et al.,Phys. Rev. Lett. 47(1981)1686;
M.R. Adams et al.,Phys. Rev. D27(1983)1977.
[35] R. Stroynowski et al.,Phys. Lett. 97B(1980)315;
D. Blockus et al.,Nucl. Phys. B201(1982)205.

[36] A.T. Goshaw et al.,Phys. Rev. D24(1981)2829.
[37] S. Mikamo et al.,Phys. Lett. 106B(1981)428.
[38] J. Guy et al.,Phys. Lett. 66B(1977)300.
[39] J. Ballam et al.,Phys. Rev. Lett. 41(1978)1207.
[40] R. Ruckl,Phys. Lett. 64B(1976)39.
[41] N.S. Craigie and N.H. Thompson,Nucl. Phys. B141(1978)121.
[42] A.T. Goshaw et al.,Phys. Rev. Lett. 43(1979)1065.
[43] F.E. Low, Phys. Rev. 110(1958)974.
[44] R.N. Cahn,Phys. Rev. D7(1973)247.
[45] N.S. Craigie,Phys. Rep. 47(1978)1.
[46] R. Stroynowski,Phys. Rep. 71(1981)1.
[47] P. Baillon et al.,proposal CERN/SPSC/82–55(1982).
[48] V. Cerny et al.,Z. Phys. C31(1986)163.
[49] E.V. Shuryak,Phys. Rep. 61(1980)71;
E.V. Shuryak,CERN–yellow report, CERN 83–01.
[50] T. Adachi and I. Yotsuyanagi,Phys. Rev. D23(1981)1106.
[51] V. Cerny et al.,Phys. Rev. D24(1981)652;
V. Cerny et al.,Acta Phys. Pol. B10(1979)537;
V. Cerny et al.,Acta Phys. Pol. B9(1978)901.
[52] J.D. Bjorken and H. Weisberg,Phys. Rev. D13(1976)1405.
[53] E.V. Shuryak,Sov. J. Nucl. Phys. 28(1978)408.
[54] R.C. Hwa and K. Kajantie,Phys. Rev. D32(1985)1109.
[55] G. Domokos and J.I. Goldman,Phys. Rev. D23(1981)203.
[56] L.D. McLerran and T. Toimela,Phys. Rev. D31(1985)545.
[57] K. Kajantie and H.I. Miettinen,Z. Phys. C9(1981)341.
[58] K. Kajantie et al.,Helsinki University preprint HU–TFT–86–6.
[59] V. Hedberg,Proc. XV International Symposium on Multiparticle Dynamics, Lund,June 1984,World Scientific Publishing Co.,Singapore.
[60] T. Akesson et al.,Phys. Lett. 152B(1985)411.
[61] T. Akesson et al.,Phys. Lett. 178B(1986)447.
[62] T. Akesson et al.,CERN preprint CERN–EP/87–16.
[63] H. Gordon et al.,Nucl. Instrum. Methods 196(1982)303.
[64] O. Botner et al.,Nucl. Instrum. Methods 196(1982)315.
D. Cockerill et al.,Physica Scripta 23(1981)649.
[65] R. Batley et al.,Nucl. Instrum. Methods A242(1985)75.
[66] T. Akesson et al.,Nucl. Instrum. Methods A241(1985)17.
[67] L. Rosselet,Proc. Topical Conf. on The Application of Microprocessors to High–Energy Physics Experiments,CERN 81–07(1981)p.316.
[68] W.W.M. Allison and J.H. Cobb,Oxford University,Nucl. Phys. Lab., Ref. 13/80.
[69] C.G. Wohl et al.,Particle Data Group,Rev. Mod. Phys. 56,No 2(1984).
[70] B. Alper et al.,Nucl. Phys. B100(1975)237.
[71] K. Guettler et al.,Phys. Lett. 64B(1976)111.
[72] F.W. Busser et al.,Nucl. Phys. B106(1976)1.
[73] G.J. Donaldson et al.,Phys. Rev. Lett. 40(1978)684.
[74] E. Amaldi et al.,Nucl. Phys. B158(1979)1.
[75] T. Akesson et al.,Z. Phys. C18(1983)5.

[76] T. Akesson et al.,Phys. Lett. 158B(1985)282.
[77] R.M. Baltrusaitis et al.,Phys. Lett. B88(1979)372.
[78] J. Kanzaki et al.,J. Phys. Soc. Jpn. 50(1981)3849.
[79] K. Jaeger et al.,Phys. Rev. D11(1975)1756.
[80] A.C. Borg et al.,Nucl. Phys. B106(1976)430.
[81] R.D. Kass et al.,Phys. Rev. D20(1979)605.
[82] R. Barloutaud et al.,Nucl. Phys. B176(1980)285.
[83] G. Levman et al.,Phys. Rev. D21(1980)1.
[84] C. Poiret et al.,Z. Phys. C7(1981)283.
[85] M. Barth et al.,Z. Phys. C22(1984)23.
[86] L. Bailly et al.,Z. Phys. C22(1984)119.
[87] S. Chakrabarti et al.,Z. Phys. C27(1985)1.
[88] M. Bourquin and J.M. Gaillard,Phys. Lett. B59(1975)191.
M. Bourquin and J.M. Gaillard,Nucl. Phys. B114(1976)334.
[89] J. Bartke et al.,Nucl. Phys. B120(1977)14.
[90] C. Kourkoumelis et al.,Phys. Lett. 91B(1980)481.
[91] L. Montanet, Proc. 2nd International Conference on Physics in Collision, Stockholm,June 1982,Plenum Publishing Co.,New York.
[92] S. Reucroft,Proc. XIV International Symposium on Multiparticle Dynamics, Lake Tahoe,July 1983,World Scientific Publishing CO.,Singapore.
[93] B. Rossi,High Energy Particles,Prentice – Hall Inc.(1952).
[94] G.N. Patrick and L. Urban,Simulation of e^+e^- pair production by Photons GEANT 3.10 Users Guide,CERN DD/EE/84 – 1, and references therein.
[95] L. Urban,GEANT 3.02, a more recent parameterization is given in;
Total cross section for e^+e^- production by Photons,
GEANT 3.10 Users Guide,CERN DD/EE/84 – 1.
[96] Y.S. Tsai,Rev. of Modern Phys. 46(1974)815.
[97] Nuclear Data Tables, A7(1970).
[98] N.M. Kroll and W. Wada,Phys. Rev. 98(1955)1355.
[99] D. W. Joseph,Nuovo Cimento 16(1960)997.
[100] T. Miyazaki and E. Takasugi,Phys. Rev. D8(1973)2051.
[101] G.N. Patrick,Simulation of photon – electron Compton scattering.
GEANT 3.10 Users Guide,CERN DD/EE/84 – 1.
[102] J.C. Butcher and H. Messel,Nucl. Phys. 20(1960)15.
[103] R.L. Ford and W.R. Nelson,SLAC – 210 UC – 32 (1978).
[104] J. Fischer et al.,Phys. Lett. 73B(1978)359.
[105] K.O. Mikaelian and J. Smith,Phys. Rev. D5(1972)1763.
[106] G.B. Tupper et al.,Phys. Rev. Lett. D28(2905).
[107] V.L. Highland,Nucl. Instrum. Methods 129(1975)497.
[108] M.S. Dixit,Molier Scattering.
GEANT 3.10 Users Guide,CERN DD/EE/84 – 1, and references therein.
[109] G. Moliere,Z. Naturforsch. 2A(1947)133;
G. Moliere,Z. Naturforsch. 3A(1948)78.
[110] T. Akesson et al.,Phys. Lett. 128B(1983)354.
[111] A. Breakstone et al.,Phys. Lett. 132B(1983)463.
[112] A. Breakstone et al.,CERN preprint CERN – EP/86 – 132
[113] N.S. Craigie and D. Schildknecht,Nucl. Phys. B118(1977)311.

[114] H. Specht,Proc. Fourth Int. Conf. on Ultrarelativistic Nucleus–Nucleus Collisions,Helsinki,June 1984,World Scientific Publishing Co.,Singapore.
[115] I.H. Dunbar, Phys. Rev. Lett. 41(1978)210.
[116] G.R. Farrar and S.C. Frautschi,Phys. Rev. Lett. 36(1976)1017.
[117] S.D. Drell and T–M Yan,Phys. Rev. Lett. 25(1970)316.
[118] C.B. Newman et al.,Phys. Rev. Lett. 42(1979)951.
[119] J. Pisut,Private communication.
[120] P.V. Chliapnikov et al.,Phys. Lett. 141B(1984)276.
Figure 68 is from Y. Goldschmidt–Clermont, Private communication.
[121] T. Akesson et al.,to be published in Phys. Rev.
[122] E.W. Beier et al.,Phys. Rev. Lett. 37(1976)1114.
[123] O.L. Davies et al.,Statistical methods in research and production, Oliver and Boyd (1957).
[124] F. James and M. Roos,Nucl. Phys. B172(1980)475.

APPENDIX A

THE CHERENKOV REJECTION FORMULA

The Cherenkov rejection formula can be derived in the following way: Assume that the number of events, during a certain data taking time, for which the Cherenkov had a signal above threshold was A and the number of events where the signal was below threshold was P_1 . Let us further assume that the A sample can be divided into one part consisting of electrons (N_{e1}) and one part consisting of pions ($N_{\pi 1}$) so that

$$A = N_{e1} + N_{\pi 1}$$

A dE/dx cut is then constructed so that the probability that a pion survives the cut (X) is high and the probability that an electron survives (Y) is low. Because of the cut the P_1 sample is reduced to P_2 and in the same way the A sample is reduced to

$$B = N_{e2} + N_{\pi 2}$$

The rejection factor for pions is then given by

$$R = N_{\pi 1}/(N_{\pi 1} + P_1) = X \cdot N_{\pi 2}/(X \cdot N_{\pi 2} + X \cdot P_2)$$

but since $P_2 >> N_{\pi 2}$ an approximation can be made so that

$$R \approx N_{\pi 2}/P_2$$

The problem is then to calculate $N_{\pi 2}$ (P_2 is the number of pion triggers that survived the dE/dx cut and is therefore known) from the two equations

$$A = N_{\pi 1} + N_{e1} = N_{\pi 2}/X + N_{e2}/Y$$
$$B = N_{\pi 2} + N_{e2}$$

This is a simple algebraic problem with the solution

$$N_{\pi 2} = B - (A - B/X)/(1/Y - 1/X)$$

The rejection factor is then given by:

$$R = \left(B - \frac{A - \frac{B}{X}}{\frac{1}{Y} - \frac{1}{X}} \right) / P$$ where

R	the probability that a pion survive the Cherenkov cuts;
A	the number of Cherenkov triggered events before the dE/dx cut;
B	the number of Cherenkov triggered events after the dE/dx cut;
X	the probability that a pion survives the dE/dx cut;
Y	the probability that an electron survives the dE/dx cut;
P	the number of PI triggered events after the dE/dx cut.

A more exact calculation has to take into account three event samples (particles that did not fire the Cherenkov, particles that fired the Cherenkov but where the pulse height was lower than the off – line cut and particles that gave a pulse height larger than the off – line pulse height cut) but in practice the results change very little if this is done. The assumption that the PI triggered event sample consisted only of pions and that the MB and PT triggered event samples consisted only of pions and electrons is also not strictly correct but the systematic error introduced by this assumption is small.

APPENDIX B

ERROR ANALYSIS

The question about how to calculate and propagate errors, especially systematic errors, does not always have an obvious answer. For this reason it will be described below how the statistical, systematic and total errors were derived in this experiment.

It is well known that the measured number of events in a given time period is Poisson distributed and that the statistical error on such a measurement can be approximated with the square root of the number of events. However, this approximation is not valid for very small samples of events. The term "error" (σ) will mean, throughout this document, one standard deviation (=rms), that is for a central value $\bar{x}$ with the error σ, the range $\bar{x}\pm\sigma$ constitutes a 68% confidence interval.

In order to propagate errors, the following formula is frequently used [123]: If $Y=f(x_1,x_2,....,x_n)$, where f is any function, σ_i is the error on x_i, σ is the error on Y and $\mathrm{cov}(x_i,x_j)$ is the covariance of x_i and x_j, then

$$\sigma^2 = (\partial Y/\partial x_1)^2\cdot\sigma_1^2 + (\partial Y/\partial x_2)^2\cdot\sigma_2^2 + ...$$
$$+ (\partial Y/\partial x_1)\cdot(\partial Y/\partial x_2)\mathrm{cov}(x_1x_2) + (\partial Y/\partial x_1)\cdot(\partial Y/\partial x_3)\,\mathrm{cov}(x_1x_3) + ...$$
$$+ \text{terms involving higher differentials.}$$

If the variables are mutually independent and the function is linear, the formula is reduced to the first line. If the function is not linear, the first line is still a good approximation if the relative errors are small.

In this experiment the number of electrons (N_e) and pions (N_π) in a certain time period were measured and the ratio $r=N_e/N_\pi$ was calculated. The statistical error on this ratio (σ_r) was estimated with the following formula:

$$\sigma_r=(N_e/N_\pi)\cdot(1/N_e+1/N_\pi)^{1/2}$$

It has been pointed out by James and Roos [124] that this expression is a poor estimate of the statistical error when N_e and N_π are small. However, in this experiment, where at least N_π is very large, the errors obtained with the above formula should be reasonably accurate. The ratio r is called the uncorrected e/π ratio and the the more interesting so-called residual e/π ratio (R) is obtained by multiplying r with an efficiency correction (ε) and then subtracting the electron (M) and hadron background (H), i.e. $R=\varepsilon\cdot r - M - H$. The statistical error on R is estimated with $\sigma_S=\varepsilon\cdot\sigma_r$.

In addition to the statistical errors there are systematic uncertainties in the calculations of ε, M and H. The systematic errors are by there nature much more difficult to estimate than the statistical errors. If the systematic problems were per-

fectly known they could be corrected for and would consequently not introduce any uncertainty in the results. The most common way of estimating systematic errors is by changing some parameters in the analysis and see how the result changes. The obvious problem with this method is to determine how much the parameters should be changed. This method gives, in any case, some feeling for the sensitivity of the final result on different parameters in the analysis.

The aim in the error analysis was to estimate the systematic errors in a way so that the presented errors would correspond to a 68% confidence interval. In practice, however, it is easier to estimate a maximum error (corresponding to 2 – 3 standard deviations) than an error with the same confidence level as the statistical error. This is one of the reasons why the adding of systematic and statistical errors into a total error is questionable. The different systematic errors were assumed to be mutually independent and they were therefore added in quadrature:

$$\sigma_{sy} = (\sigma_{sy}[\varepsilon]^2 + \sigma_{sy}[M]^2 + \sigma_{sy}[H]^2)^{1/2} \quad \text{where}$$

σ_{st}	the total systematic error;
$\sigma_{sy}[\varepsilon]$	the systematic error in the e/π calculation;
$\sigma_{sy}[M]$	the systematic error in the MC calculation;
$\sigma_{sy}[H]$	the syst. error in the calculation of hadron background.

When the results from different triggers were combined, an average weighted by the statistical error was calculated. Given below is the definition of this weighted average and the corresponding formula which was used to calculate the statistical error [69]:

$$R = \frac{\frac{R_1}{\sigma_{s1}^2} + \frac{R_2}{\sigma_{s2}^2} + \frac{R_3}{\sigma_{s3}^2}}{\frac{1}{\sigma_{s1}^2} + \frac{1}{\sigma_{s2}^2} + \frac{1}{\sigma_{s3}^2}}$$

$$\sigma_s = \frac{1}{\sqrt{\frac{1}{\sigma_{s1}^2} + \frac{1}{\sigma_{s2}^2} + \frac{1}{\sigma_{s3}^2}}}$$

R	the weighted average;
R_1, R_2, R_3	the e/π ratio calculated with the three different triggers;
σ_s	the statistical error of the weighted average;
$\sigma_{s1}, \sigma_{s2}, \sigma_{s3}$	the statistical error for the three triggers.

The systematic error of the weighted average was a little bit more difficult to estimate than the statistical error. If the systematic error had been exactly the same for all three measurements the systematic error of the weighted average would have

been the same as in the individual measurement. However, the systematic errors were not the same for the different triggers due to corrections for the PT trigger efficiency which obviously was made only on one of the three measurements. The following procedure was followed to obtain a formula for the calculation of the systematic error in the weighted average (of two measurements):
Lets assume that the weighted average is

$$R = A \cdot R_1 + B \cdot R_2 \qquad \text{with}$$

$$A = \sigma_{s2}^2/(\sigma_{s1}^2 + \sigma_{s2}^2)$$
$$B = \sigma_{s1}^2/(\sigma_{s1}^2 + \sigma_{s2}^2)$$

and that A and B are constants. The ratios R_1 and R_2 can then be divided up into:

$$R_1 = \varepsilon_1 \cdot r_1 \quad - M - H$$
$$R_2 = \varepsilon_1 \cdot \varepsilon_2 \cdot r_1 \quad - M - H$$

and the weighted average then becomes:

$$R = A \cdot (\varepsilon_1 \cdot r_1 - M - H) + B \cdot (\varepsilon_1 \cdot \varepsilon_2 \cdot r_1 - M - H) \qquad \text{where}$$

R	the weighted average;
r_1, r_2	the uncorrected e/π ratio;
ε_1	all corrections to the measured e/π except ε_2;
ε_2	the corrections due to the PT trigger efficiency;
M	the Monte Carlo calculated background;
H	the background from hadrons.

The systematic error on the weighted average can then be estimated by:

$$\Delta R^2 = (A \cdot r_1 + B \cdot \varepsilon_2 \cdot r_2)^2 \cdot \Delta\varepsilon_1^2 + (B \cdot \varepsilon_1 \cdot r_2)^2 \cdot \Delta\varepsilon_2^2 + \Delta M^2 + \Delta H^2$$

where the prefix Δ is used as a notation for systematic errors.

A total error can be estimated either as the sum of the systematic and statistical errors or as the sum in quadrature. It was decided to use the latter definition of total error in this experiment. It should be stressed, however, that the precise meaning of this type of error is unclear. Throughout this document the principle is that systematic errors are given in tables while total errors are sometimes indicated in figures.

APPENDIX C

NOTATION & ABBREVIATIONS

A	mass number of a material
ADC	Analog to Digital Converter
AFS	Axial Field Spectrometer
AGS	Alternating Gradient Synchrotron
ANL	Argonne National Laboratory
α	fine structure constant ($\simeq = 1/137$)
B	Branching ratio
BB	Beam – Beam counters
BC	Bubble Chamber
1BC	the SLAC 1m Bubble Chamber
BEBC	Big European Bubble Chamber
BNL	Brookhaven National Laboratory
c	The velocity of light
CAMAC	Computer Automated Measurement and Control
CERN	Centre Europeenne pour la Recherche Nucleaire
CL	Confidence Level
CM	Center – of – Mass
$c\tau$	mean life (in cm)
DC	Drift Chamber
dE/dx	energy loss
DTR	Drift Time Recorder
E_S	Statistical Error
E_{sy}	Systematic Error
E_t	Total Error
E_T	Transverse Energy
E_{tot}	Total Energy
ETOT	Total Energy trigger
FNAL	Fermi National Laboratory
ϕ	the angle in the XY – plane
IH	Inner Hodoscope counters
ISR	Intersecting Storage Rings
k	momentum of a photon
KEK	National laboratory for high energy physics (Japan)
l	lepton
LASS	Large Aperture Superconducting Solenoid Spectrometer
LED	Light Emitting Diodeall
λ	absorption length
m	invariant mass
M	Multiplicity of decay product
MB	Minimum Bias trigger
m_T	transverse mass ($m_T = \sqrt{(m^2 + P_T{}^2)}$)

n	refractive index;
	charged multiplicity
N	Avogadro's number
NDF	Number of Degrees of Freedom
N_X	Number of parent particles that could have triggered
ω	energy of a photon
P	Probability
PDP	PDP – 11 – the online computers
PM	Photo Multiplier
P_T	trigger requiring a minimum transverse momentum
P_T	transverse momentum
P_t	momentum threshold
r	the distance to the vertex;
	the classical electron radius ($\simeq$ = 2.818 fm)
R	Rejection factor
RAL	Rutherford Appleton Laboratory
RLCBC	Rutherford Laboratory Cryogenic Bubble Chamber
rms	Root Mean Square
2SC	the SLAC 2m Streamer Chamber
SFM	Split Field Magnet
SLAC	Stanford Linear Accelerator
SPS	Super Proton Synchrotron
$\sqrt{s}$	center – of – mass energy
σ	cross section
T0	the event time
TDC	Time to Digital Converter
TOF	Time Of Flight
Q	difference between initial and final mass in a reaction
θ	the angle in the ZX plane
UCAL	Uranium – copper CALorimeter
UCCS	University of Chicago Cyclotron magnet Spectrometer
VFB	Very Fast Bus (part of the trigger system)
x	thickness of a material in fraction of a radiation length
X	The X direction (see fig. 3)
X′	thickness of a material (in g/cm^2)
X_0	radiation length (in g/cm^2)
x_F	Feynman x ($= P_L/P_L(max)$)
X_π	number of parents per π^0
y	rapidity
Y	the Y direction (see fig. 3)
Z	the Z direction (see fig. 3);
	the atomic number of a material
ZGS	Zero Gradient Synchrotron

Acknowledgments

This experiment could obviously not have been performed without the dedicated work of the many members of the AFS collaboration who built and operated the detectors, trigger system and data acquisition system.

The results of the analysis presented in this document are not the work of a sole person. The analysis of the electron data has taken four years during which time many people have been involved, either directly or in an advisory role. In particular, I would like to acknowledge the following people who I believe have been vital to the electron part of the AFS experiment: R. Batley, W.E. Cleland, A. Kalinovsky, D. Lissauer, J. Schukraft, H. Specht, W.J. Willis and M. Winik.

In addition, I would like to express my gratitude to the following people who have given me helpful suggestions about how to improve this document: G. Jarlskog, D. Lissauer, B. Lorstad, M. Murray and J. Schukraft.

I would also like to thank C. Hedberg who has helped me with the typing and proof – reading.

Financial support from University of Lund, the Swedish Research Council (NFR) and CERN is gratefully acknowledge.